ADSORPTION AND INTERFACIAL PROPERTIES OF FLUIDS FROM MOLECULAR SIMULATION

by

Xiongce Zhao

B.S. in Chemical Engineering, Tsinghua University, 1993

M.S. in Chemical Engineering, Tsinghua University, 1998

Submitted to the Graduate Faculty of

the School of Engineering in partial fulfillment

of the requirements for the degree of

Doctor of Philosophy

University of Pittsburgh

2004

UNIVERSITY OF PITTSBURGH

SCHOOL OF ENGINEERING

This dissertation was presented

by

Xiongce Zhao

It was defended on

January 6, 2004

and approved by

J. Karl Johnson, Associate Professor, Department of Chemical and Petroleum Engineering

Robert M. Enick, Professor, Department of Chemical and Petroleum Engineering

Kenneth D. Jordan, Professor, Department of Chemistry

Joseph J. McCarthy, Associate Professor, Department of Chemical and Petroleum Engineering

Dissertation Director: J. Karl Johnson, Associate Professor, Department of Chemical and Petroleum Engineering

ADSORPTION AND INTERFACIAL PROPERTIES OF FLUIDS FROM MOLECULAR SIMULATION

Xiongce Zhao, PhD

University of Pittsburgh, 2004

The objective of this research is to provide molecular-level insight on the adsorption and interfacial properties of fluids. Molecular simulation is the tool used to perform this work. The adsorption of polar and nonpolar molecules on carbonaceous adsorbents and metal surface is studied by using existing simulation techniques and new techniques developed by ourselves. The interfacial properties of quantum liquid mixtures are investigated using path integral simulations. The physical behavior of a DNA segment interacting with a novel adsorbent, single-walled carbon nanotubes (SWNTs), in aqueous environment is studied by molecular dynamics simulations.

We have simulated the adsorption of propane on graphite surface. We obtain good agreement between simulations and experiments on both the isotherms and isosteric heat of adsorption. We have investigated five different propane potential models. We found that the fluid-fluid potential plays a significant role in determining the location of the 1-2 layering transition. We identified an orientational ordering transition for propane in the monolayer. In order to study the polar molecules adsorbed on graphite, we have developed potential models including the graphite quadrupole and induction interaction between a polar molecule and the graphite surface. We have performed simulations of acetone adsorption on graphite to investigate the layering transitions, geometry, and coverage of acetone in the first, second and third layers. The simulation results agree well with the experimental observations. We have studied the structure of second layer physisorbed carbon monoxide on the Ag(110) metal surface. Both simulation and experiment found that the second layer CO molecules

form orientationally ordered structures, with CO bond angles tilting at 45° to the surface normal and azimuthal angles tilting in multiples of 45° to the principal azimuth axis. From the simulation, we conclude that redistribution of charges within the first layer of CO on silver accommodate the formation of ordered second layer CO structures.

We have performed parallel hybrid path integral Monte Carlo to study the interfacial properties of pure and mixture quantum liquids. We calculated the surface tension of pure liquid H_2, pure liquid D_2, and H_2/D_2 mixtures. The surface tension of pure fluids we calculated from simulations agree well with the experimental data. We observed interfacial segregation in the H_2/D_2 mixtures with H_2 migrating to the surface. The H_2/D_2 mixture therefore exhibits negative deviations from ideal solution behavior. We studied the adsorption of a DNA segment with 12 base pairs on a (8,8) single walled carbon nanotube using the AMBER MD simulation software package. We found that the DNA adsorbs onto the wall of a regular SWNT or a positively charged SWNT, with a time scale of 100 pico-seconds. When the DNA is uncharged the end of the DNA molecule binds to the SWNT surface. DNA binds with its axis nearly parallel to a positively charged SWNT. The angle between the DNA and SWNT axes is about 20-30°. In contrast, DNA does not bind to negatively charged SWNTs, because of the net negative charge on DNA. We found that the adsorption process does not affect greatly the structures of the DNA. However, the adsorption on a regular SWNT delays the A-form to B-form conversion for an A-DNA.

KEYWORDS

Adsorption
DNA
Fluid
Graphite
Interface
Molecular Dynamics
Monte Carlo
Simulation
SWNT

TABLE OF CONTENTS

LIST OF TABLES

LIST OF FIGURES

PREFACE

I am very thankful to my adviser, Dr. J. Karl Johnson, for training, mentoring and providing opportunities to me during the past four years. His guidance, inspiration, encouragement, and wise and thoughtful discourses have laid the foundation for my Ph. D.. I am also grateful for his kind concern and help beyond my study. I learned a lot from both his academic excellence and character nobleness.

I thank Dr. Craig E. Rasmussen at Advance Computing Lab of Los Alamos National Laboratory for his advising during my internship. I also thank Los Alamos National Laboratory Graduate Research Assistantship Program for giving me the opportunity for the internship.

I thank Dr. Eric Borguet, Dr. Radisav Vidic, and Dr. John T. Yates Jr., together with their group members for stimulating discussions and fruitful collaborations. I thank Dr. Robert M. Enick, Dr. Kenneth D. Jordan, and Dr. Joseph J. McCarthy for serving on this Ph. D. committee. I thank National Science Foundation for support of this work. I am very much indebted to the immense help and encouragement by my group colleagues.

Finally but not leastly, I must acknowledge my family members, whose sacrifices and encouragements have been constant and essential throughout all these years.

1.0 INTRODUCTION

A basic understanding of the physics dominating the process of adsorption and properties of fluids at interfaces is of great importance in both scientific and industrial settings. Many interesting phenomena occur during the adsorption process and at interfacial regions. Examples include layering transitions, capillary condensation, separation, and wetting transitions. At practical level, a better understanding of molecular-level processes at interfaces can help us to design more efficient sorbents for industrial applications.

Accurate measurement of adsorption and interfacial properties from experiments is very difficult, especially mixtures. Most of the available experimental adsorption data are for small molecules on traditional adsorbents or single crystals, such as activated carbon, zeolites, etc.[1] The practical applications of adsorption in industrial plants are largely based on empirical designs.

The commonly used analytical and numerical theories for study of adsorption and interfacial properties can be divided into three categories: continuum treatment (macroscopic correlation), statistical mechanical theories, and molecular simulations. Continuum treatments are based on experimental observations, together with classical thermodynamic arguments. [2, 3] These methods are still useful in industrial design but can usually only explain the phenomena in an empirical sense. The typical statistical mechanical theory used in study adsorption is density functional theory (DFT). It is accurate under a wide range of conditions and much faster than molecular simulations. But DFT is not appropriate for investigation of the behavior of complex systems, such as biomolecule adsorption.

The general objective of this research is to study the physics behind adsorption and interfacial phenomena of fluids by computer simulation. Computer simulation provides reliable results for well-defined systems, including information on the molecular level. It is relatively

easy to incorporate molecularly structured adsorbents such as zeolites and single walled nanotubes into simulations. Through computer simulation, we can probe experimentally inaccessible properties such as molecular structure and energetics. Consequently, tremendous progress has been made in the past few decades in molecular modeling of adsorption and interfacial properties of simple fluids.[4] The adsorption and interfacial properties that can be calculated by simulations include adsorption isotherms, isosteric heats, interaction forces between molecules, diffusivity, phase equilibrium, surface tension, layering transition, capillary condensation, etc.

New simulation algorithms and accurate potential models have provided tools for performing molecular simulation of fluids over a wide range of pressures and temperatures. In order to study the adsorption and interfacial properties of fluids, we have used these techniques extensively in this work. We have carried out studies on the adsorption of simple polar and nonpolar fluids adsorbed on carbonaceous and metal surfaces, such as propane adsorbed on graphite, acetone adsorbed on graphite, carbon monoxide adsorbed on silver, etc. We have developed potential functions to better account for the interaction between polar molecules and polarizable sorbents. These potentials are more accurate for simulation of adsorption on more realistic sorbents. We carried out large scale parallel path integral hybrid Monte Carlo simulation to study the interfacial properties of quantum fluids. We also performed molecular dynamics simulation of a DNA segment adsorbing on a single walled carbon nanotube in aqueous solution.

The thesis is organized as follows: In Chapter 2 we report the simulation study of a nonpolar molecule, propane, on a model carbonaceous surface, the graphite basal plane. We calculate the adsorption isotherms and adsorption heats to compare the results with experimental data. This chapter is taken from the Journal of Chemical Physics, volume 117, pages 7719-7731, published with our experimental collaborators S. J. Kwon, E. Borguet, and R. Vidic. In Chapter 3 we develop the potential models for calculating the electrostatic interactions between polar molecules and the graphite surface. In Chapter 4 we present the simulation results of the adsorption of polar molecules, acetone, on graphite and compare with the experimental findings from collaborators S. J. Kwon, E. Borguet, and R. Vidic. This chapter is based on Langmuir, volume 18, pages 2595-2600. We calculate the transition

pattern and the surface structures of the adsorbed layers and compare the results with the experimental observations. Chapter 5 is devoted to the calculation of the structures of second layer physisorbed carbon monoxide on silver surface. These simulations complement experimental data from J. G. Lee, S. H. Hong, J. Ahner, and J. T. Yates. In Chapter 6 we present the path integral simulation study of quantum fluids, and compare the calculated interfacial properties such as surface tensions with experimental data. Finally, Chapter 7 is on the simulation study of a DNA segment interacting with a single walled carbon nanotube in an aqueous environment.

2.0 SIMULATION OF PROPANE ON GRAPHITE

2.1 INTRODUCTION

Molecular simulation studies on the adsorption of alkanes on solid surface focused primarily on modeling porous sorbents, such as graphite slit pores and ideal cylindrical pores,[5, 6, 7, 8, 9, 10] porous glass [11, 12], microporous carbons [13, 14], and zeolitic materials [15, 16, 17, 18, 19, 20, 21, 22, 23, 24, 25, 26, 27, 28, 29, 30, 31]. There have been extensive simulations of adsorbed fluids and solids on graphite surfaces, with most simulations performed for relatively simple molecules. [32, 5, 6, 33, 34] A few simulations of the adsorption quantum fluids (hydrogen, helium) on graphite have been carried out. [35, 36, 37, 38, 39] Relatively few simulations of adsorption of higher alkanes on graphitic and other surfaces have been performed. [40, 41, 42, 43, 44] Most of these simulations have addressed structural and melting transitions in the monolayer; none of these studies have investigated layering transitions.

Propane is one of the most important lower hydrocarbons and has received significant research attention. Several experimental studies have been performed to determine general features of high pressure physical adsorption on homogeneous high energy solid surfaces at ambient temperature [45, 46, 47]. Isotherms of propane on graphon have been measured in the temperature range from 273 to 373 K and pressure range from 1 to 150 bar using the volumetric method. In theoretical studies, Cracknell et al. [7, 8, 9] calculated isosteric heat of adsorption at zero coverage of propane and ethane on graphite at ambient temperatures. Their results were in excellent agreement with experimental data. Furthermore, they simulated the adsorption of several alkane mixtures in graphite slit pores, obtained the separation selectivity, and compared their calculations with ideal adsorbed solution theory.[48]

However, to our knowledge, no experimental or theoretical work has been done on the adsorption behavior of propane on graphite at low temperatures and vacuum pressures. An understanding of such a simple model system is a prerequisite to the investigation of more complex carbonaceous systems important in atmospheric processes, catalysis, adsorption, and lubrication.

In this work we present grand canonical Monte Carlo calculations of propane adsorption on graphite. The temperature range evaluated in this study is from 90 to 110 K (the freezing point of bulk propane is 84.5 K[49]), while the pressure spans a range of six orders of magnitude from 5×10^{-10} to 5×10^{-4} torr. Theoretical isotherms and isosteric heats of adsorption are compared with experimental data. The orientations of the monolayer propane molecules are discussed.

2.2 POTENTIAL MODELS

2.2.1 Fluid-fluid interaction

There are two kinds of interactions involved in simulation of adsorption, namely, fluid-fluid and solid-fluid interactions. The contribution of fluid-fluid interactions to the total energy of adsorption increases with coverage. Thus, the fluid-fluid potential will not affect the shape of the adsorption isotherm at very low coverage (Henry's law region), but will have profound effect at higher loadings. In this study we have investigated five different propane potential models, namely, the Lustig and Steele[50] (LS), OPLS [51], TraPPE [52], NERD[53], and SKS[54] models. All of these potentials are based on a united-atom description of propane but they differ in the geometry of the propane molecule and the potential parameters.

In all five potential models the interaction between two sites i and j on two different propane molecules are described by pairwise-additive Lennard-Jones potentials,

$$u(r_{ij}) = 4\epsilon_{ij}\left[\left(\frac{\sigma_{ij}}{r_{ij}}\right)^{12} - \left(\frac{\sigma_{ij}}{r_{ij}}\right)^{6}\right], \tag{2.1}$$

Table 1: Parameters for the propane potential models used in this work.

	LS	OPLS	SKS	TraPPE	NERD
δ_{CC}(Å)	2.16	1.53	1.54	1.54	1.54
θ_{CCC}	90°	112°	114°	114°	114°
σ_{CH_2}(Å)	3.527	3.905	3.93	3.95	3.93
σ_{CH_3}(Å)	3.527	3.905	3.93	3.75	3.857
ϵ_{CH_2}/k_B(K)	119.57	59.4	47	46	45.8
ϵ_{CH_3}/k_B(K)	119.57	88.1	114	98	102.6

δ_{CC} is the bond length between CH_2 and CH_3, θ_{CCC} is the bond angle.

where r_{ij}, ϵ_{ij} and σ_{ij} are the site-site separation, energy parameter, and size parameter, respectively, for the two sites. The interaction parameters for different models are listed in Table 1.

Parameters for the cross interactions are obtained using the Lorentz-Berthelot combining rules,

$$\sigma_{ij} = \frac{\sigma_i + \sigma_j}{2}, \tag{2.2}$$

$$\epsilon_{ij} = (\epsilon_i \epsilon_j)^{1/2}. \tag{2.3}$$

We have calculated the thermodynamic properties of pure propane at several different liquid and vapor state points using the five different potentials in order to test their accuracy. The simulation pressures were computed from ensemble averages of the pressure virial[55]. The calculated and experimental pressures are shown in Table 2.

All simulations were carried out in the NVT ensemble at the experimental temperatures and densities. The bulk system consisted of 610 molecules and was equilibrated for 1.5×10^6 steps and data were collected over 5×10^5 steps. All the potentials were truncated at $5\sigma_{ff}$ and no long-range corrections were applied. The authors of SKS and TraPPE models suggested that an accurate calculation of thermodynamic properties of propane using these potentials requires a cutoff of more than 30 Å for temperatures as low as about 100 K. Using such a long cutoff would make the simulation of the liquid very expensive. However, we ran simulations

Table 2: Comparison of liquid and gas phase pressures for propane from experiment and calculated from the five potentials listed in Table 1. The simulations were performed in the NVT ensemble.

T	ρ	$P_{\rm ex}$	Simulated Pressure (MPa)				
(K)	(kg m^{-3})	(MPa)	LS	OPLS	TraPPE	SKS	NERD
Gas							
200	0.2667	0.01	0.010012(1)	0.010035(8)	0.010014(6)	0.009994(7)	0.010009(1)
300	0.1771	0.01	0.010003(3)	0.010039(2)	0.010007(2)	0.009997(3)	0.010004(3)
300	1.7955	0.1	0.09990(1)	0.10048(6)	0.10021(1)	0.09947(1)	0.09997(7)
AAD			8.3×10^{-6}	4.1×10^{-5}	1.4×10^{-5}	2.0×10^{-5}	5.3×10^{-6}
Liquid							
100	718.94	0.01	12(3)	144(2)	13(2)	252(7)	113(2)
200	615.98	0.1	7(3)	56(2)	7(2)	57(2)	34(2)
250	559.46	1.0	1.2(3)	31(2)	7(2)	23(2)	34(2)
300	492.49	2.0	-0.2(1)	18(1)	7(1)	4(2)	9(1)
AAD			5.3	61.5	7.7	83.3	46.7

The numbers in parentheses represent uncertainties in the last digit. AAD is the average absolute deviation, defined as AAD $= \frac{1}{N}\sum_{i=1}^{N}\left|P_i^{\rm exp} - P_i^{\rm sim}\right|$.

with a cutoff of $3.5\sigma_{\rm ff}$ (about 14 Å) and $5\sigma_{\rm ff}$ (about 20 Å) to calculate the internal energy of liquid propane at the temperature range of 90 to 180 K, and found that the differences in the internal energies from these two cutoffs are typically about one percent.

The simulated pressures are compared with experimental data. [56] As shown in Table 2, all five models predict accurately the gas phase pressures while none reproduces the liquid pressures. This is not surprising because the incompressibility of liquids means that a small error in the potential may lead to a very large error in the computed liquid pressures. We have also calculated the internal energy, U, of liquid propane at 0.01 MPa as a function of temperature using these potentials. The values obtained were compared with the results from the Modified-Benedict-Webb-Rubin (MBWR) equation of state (EOS)[49], the parameters of which were regressed from experimental data. The results are plotted in Fig. 1.

We found that the LS model gives the best agreement with the MBWR EOS data. We note that only the LS model was specifically designed for propane while the other four potentials were developed from a universal description of n-alkanes. The LS model was designed to reproduce the PVT properties of propane, not the energetic properties, so it is somewhat surprising that it is superior to the other models for predicting internal energy, especially

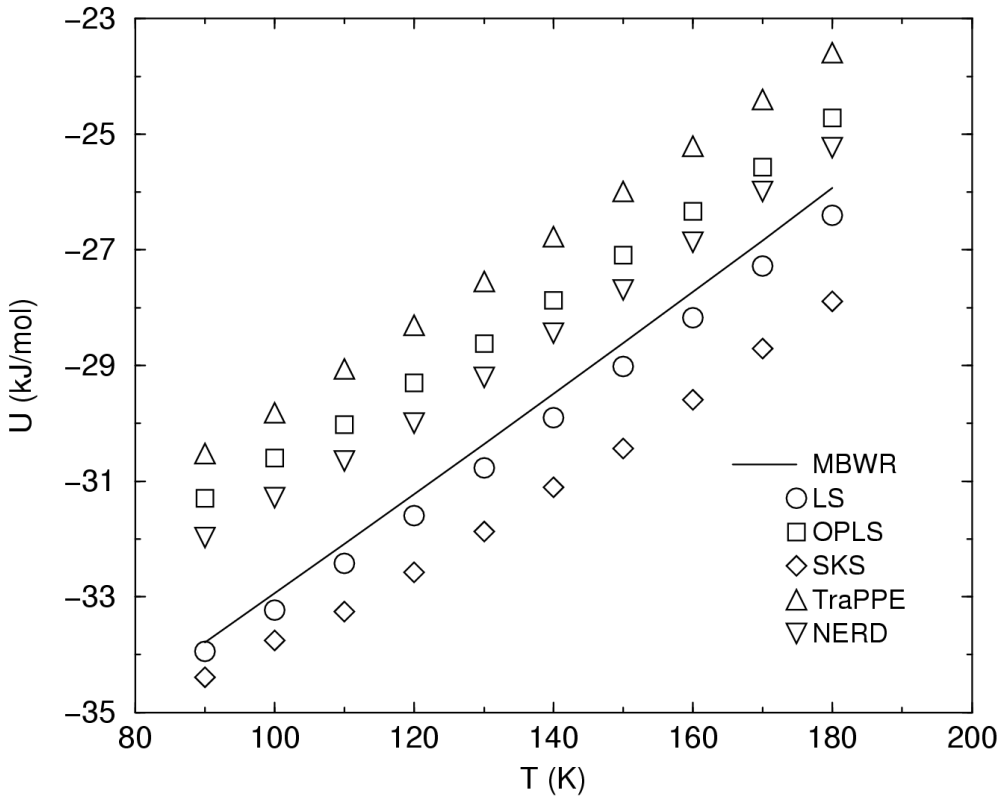

Figure 1: Internal energy of liquid propane calculated from the MBWR equation of state[49] (line) and simulations at 0.01 MPa. The symbols are from simulations using the five potentials listed in Table 1 .

given the unrealistic bond lengths and bond angle used in the LS model. Nevertheless, because of its success, as illustrated in Fig. 1, we adopted the LS potential as the basic model throughout our adsorption simulations. The other four potentials were used to compute a single isotherm in order to assess the effect of the fluid-fluid potential on the isotherm.

2.2.2 Fluid-solid interaction

The graphite surface is modeled as a smooth basal plane. The interaction energy between a propane molecule and graphite surface is given by the 10-4-3 potential[57]:

$$u_{\rm sf}(z) = 2\pi\epsilon_{\rm sf}{\sigma_{\rm sf}}^2\Delta\rho_{\rm s}\left[\frac{2}{5}\left(\frac{\sigma_{\rm sf}}{z}\right)^{10} - \left(\frac{\sigma_{\rm sf}}{z}\right)^{4} - \frac{\sigma_{\rm sf}^4}{3\Delta(0.61\Delta+z)^3}\right], \tag{2.4}$$

where z is the distance between a fluid molecule interaction site and the graphite surface, ρ_s is the graphite number density, and Δ is the distance between the graphene sheets in graphite. The solid-fluid interaction parameters $\epsilon_{\rm sf}$ and $\sigma_{\rm sf}$ are calculated from the Lorentz-Berthelot rules. The values of the parameters are: $\rho_{\rm s} = 114$ nm^{-3}, $\Delta = 0.335$ nm, $\epsilon_{\rm s}/k_{\rm B} = 28.0$ K, and $\sigma_{\rm s} = 0.340$ nm.[7]

2.3 SIMULATION METHODOLOGY

We have used grand canonical Monte Carlo (GCMC) simulations to compute the isotherms and isosteric heats. A detailed description of the GCMC technique can be found elsewhere [55]. In GCMC, the temperature, T, the volume of the simulation cell, V, and the chemical potential, μ, are held constant. The number of molecules in the cell is allowed to vary and the average value represents the absolute amount of gas adsorbed.

Four kinds of moves are involved in GCMC simulation of propane on graphite: (i) displacement of the center of mass of a molecule, (ii) rotation of a molecule, (iii) creation of a molecule, and (iv) deletion of a molecule. Periodic boundary conditions and minimum image conventions were applied in the x and y directions of the simulation box. The dimensions of the simulation box were equal in the x and y directions and ranged from 10 to 15 $\sigma_{\rm ff}$, which gave average numbers of adsorbed molecules ranging from 70 to 350. The bottom wall of the

simulation box was chosen as the adsorbing surface and the opposite wall was chosen to be purely repulsive to keep the molecules in the box. The separation between the two walls was fixed at 20 σ_{ff} so that the influence of the repulsive wall on the adsorption properties was negligible. The site-site interaction cutoff distance was 5 σ_{ff} and no long-range corrections were applied. The probabilities of making a displacement, rotation, deletion and creation were each set to 0.25. The maximum values of displacement and rotation were adjusted during the equilibration to achieve acceptance ratios for displacements and rotations of about 0.4.

Simulations were performed at temperatures of 91, 95, 100, 105, 110, and 300 K. The low temperature simulations ($T \leq 110$ K) were equilibrated for 5×10^7 moves, after which data were collected for another 5×10^7 moves. Simulation statistics at 300 K were much better so that only 2×10^6 moves for equilibration and data collection were required.

The isosteric heat of adsorption can be computed directly in a grand canonical Monte Carlo (GCMC) simulation from the fluctuations of the number of molecules and the energy, [58]

$$q_{\mathrm{st}} = kT - \frac{\langle UN\rangle - \langle U\rangle\langle N\rangle}{\langle N^2\rangle - \langle N\rangle^2}, \tag{2.5}$$

where q_{st} is the isosteric heat of adsorption per molecule, U is the total potential energy of the system, and N is the number of molecules in the simulation cell.

Experimental adsorption isotherms are usually measured in terms of the excess amount adsorbed as a function of the pressure of the bulk fluid in equilibrium with the adsorbed fluid, while the simulations give absolute amounts adsorbed. The excess adsorption is given by

$$n^e = n - V^a\rho^g \tag{2.6}$$

where n^e and n are the excess and total (absolute) adsorption, respectively, V^a is the volume in the system that can be occupied by gas molecules, and ρ^g is the density of the bulk gas at the system temperature and pressure. Note that V^a excludes the volume of the solid sorbent. The absolute and excess adsorption are virtually identical at the low pressures considered in this study. We obtained the bulk pressures for each chemical potential by assuming ideal gas behavior in the bulk. This is an excellent approximation given the range of pressures covered. We have also performed GCMC simulations of bulk propane at several state points to verify

the accuracy of the ideal gas law approximation. The results from these two approaches were found to agree within the simulation errors.

2.4 RESULTS AND DISCUSSION

2.4.1 Adsorption isotherms

Propane isotherms at about 90, 95, 100, 105, and 110 K were obtained in our study. The pressures at which the bilayer begins to form were found to be 2.4×10^{-6}, 7.5×10^{-6}, 4.5×10^{-5}, 1.5×10^{-4}, and 5.5×10^{-4} torr, for 90, 95, 100, 105, and 110 K, respectively. The transition pressures from experiment for 90, 95, 100 and 105 K are 2.4×10^{-6}, 2.3×10^{-5}, 6.2×10^{-5}, and 2.4×10^{-4}, respectively. The estimated uncertainty in the absolute pressure from experiment at which the bilayer forms is about 30%, while the uncertainty in the relative temperature is about ±1 K.

Two representative isotherms from GCMC simulations, along with the experimental data, are shown in Figs. 2 and 3. In Fig. 2, we present the adsorption isotherm data for propane on graphite at 91 K determined from experiments and simulations. The experimental adsorption loadings were measured in arbitrary units and converted to μmol/m^2 by matching the monolayer loading with the simulation data. Because the relative adsorbed amount measured experimentally are accurate, the good agreement between experiments and simulations for the second layer loadings indicate that simulations accurately predict relative coverages in the first and second layers. The position of the first to second layer transition on the pressure axis determined from experiments and simulations are in very good agreement. The agreement, however, is probably fortuitous because of the experimental difficulty in measuring the absolute pressure accurately. Furthermore, transition pressures are very sensitive to substrate temperature. While relative temperature precision is about one Kelvin, absolute temperature is measured less accurately. We are unable to observe a transition from zero loading to the first layer in any of the simulations. We obtained virtually complete monolayer coverage at the lowest pressures simulated (about 2×10^{-8} torr), indicating that the 0-1 transition must occur at pressures lower than 2×10^{-8} torr. The apparent 0-1 layering

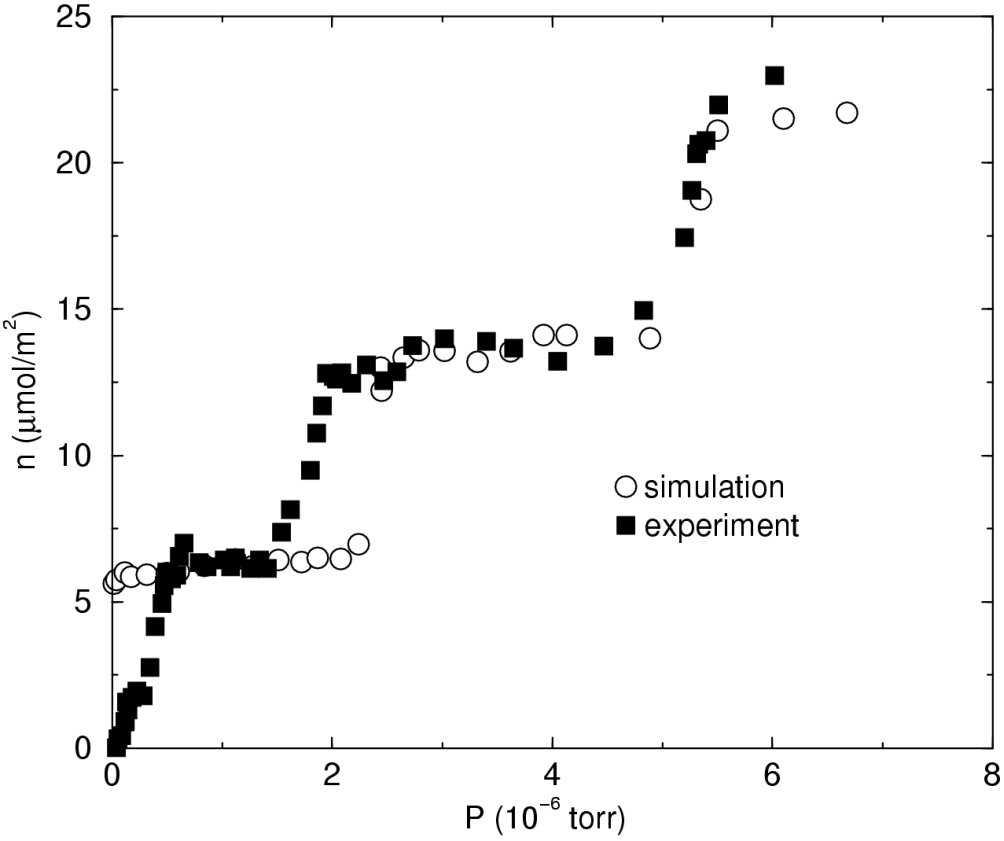

Figure 2: Adsorption isotherms from experiment and simulation at 91 K. The filled squares are experimental data, the open circles are GCMC results. The simulations report the absolute adsorption, which at these pressures is virtually identical to the excess adsorption. The experimental data are measured in arbitrary units and scaled to match the first layer coverage from simulations.

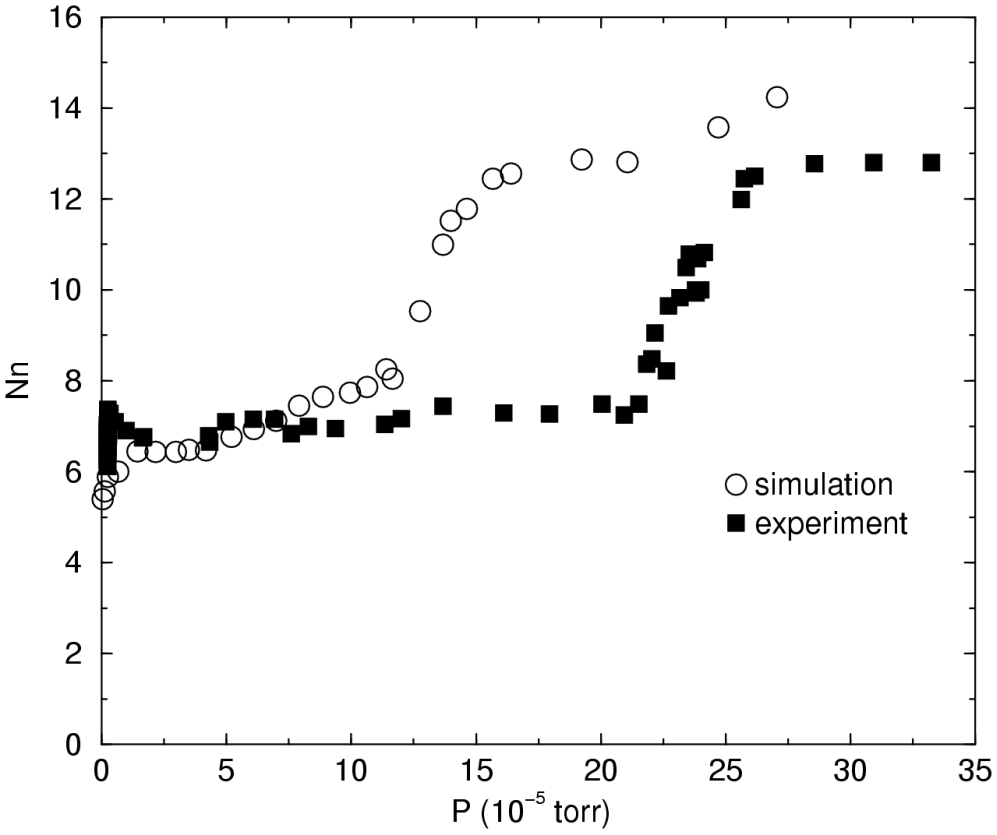

Figure 3: Adsorption isotherms from experiment and simulation at 105 K. The filled squares are experimental data, the open circles are GCMC results.

transition seen in the experimental data (e.g., Figs. 2 and 3) is the result of kinetic effects. Experimental and simulation isotherms for 105 K are shown in Fig. 3. The 1-2 layering transition pressures from simulation and experiment do not agree as well as in the 91 K case, but they are in good qualitative accordance. The relative coverages in the first and second layer are in excellent agreement.

We have investigated the effect of the fluid-fluid potential model on the adsorption isotherm by computing the 100 K isotherm for all five propane potential models examined in this study. The results of these calculations are plotted together with experimental data in Fig. 4.

The most striking observation in Fig. 4 is that the transition pressure for the 1-2 layering transition computed using the different fluid-fluid potentials varies by more than an order of magnitude, which is significantly more than the difference observed between our experimental data and simulation data obtained using the LS potential. The SKS potential exhibits the lowest transition pressure of about 2×10^{-5} torr, while the TraPPE potential gives the highest transition pressure of about 6×10^{-4} torr.

Comparing Figs. 1 and 4, we see that the sequence of the 1-2 layering transition pressures at 100 K for different propane models exactly follows the ordering of internal energy values for liquid propane. For example, the liquid propane internal energy calculated by SKS model is the lowest in Fig. 1 and consequently, the transition pressure predicted by the SKS model in Fig. 4 is the smallest. The coincidence of liquid internal energies with the order of the transition pressures is due to the important role of the fluid-fluid interactions in simulating the 1-2 layering transition. It is noted that about a 10% difference in U (comparing SKS with TraPPE in Fig. 1) gives rise to more than an order of magnitude change in the transition pressure, while having apparently no effect on the sharpness of the transition. We have computed the isosteric heats of adsorption for the 100 K isotherm using each of the five fluid-fluid potentials listed in Table 1. The values of $q_{\rm st}$ were computed from Eq. (2.5). We note that the differences in the fluid-fluid potentials have a relatively small effect on the values of $q_{\rm st}$ when compared with the transition pressures. The large statistical uncertainties in the simulation data tend to mask the differences due to the potentials. We note that changing the fluid-fluid potential implicitly changes the solid-fluid potential through changes in the

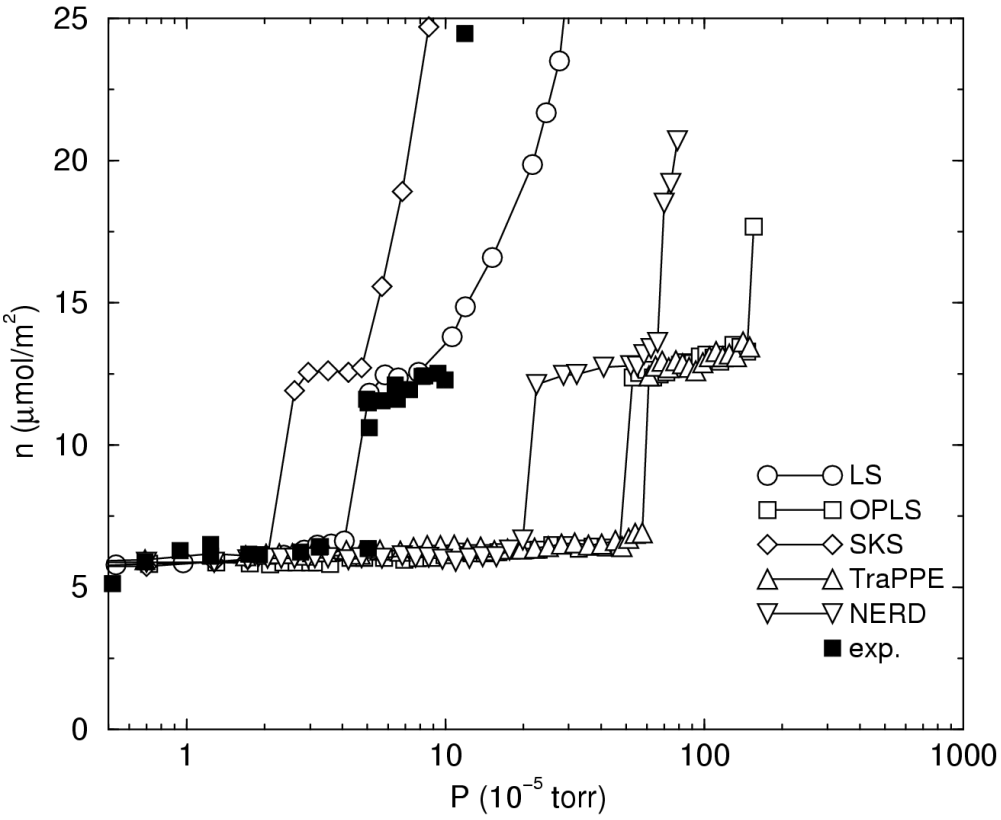

Figure 4: Adsorption isotherms at 100 K from five different propane potential models and experiments. The filled squares are from experiments. The open circles, squares, diamonds, up triangles, and down triangles are from the LS, OPLS, SKS, TraPPE, and NERD potentials, respectively. The lines are drawn to guide the eye.

geometry of the molecule and through the combining rules of Eqns. (2.2) and (2.3). We have studied the effect of changing only the solid-fluid potential by computing the 100 K isotherm using the LS fluid-fluid potential, while changing ϵ_{sf} in Eq. (2.4) by ± 5 and $\pm 10\%$. The results of these calculations are plotted in Fig. 5.

Note that perturbing the solid-fluid potential has a much smaller effect on the location of the 1-2 layering transition pressure than the effect of changing the fluid-fluid potential (compare Figs. 4 and 5). An increase (decrease) of 10% in the solid-fluid potential leads to roughly a factor of two decrease (increase) in the transition pressure. We note that the shape of the isotherm is a fairly strong function of the solid-fluid potential. A decrease in ϵ_{sf} of only five percent appears to change the 1-2 layering transition from first order to continuous, as can be seen from the shape of the isotherm. This is surprising because one would expect the 1-2 layering transition to be less sensitive to small perturbations in the solid-fluid potential given that the magnitude of the potential is attenuated roughly by a factor of 0.1 in the second layer compared with the first layer due to the increased distance from the graphite plane.

2.4.2 Adsorption energetics

The isosteric heat of adsorption can be calculated from the following relationship,[59]

$$q_{st} = -R \left[\frac{\partial \ln P}{\partial (1/T)} \right]_n , \tag{2.7}$$

where q_{st} is the isosteric heat, T is the temperature, P is the pressure and n is the coverage. Plots of $\ln P$ as a function of reciprocal absolute temperature at constant coverage are called adsorption isosteres and the isosteric heat of adsorption is determined by their slopes. Experiments performed at five temperatures (90, 95, 100, 105 and 110 K) allow determination of q_{st}. The average pressures where the second layer just begins to form at each temperature was used to construct a single isostere. For experiments at 110 K second layer formation was not observed at pressures up to 2×10^{-4} torr, consistent with the simulations showing that the second layer forms at a pressure of about 5×10^{-4} torr. The isosteres procedure can be applied to the isotherms calculated from simulations. The values of q_{st} from the

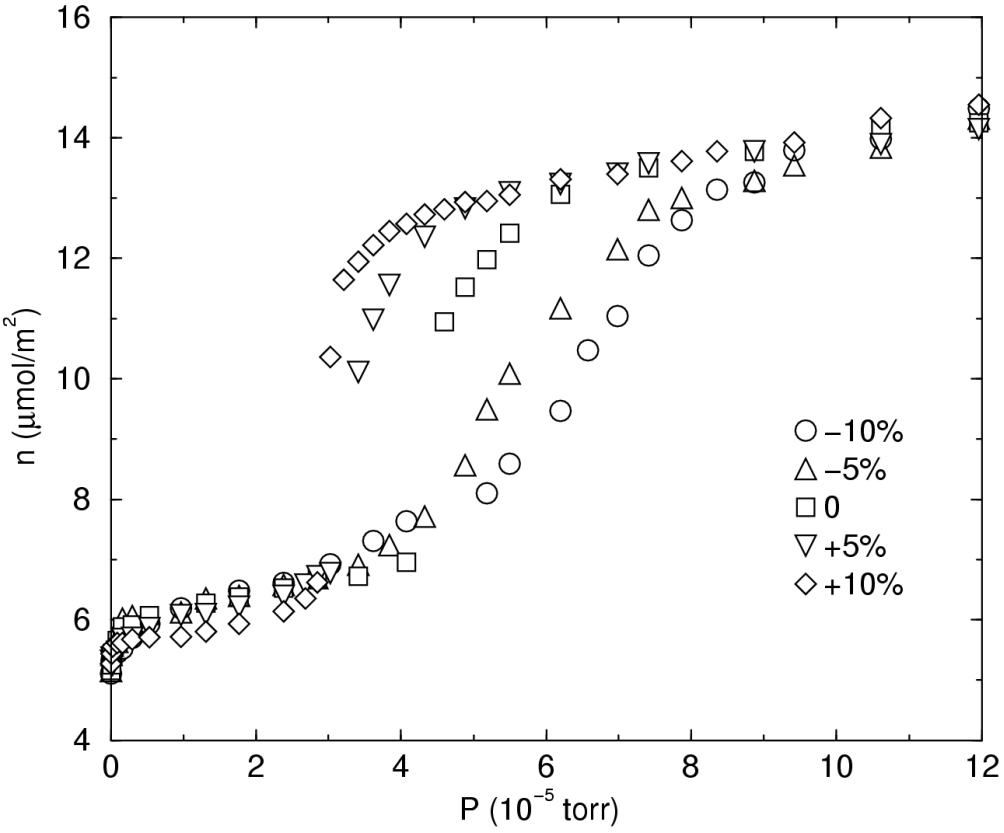

Figure 5: Adsorption isotherms at 100 K using the LS fluid-fluid potential and different values of of ϵ_{sf}. The squares denote the standard ϵ_{sf}, the circles (diamonds) denote an increase (decrease) of 10% in ϵ_{sf}, and the up (down) triangles denote an increase (decrease) of 5%. All the simulations in this figure were performed with a cutoff of 3.5σ.

isosteres [Eq. (2.7)] and the statistical method [Eq. (2.5)] should agree with each other, although it has been noted that measurements of q_{st} by different experimental methods are often in disagreement and differences of 10-20% are common.[59] The isosteres computed from simulation and experimental data are plotted in Fig. 6.

The experimental values in Fig. 6 represent the average of several isotherm measurements and the error bars were estimated based on the scatter in the experimental data. The values of isosteric heat at bilayer formation determined from experimental and simulation data are in excellent agreement. The experimentally determined value of q_{st} is 23±2 kJ mol^{-1}, while that calculated from simulation is 24 ± 1 kJ mol^{-1}.

The dependence of q_{st} on pressure at 91 K as computed from GCMC simulation through Eq. (2.5) is shown in Fig. 7. At lowest pressures simulated in our work, the isosteric heat of adsorption is estimated to be around 31 kJ mol^{-1}. This corresponds to complete monolayer coverage, although there is a slight increase in the coverage as the pressure increases before the transition pressure for the second layer. The value of $q_{st} \sim 31$ kJ mol^{-1} implies a binding energy[2] of $q_{st} - RT/2 \sim 30.6$ kJ mol^{-1}, which is in excellent agreement with $E_d = 30 \pm 2$ kJ mol^{-1} as measured from experiment. The increase in coverage in an apparently full monolayer will be addressed below. As the pressure increases q_{st} decreases to about 25 kJ mol^{-1}, with fairly large fluctuations, and is fairly independent of pressure through the formation of the bilayer and multilayers. For comparison, the isosteric heat at zero coverage is 27.9 kJ mol^{-1}, as computed from numerical integration.[9] The value of q_{st} computed from Eq. (2.5) around monolayer completion is in good agreement with the value computed from Eq. (2.7) from the experimental and simulation data. The isosteric heats of adsorption at 300 K were also calculated from simulations over a range of coverages. The value of the isosteric heat at zero coverage at 300 K is 25 kJ mol^{-1} from simulation and compares very well with the experimental data measured by Lal and Spencer in the range from 24.8 to 27.3 kJ mol^{-1}.[60] Agreement with the experimental data indicates that the energetics of the LS potential model are quite accurate, despite its simplicity.

In general, a pronounced decrease in q_{st} upon monolayer completion is expected because the adsorbate-adsorbate interactions in the first layer become more and more repulsive as the monolayer completes. When the first layer is completely filled subsequent molecules must

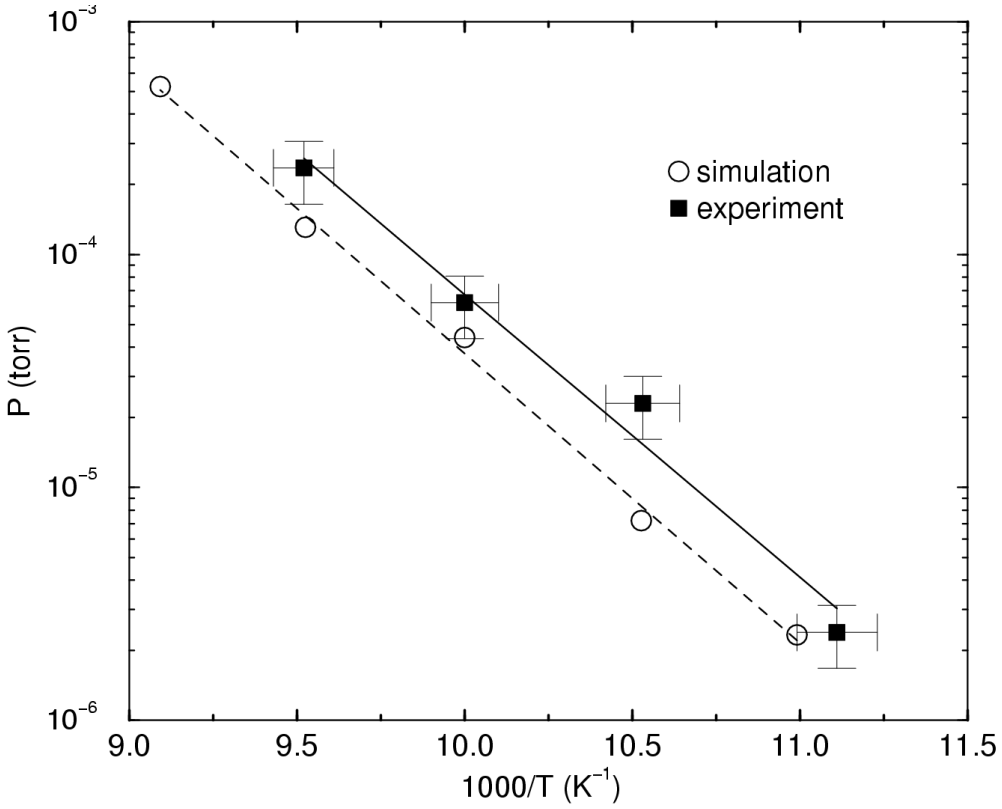

Figure 6: Isosteres from experiment and GCMC simulations. The filled squares are from experiments and circles are from simulations. The dashed and solid lines are fits to the simulation and experimental data, respectively. The slopes of the lines give $q_{\rm st}$ through Eq. (2.7). The values are 23 ± 2 and 24 ± 1 kJ mol^{-1} from experiments and simulations, respectively.

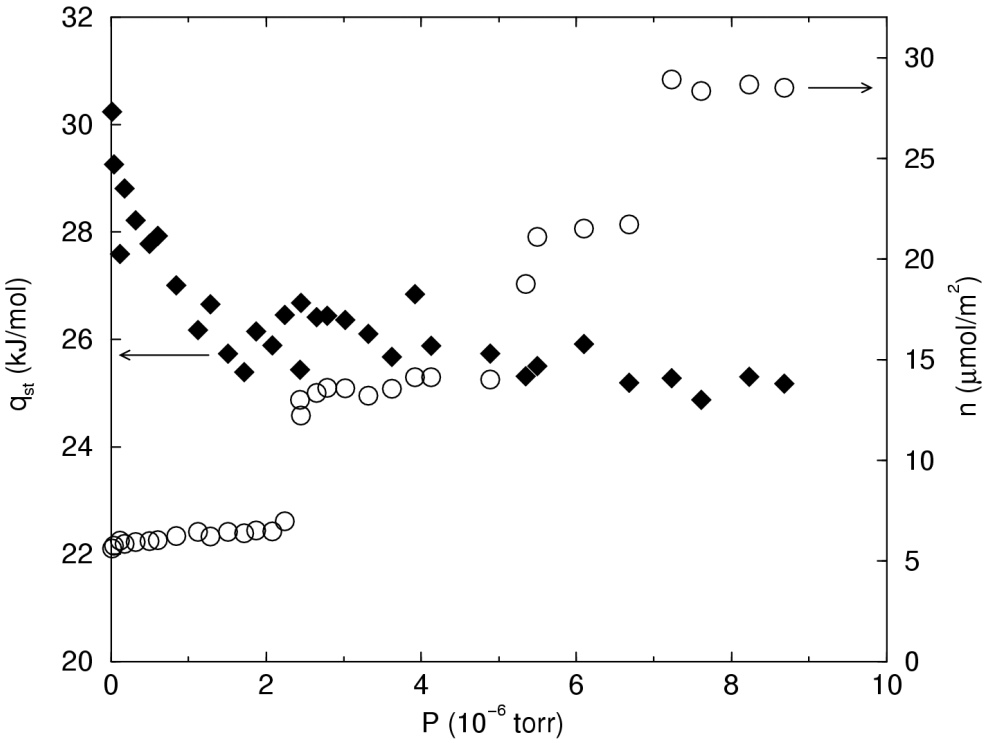

Figure 7: Isosteric heat of adsorption (diamonds, left axis) and adsorption isotherm (circles, right axis) from simulations of propane on graphite at 91 K as a function of pressure. The values of $q_{\rm st}$ are computed from Eq. (2.5).

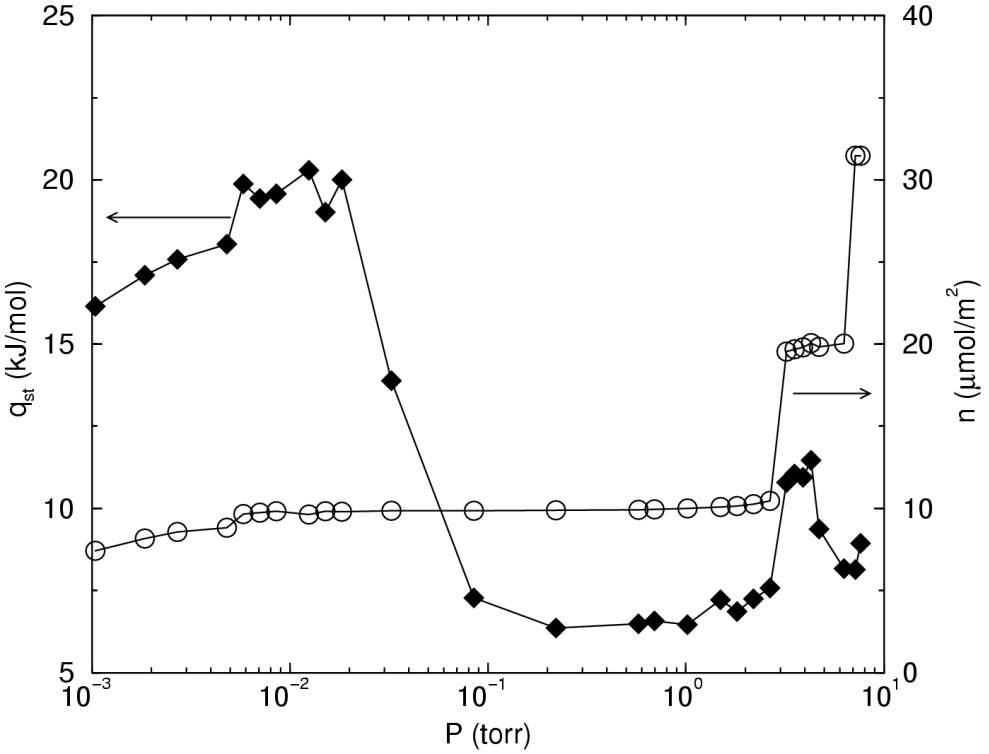

Figure 8: Isosteric heat of adsorption (diamonds, left axis) and adsorption isotherm (circles, right axis) for methane on graphite at 77 K simulations. The lines are to guide the eye.

occupy the second layer. Therefore, the q_{st} is expected to drop because of the relatively weak interactions between the second layer molecules and the graphite surface. This type of behavior has been noted for fluids such as methane, hydrogen, nitrogen, and carbon dioxide on graphite. [5, 61, 62, 63, 64]

We have plotted the isosteric heat and adsorption isotherm for methane on graphite at 77 K in Fig. 8 as an example. We have used the same parameters in these calculations for methane as those used by Jiang *et al.*[5], but with a potential cutoff of 5 σ. Note that the isosteric heat drops dramatically upon completion of the monolayer and remains low until the second layer is substantially occupied. The coverage in the first layer remains essentially constant from a pressure of about 0.1 torr until the second layer abruptly fills at a pressure of about 3 torr. The isosteric heat from about 0.1 to 3 torr is roughly constant with a value around 6.4 kJ mol^{-1}. This isosteric heat is due to molecules added to the second layer at zero coverage in the second layer, i.e., without any neighbors in the second layer.

We have verified that the isosteric heat from 0.1 to about 3 torr is due to addition of molecules into the second layer rather than in the first layer by computing the isosteric heat for a single methane molecule adsorbing on the frozen first layer of methane on graphite. This was done by numerical integration [9] with a resulting value of 6.1 kJ mol^{-1}, in good agreement with the plateau region of Fig. 8. It is generally accepted that the large drop in q_{st} on monolayer filling is due to the much lower solid-fluid interaction of molecules in the second layer. Note that q_{st} increases somewhat when the second layer becomes filled because of the attractive adsorbate-adsorbate interactions in the second layer. However, for propane on graphite q_{st} unexpectedly remains essentially constant as the bilayer and multilayers grow (Fig. 7).

2.4.3 Orientational ordering

In addition to the roughly constant isosteric heat as a function of coverage, another related phenomenon is the slight increase in coverage in the first layer with pressure after monolayer filling, but before second layer formation. This can be observed from simulations in Figs. 2, 3, and 4. The noise in the experiments makes it difficult to observe the increase in monolayer

density experimentally. The increase in monolayer coverage with increasing pressure observed for propane is not observed for simple fluids such as methane (see Fig. 8).

Both the absence of a drop in the isosteric heat upon monolayer completion and the slight increase in coverage in the monolayer with pressure can be explained in terms of an observed orientational transition of the adsorbed propane molecules. The angles between the plane of the propane molecules and the graphite basal plane for each of the molecules in the first layer have been measured from the GCMC simulations. The average angle of the propane molecules adsorbed in the first layer at 91 K is shown in Fig. 9 as a function of coverage. We observe that the average angle of the propane molecules depends linearly on the pressure for coverages in the first layer. Note that this graph starts from a coverage that is close to the monolayer limit. At zero coverage propane will have an angle close to zero (parallel with the surface). Although only results for 91 K are shown in Fig. 9, the same linear increase in angle with coverage can be observed for all temperatures studied.

The rotation of propane in the first layer can be viewed as a monolayer roughening transition that facilitates the growth of the second layer. This is because the first molecules to adsorb in the second layer do not adsorb onto a "bare" surface, but one that has many CH_3 groups protruding into the second layer. These groups serve to increase the isosteric heat in the second layer over the value for adsorption onto a perfect $\alpha = 0$ propane surface, where α is the average angle between the propane molecule and the graphite plane. We have verified this by comparing the energetics of a single propane molecule at 91 K on a relatively smooth propane monolayer and on a monolayer of propane molecules with an average angle of about 42°. The average angle for the monolayer molecules in the "smooth" surface was about 17°. We have computed the isosteric heat by performing Monte Carlo integrations of a single propane molecule interacting with the propane monolayer on graphite. This is analogous to the approach used by Cracknell and Nicholson[9] for computing the zero coverage isosteric heats. Our calculations yield the isosteric heat at zero coverage in the second layer on top of a full monolayer, given by

$$q_{st}^0 = RT - N_a \frac{\int u_s(\vec{r},\vec{\omega}) \exp[-\beta u_s(\vec{r},\vec{\omega})] d\vec{r} d\vec{\omega}}{\int \exp[-\beta u_s(\vec{r},\vec{\omega})] d\vec{r} d\vec{\omega}}, \tag{2.8}$$

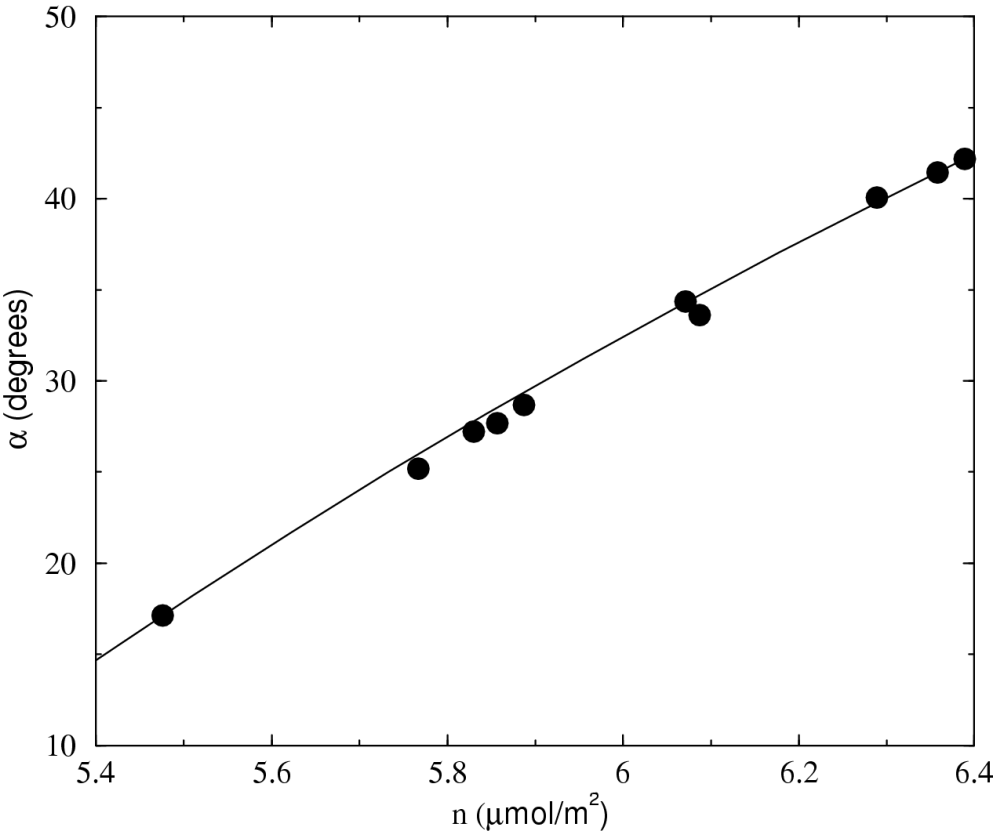

Figure 9: The average angle between the plane of the propane molecule and the graphite basal plane as a function of coverage for the 91 K isotherm. The circles are the data from the simulations, the line is the calculation from Eq. (2.13).

where u_s is the interaction potential between a propane molecule and the surface (graphite plus fixed monolayer), $\vec{r}$ is the center of mass and $\vec{\omega}$ represents the orientation of the propane molecule, and the integrals are over the volume of the system and all orientations of the propane molecule. We have averaged the results from 11 separate Monte Carlo integrations for each surface. The results are $q_{\rm st} = 21.8 \pm 0.3$ kJ mol^{-1} for the "smooth" propane monolayer and $q_{\rm st} = 26.7 \pm 0.4$ kJ mol^{-1} for the "rough" surface. The uncertainty is the estimate for one standard deviation of the mean. The latter value is in excellent agreement with $q_{\rm st}$ computed from simulations at the second layer transition shown in Fig. 7. The increase in $q_{\rm st}$ in the second layer with increasing α produces an isosteric heat that is roughly independent of coverage from monolayer to bilayer, as observed in Fig. 7.

Orientational ordering of molecules in the monolayer has been previously noted for other systems. For example, Bottani *et al.* have observed that carbon dioxide exhibits a coverage dependence in the average tilt angle of CO_2 relative to the graphite basal plane, [64] and Raut *et al.* noted that *n*-butane begins to tilt at high coverages on Pt (111) at low temperature in order to accommodate a higher coverage in the monolayer. [65]

We have computed the probability of observing a given propane tilt angle as a function of coverage for the 91 K isotherm. The probability distribution is distinctly bimodal, with a peak at about $\alpha = 8°$ and another broader peak centered at about 85-90° (Fig. 10). The probability distribution indicates that molecule are very likely to be in one of two states, one relatively flat with $\alpha \sim 0°$, and one almost perpendicular with $\alpha \sim 90°$. There is a low probability that a molecule will have an angle between 30 to 50°. The relative population of the two peaks in the bimodal distribution is seen to shift from $\alpha \sim 0°$ to $\alpha \sim 90°$ as the coverage increases. However, this shift is apparently not an orientational phase transition. Snap shots reveal that the molecules that are oriented perpendicular to the surface are not clustered together, but appear fairly randomly over the surface of the monolayer.

The linear dependence of the average angles of the propane molecules on coverage can be explained by a simple geometric theory. At low monolayer coverages, the molecule has all three sites (two CH_3 and one CH_2) in contact with the graphite surface ($\alpha \sim 0°$), whereas at higher monolayer coverages, only two sites contact the surface ($\alpha \sim 90°$). As the propane monolayer fills, molecules rotate from 0° to 90°. Based on the potential model used in the

simulation, we calculated that rotation of a single molecule in the monolayer from $\alpha = 0°$ to $90°$ leads to an increase in the system internal energy of about 6-7 kJ mol^{-1}. Insertion of a molecule from the gas phase into the monolayer decreases the internal energy of the system by about 30-40 kJ mol^{-1}, depending on the configuration. Hence, it is energetically favorable to rotate several molecules in order to accommodate another propane molecule adsorbing on the surface. Geometrically, rotation of a small number of molecules from $\alpha = 0°$ to $90°$ can provide enough surface area for the adsorption of a propane molecule from the gas phase onto the graphite surface. This accounts for the observation that the coverage in the first layer continues to increase slightly as the pressure increases. The increase in coverage with rotation can be quantified as follows. Assume that at some low pressure the total number of adsorbed propane molecules is N_l. Among these N_l molecules, N_0 molecules have an angle close to $0°$ (denoted α_0) and N_{90} molecules have an angle of about $90°$ (α_{90}) such that $N_l = N_0 + N_{90}$. The average angle can be written as

$$\langle \alpha_l \rangle = \frac{N_0 \alpha_0 + (N_l - N_0)\alpha_{90}}{N_l}. \tag{2.9}$$

Solving for N_0 we have

$$N_0 = \frac{\alpha_{90} - \langle \alpha_l \rangle}{\alpha_{90} - \alpha_0} N_l, \tag{2.10}$$

and likewise,

$$N_{90} = \frac{\langle \alpha_l \rangle - \alpha_0}{\alpha_{90} - \alpha_0} N_l. \tag{2.11}$$

At higher coverage, if the total number of adsorbed propane molecules is increased to N_h, we assume that N' of the N_0 molecules must rotate from α_0 to α_{90} in order to accommodate $\Delta N = N_h - N_l$ more molecules into the monolayer with an angle of $\alpha \sim 90°$. The average angle in the higher coverage state is

$$\langle \alpha_h \rangle = \frac{(N_0 - N')\alpha_0 + (N_{90} + \Delta N + N')\alpha_{90}}{N_h}. \tag{2.12}$$

Insertion of an additional molecule into the monolayer with an angle of α_{90} requires that s molecules already in the monolayer be rotated from the α_0 to the α_{90} orientation, giving

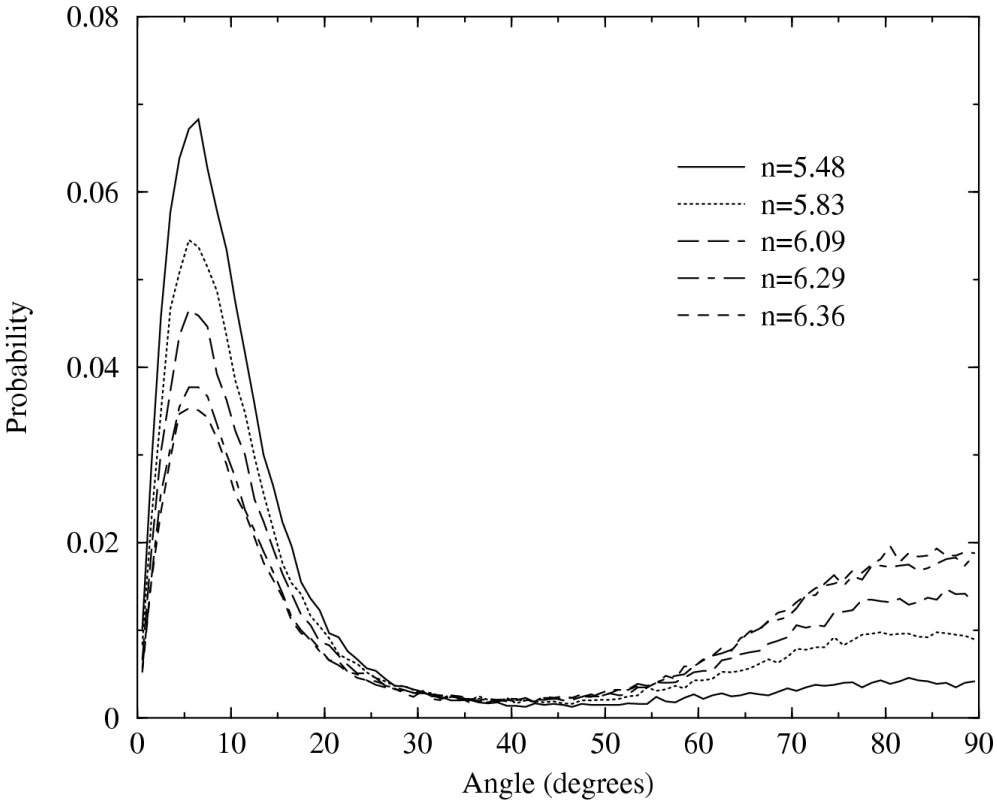

Figure 10: The probability distribution for the angle between the plane of the propane molecule and the graphite basal plane for coverages in the monolayer regime.

$N' = s\Delta N = s(N_h - N_l)$. Substituting N_0, N_{90}, N', and ΔN as functions of N_l and N_h into Eq. (2.12), we have

$$\langle \alpha_h \rangle = \frac{N_l}{N_h}\langle \alpha_l \rangle + \left(1 - \frac{N_l}{N_h}\right)\left[(1+s)\alpha_{90} - s\alpha_0\right]. \tag{2.13}$$

The curve predicted by Eq. (2.13) for the average angle as a function of coverage is nonlinear. However, the function is approximately linear over a narrow range of coverage. In our simulations $N_l = 5.48$ μmol/m^2 at the lowest pressure. The corresponding average angle is $\langle \alpha_l \rangle = 17.1°$. At any coverage higher than N_l, denoted as N_h, the average angle is given by $\langle \alpha_h \rangle$ from Eq. (2.13). Equation (2.13) contains three unknown parameters, α_0, α_{90}, and s. Nonlinear regression gives $\alpha_0 = 6°$, $\alpha_{90} = 85°$, and $s = 1.36$, when starting from reasonable initial guesses. The values of α_0 and α_{90} agree well with the data from Fig. 10. The fit to Eq. (2.13) gives a good match to the simulation data, as can be seen from Fig. 9, where the solid line is computed from Eq. (2.13) using the above values of the parameters.

2.5 CONCLUSION

We have presented computer simulation studies of propane adsorption on graphite. The simulation results agree well with experimental data for $q_{\rm st}$ near the 1-2 layering transition. The values of $q_{\rm st}$ computed from the isosteres method [Eq. (2.7)] and from simulation statistical method [Eq. (2.5)] are in very good agreement. The 1-2 layering transition from 90 to 105 K appears to be first order. The 1-2 layering transition pressures from simulations are generally in good agreement with experiments. The value of the 1-2 layering transition pressure from simulations was found to be very sensitive to the fluid-fluid interaction potential. The sharpness of the transition (first order or continuous) was not affected by the choice of a fluid-fluid potential, whereas a 5% decrease in the solid-fluid potential is apparently sufficient to change the transition from first order to continuous at 100 K. However, changes in the solid-fluid potential have comparatively moderate effect on the pressure at which the transition takes place. These observations underscore the importance of the accuracy of the fluid-fluid potential if one is interested in locating accurately the transition pressure.

We have observed unexpected behavior for the isosteric heat of adsorption across the first and second layer transitions. For simple fluids the isosteric heat exhibits a dramatic drop upon completion of the first layer and a slight recovery in q_{st} at the formation of the second layer. In contrast, the isosteric heat for propane is almost constant from monolayer completion to formation of the multilayer. An unusual slight increase in the monolayer coverage (before the onset of the second layer transition) was observed. Both of these phenomena can be explained by the orientational transition observed in simulations. Individual propane molecules rotate from orientations that are parallel to the graphite surface to an orientation almost perpendicular to the surface, having one methyl group pointing up from the monolayer. This orientational change provides a more attractive (roughened) surface for second layer adsorption, thereby increasing q_{st} and the coverage in the monolayer. The simulation data show that the average angle of propane in the monolayer depends linearly on coverage.

3.0 DEVELOPMENT OF A GRAPHITE POTENTIAL THAT INCLUDES INDUCTION AND QUADRUPOLE TERMS

3.1 INTRODUCTION

Molecular simulation studies of gas adsorption on graphitic sorbents requires accurate and computationally efficient descriptions of the solid-fluid potential energy surface (PES). For years people have been using the analytic integrated potential developed by Steele [57] to model adsorption of fluids on graphite.[32] This so-called 10-4-3 potential accounts for the van der Waals interaction between an adsorbate and atoms in the graphite based on the Lennard-Jones (LJ) potential. It has been common practice to assume that the electrostatic interactions between adsorbed molecules and the graphite are negligible compared to the LJ energies.[66] However, such an approximation may be a problem for strongly polar adsorbates, as will be discussed in this chapter, and needs more careful reconsideration.

The questions arise due to that carbon atoms in graphite have non zero polarizability and non zero quadrupole moment. The short ranged multipole and induction interaction between a strongly polar adsorbate and graphite may be too important to be neglected. The work by Bruch et al. showed that the electrostatic energies are important for systems of strongly polar molecules and dielectric solid for explaining some experimental observations.[67, 68] Vernov and Steele [69] estimated such interaction for water/graphite and found it can significantly change the adsorption behavior of water on graphite. A later experimental work by Whitehouse and Buckingham [70] confirmed that the quadrupole moment assigned to each carbon atom in a graphite crystal is about $-3.03 \times 10^{-40}\mathrm{Cm}^2$, which would be strong enough to account for a significant fraction of the interaction between strongly polar fluids and graphite based on the estimation of Vernov and Steele.[69] Nobody has ever evaluated

carefully the importance of induction energy between polar adsorbates and graphite, but we expect it to be stronger than the interactions involving quadrupole moment since it has a shorter range.

We can use two approaches in order to include the induction and multipole interaction into the total potential energy of polar adsorbate/graphite systems. Firstly, we can use an atom-explicit potential to describe the interaction between an adsorbate molecule and each individual carbon atom in the graphite. The total energy is calculated by summing up all the paired interaction. Dispersion, repulsion, multipole, and induction terms can all be computed in this way. But such an approach is computationally expensive, requiring a summation over each of the thousands of carbon atoms in graphite with each site of the fluid molecules in the system. An alternative approach is to use an integrated potential that accounts for all the adsorbent atoms in an effective way. This has been a very popular and useful approach for modeling solid-fluid interactions for many systems, including graphite. [71, 5, 7, 72] The advantage of integrated potentials, such as the 10-4-3 potential for graphite, is that they are computationally very efficient, only requiring the distance of the fluid molecule interacting site from the solid surface to compute the solid-fluid interaction potential. To our knowledge, there is still a lack of such simple and efficient solid-fluid potentials that compute multipole and dipole-induced dipole energies.

In this paper we present a set of integrated expression that accounts for dipole-quadrupole, quadrupole-quadrupole, and dipole-induced dipole interactions of polar fluids with graphite. We compare the interaction energy from these expressions and that from atom-explicit approach for a number of different polar fluids on graphite. We also compute adsorption isotherms from potentials with and without including the polar interactions and compare the results. We demonstrate that the polar terms are very important for some strongly polar fluids, while for weakly polar molecules the polar expressions may safely be excluded.

3.2 POTENTIAL DEVELOPMENT

We begin with the Fourier transformation approach used by Steele [57] to derive integrated expressions for the multipole and induction interactions. The potential energy of a single

fluid molecule interacting with a semi-infinite solid surface made up of periodically arranged atoms can be expressed as a Fourier series

$$U(\boldsymbol{r}) = \sum_{\boldsymbol{g}} \sum_{n} w_{\boldsymbol{g}}(z_n) \exp(i\boldsymbol{g} \cdot \boldsymbol{\tau}). \tag{3.1}$$

In Eqs. (3.1), $\boldsymbol{r}$ denotes the position of an interacting site on the adsorbate molecule relative to some origin located at an arbitrary point in the solid. $\boldsymbol{\tau}$ is the two dimensional translation vector for x and y directions spanning the graphite surface. $\boldsymbol{g}$ is a multiple of the reciprocal lattice vector defined to conform to the periodicity property of $U(\boldsymbol{r})$. z_n is the perpendicular distance from the carbon atom center of mass in the n^{th} graphite sheet to the fluid molecule interacting site. Correspondingly, an analytical expression for the Fourier coefficients $w_{\boldsymbol{g}}$ can be obtained from

$$w_{\boldsymbol{g}}(z_n) = \frac{1}{a_{\text{s}}} \int_{\boldsymbol{a}} \exp(-i\boldsymbol{g} \cdot \boldsymbol{\tau}) u(z_n, \boldsymbol{\tau}) d\boldsymbol{\tau}, \tag{3.2}$$

where $u(z_n, \boldsymbol{\tau})$ stands for the pairwise additive interaction potential between the adsorbate interacting site and a carbon atom in the graphite. a_{s} is the area of the graphene unit cell (see Fig. 11), and $\boldsymbol{a}$ denotes the limits of integration variable $\boldsymbol{\tau}$.

In the case where $u(z_n, \boldsymbol{\tau})$ is a function only of the separation distance between the fluid interacting site and the solid atom, $r = (z_n^2 + x^2 + y^2)^{\frac{1}{2}}$ (see Fig. 12), we can integrate over the orientation of $\boldsymbol{\tau}$ to obtain

$$w_{\boldsymbol{g}}(z_n) = \frac{2\pi n_0}{a_{\text{s}}} \int_0^{\infty} J_0(\boldsymbol{g}t) u(r) t dt, \tag{3.3}$$

where $t^2 = x^2 + y^2$, and n_0 is the number of carbon atoms in the graphene unit cell, J_0 is the Bessel function of the first kind. If $u(r)$ has an inverse power dependence on r such as in Lennard-Jones potentials, Eq. (3.3) can be integrated analytically. Substituting the integrated $w_{\boldsymbol{g}}$ back to Eq. (3.1) and summing over $\boldsymbol{g}$ we can establish a potential as a function only of z_n. Details of above derivation can be found in ref. [71].

Steele[57] found that truncation of Eq. (3.1) to the $\boldsymbol{g} = \boldsymbol{0}$ term is sufficiently accurate to give excellent agreement with the explicit sum in real space when the LJ potential was

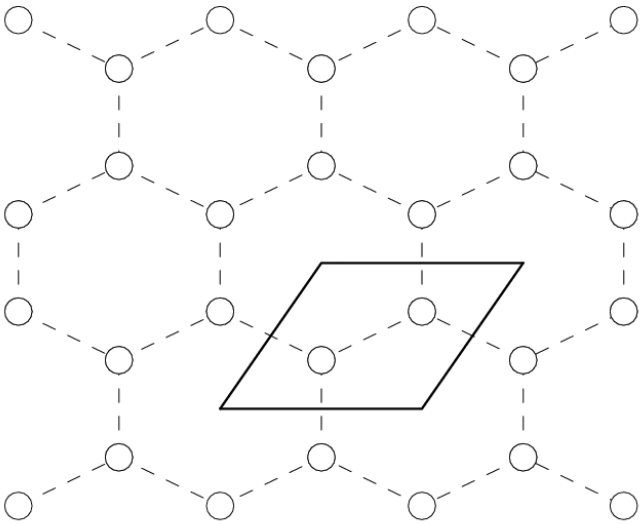

Figure 11: Graphite basal plane composed of hexagonal carbon lattices. The circles represent carbon atoms and the dashed lines show the hexagonal rings. The parallelogram in solid lines denotes one unit cell. In each unit cell there are 2 carbon atoms.

used. He derived the well-known 10-4-3 potential by simplifying the truncated series further to obtain

$$U_{\rm sf}(z) = 2\pi\epsilon_{\rm sf}{\sigma_{\rm sf}}^2\Delta\rho_{\rm s}\left[\frac{2}{5}\left(\frac{\sigma_{\rm sf}}{z}\right)^{10} - \left(\frac{\sigma_{\rm sf}}{z}\right)^{4} - \frac{\sigma_{\rm sf}^4}{3\Delta(0.61\Delta + z)^3}\right], \tag{3.4}$$

where z is the perpendicular distance between a fluid molecule interacting site and the solid surface ($n = 1$ layer of graphene), Δ is the distance between the graphene layers, $\rho_{\rm s} = n_0/(a_{\rm s}\Delta)$, and $\epsilon_{\rm sf}$ and $\sigma_{\rm sf}$ are the cross interaction LJ potential parameters between the fluid and graphite. In Eq. (3.4), the z^{-10} and z^{-4} terms are derived from the $n = 1$ term in Eq. (3.1). Repulsive terms arising from the $n > 1$ layers are neglected. The last term in Eq. (3.4) is from the integration of the attractive term in the remainder of the layers. The value 0.61Δ rather than Δ is used in the last term because the integration of the $n > 1$ attractive terms from $z + 0.61\Delta$ was found to give a more accurate representation of the atom-explicit sum.[57]

The similar procedures can be applied to obtain integrated expressions for induction or multipole interaction between a fluid molecule and the graphite as long as the pairwise

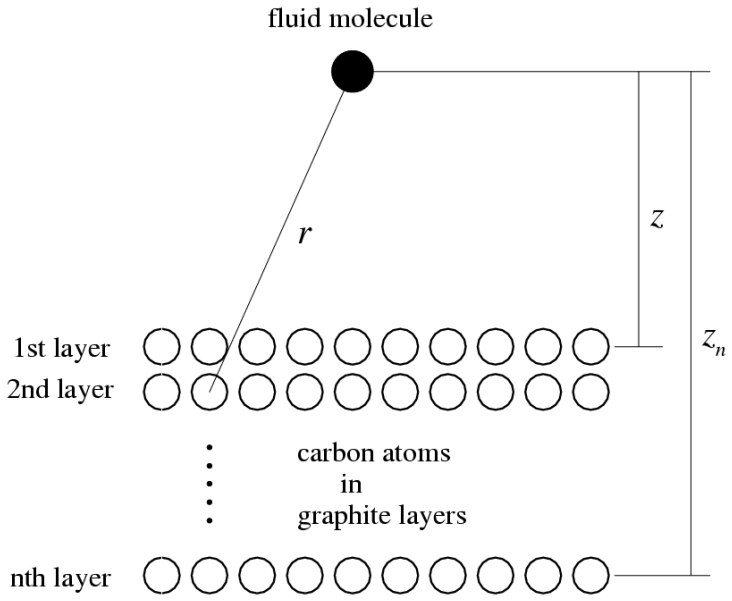

Figure 12: Schematic illustration of a fluid molecule interacting with the carbon atoms in graphite. The filled circle stands for the fluid molecule, the circles represent the carbon atoms in the graphene sheets.

potential to be used satisfies (1) it is a function only of the separation distance r; (2) it takes an inverse power dependence on r. For induction and multipole interaction potentials, both constraints are satisfied when we employ the angle average expressions for them. The angle averaged dipole-induced dipole interaction potential is given by [73]

$$u_{\mu\mathrm{i}}(r) = -\frac{\mu_{\mathrm{f}}^2 \alpha_{\mathrm{c}}}{(4\pi\epsilon_0)^2 r^6}, \tag{3.5}$$

where μ_{f} is the dipole moment of the fluid molecule, α_{c} is the scalar polarizability of carbon atoms in graphite, ϵ_0 is the vacuum dielectric constant, and r is the distance between the fluid molecule and a carbon atom. The angle averaged dipole-quadrupole interaction potential is [73]

$$u_{\mu\Theta}(r) = -\frac{\mu_{\mathrm{f}}^2 \Theta_{\mathrm{c}}^2}{kT(4\pi\epsilon_0)^2 r^8}, \tag{3.6}$$

where Θ_{c} is the quadrupole moment assigned to each carbon atom in the graphite, k is Boltzmann's constant, and T is the absolute temperature. Finally, the angle averaged quadrupole-quadrupole interaction function is [73]

$$u_{\Theta\Theta}(r) = -\frac{14}{5}\frac{{\Theta_{\mathrm{f}}}^2 {\Theta_{\mathrm{c}}}^2}{kT(4\pi\epsilon_0)^2 r^{10}}, \tag{3.7}$$

where Θ_{f} is the quadrupole moment of the fluid molecule. Eqs. (3.5)-(3.7) were derived from their angle explicit counterparts using orientation averaging approach.[73] Their accuracy are dependent on the temperature since the Boltzmann weighting factor is included during the averaging process. We will discuss this issue in a later section.

Substituting Eq. (3.5), (3.6) and (3.7) into Eq. (3.3) and integrating, we obtain the following expressions after simplifying the $\boldsymbol{g} = \mathbf{0}$ truncated series. The integrated dipole-induced dipole potential is given by

$$U_{\mu\mathrm{i}}(z) = -\frac{\Delta\rho_{\mathrm{s}}\pi}{2}\frac{\mu_{\mathrm{f}}^2 \alpha_{\mathrm{c}}}{(4\pi\epsilon_0)^2}\left[\frac{1}{z^4} + \frac{1}{3\Delta(z+\Delta)^3}\right]. \tag{3.8}$$

The integrated dipole-quadrupole interaction potential is

$$U_{\mu\Theta}(z) = -\frac{\Delta\rho_{\mathrm{s}}\pi}{3}\frac{\mu_{\mathrm{f}}^2 \Theta_{\mathrm{c}}^2}{kT(4\pi\epsilon_0)^2}\left[\frac{1}{z^6} + \frac{1}{5\Delta(z+\Delta)^5}\right]. \tag{3.9}$$

The integrated quadrupole-quadrupole interaction potential betweeen the adsorbate molecule and solid adsorbent is

$$U_{\Theta\Theta}(z) = -\frac{7\Delta\rho_s\pi}{10}\frac{\Theta_f^2\Theta_c^2}{kT(4\pi\epsilon_0)^2}\left[\frac{1}{z^8} + \frac{1}{7\Delta(z+\Delta)^7}\right]. \tag{3.10}$$

Similar to Steele's 10-4-3 function, potentials in Eqs. (3.8)−(3.10) are only dependent on the perpendicular distance between fluid molecules and the graphite surface. In contrast to the 10-4-3 function, we have not used empirical parameters like 0.61 because the contribution of z^3, z^5, and z^7 terms in Eqs. (3.8)−(3.10) respectively are quite small compared with the LJ interaction, and the use of empirical parameters will not change the total potential energy significantly.

We omit the dielectric properties of the graphite in Eqs. (3.5)−(3.10). Strictly speaking, the graphite carbon atoms in outer layer and inner layers are in different dielectric environments. Including such difference explicitly in Eqs. (3.5)−(3.7) would have made the derivation of Eqs. (3.8)−(3.10) quite complicated. However, there exists a simple way to compensate the imperfect dielectric response of graphite in calculating the interaction of fluids with graphite surface. Bruch *et al.* had shown that we can account for the potential modification due to the dielectric properties of the graphite by simply multiplying the results from Eqs. (3.8)−(3.10) by a factor of 0.619.[74]

3.3 RESULTS AND DISCUSSION

3.3.1 Discussion on the angle average approach

We have used angle averaged expressions for the induction and multipole interaction in the derivation of Eqs. (3.8)−(3.10). Eqs. (3.5)−(3.7) were obtained by using

$$\bar{u}_{ab} = \frac{\int\int u_{ab}\exp\left(-u_{ab}/kT\right)d\omega_a d\omega_b}{\int\int \exp(-u_{ab}/kT)d\omega_a d\omega_b} \tag{3.11}$$

to average the interaction energy between molecules a and b with relative orientations while holding r_{ab} fixed.[73] The Boltzmann weighting factor $\exp(-u_{ab}/kT)$ is included in order to

take into account the fact that statistically the molecules spend more time in those orientations for which the energy is low. Physically the use of this effective method corresponds to the assumption that r_{ab} does not change appreciably as molecules undergo a rotation. In order for the averaged potential to be a good approximation, it is required that the difference in interaction energy with two relative orientations ω_1 and ω_2 between two molecules,

$$|u_{\omega_1} - u_{\omega_2}| << kT. \tag{3.12}$$

We performed a few test calculations of the induction and multipolar energy of polar adsorbates on graphite using angle explicit induction and multipole potentials instead of Eqs. (3.5)−(3.7). We found that Eq. (3.12) is satisfied for typical computations of the interaction between a polar gas molecule and a carbon atom in graphite. Taking water/graphite as an example, at a distance $r_{\min}$ where the total interaction potential reaches minimum, the energy difference due to polar interactions between two typical orientations (ω_1=HOH plane parallel to the graphite surface, and ω_2=HOH plane perpendicular to the graphite surface) is about 0.36 kJ/mol, which requires the temperature $T >> 45$ K. In practical simulations, this is commonly satisfied. On the other hand, the corresponding $r_{\min}$ change between the two orientations for water/graphite is about 0.06 Å, which also satisfies the assumption that r_{ab} is not changed appreciably.

For certain very nonspherical fluid molecules, such as CO_2, the temperature limitation of Eq. (3.12) may elevate. Similar test calculations were performed on CO_2. It was found that for two typical orientations such as the linear CO_2 parallel and perpendicular to the surface, the corresponding change in $r_{\min}$ can be as high as 0.9 Å. The polar interaction difference for these two orientations is about 1.21 kJ/mol, which requires the temperature $T >> 145$ K. That indicates the application of Eqs. (3.8)−(3.10) would be inappropriate for calculating the polar energies of CO_2/graphite at temperatures below or near 145 K. We should point out that the linear CO_2 molecule (another example is CS_2) represents an nearly extreme case. According to our test calculations, Eq. (3.12) is usually satisfied when the temperature is above 150 K for most of the fluids studied (for those an angle explicit potential exists) in this work.

3.3.2 Ion/graphite interaction

In practical simulations one often uses charge sites rather than point multipoles to calculate the fluid-fluid electrostatic interactions. The point multipole approximation only needs to be employed for the solid-fluid potential. One may suggest calculate the multipolar energy of fluid/graphite by summing up integrated fluid charge/carbon point multipole. In this section we will show that such an approach is not appropriate.

The interaction between the ith carbon atom in graphite and a fluid molecule with n_{s} charge sites is given by

$$u_i = -\frac{1}{2}\boldsymbol{\mu}_i^{ind} \cdot \boldsymbol{E}_i^{\mathrm{f}}. \tag{3.13}$$

$\boldsymbol{\mu}_i^{ind}$ stands for the induced dipole on the carbon atom i, and $\boldsymbol{E}_i^{\mathrm{f}}$ is the electric field acting on the carbon atom i due to the charge sites on the fluid molecule. They are given by

$$\boldsymbol{\mu}_i^{ind} = \alpha_{\mathrm{c}} \boldsymbol{E}_i^{\mathrm{f}}, \tag{3.14}$$

and

$$\boldsymbol{E}_i^{\mathrm{f}} = \sum_j^{n_{\mathrm{s}}} \frac{q_j}{r_{ij}^3} \boldsymbol{r}_{ij}, \tag{3.15}$$

where n_{s} is the number of charge sites on the fluid molecule, q_j is the charge of site j on the fluid molecule, and $\boldsymbol{r}_{ij}$ is the vector from site j on the fluid molecule to carbon atom i, given by

$$\boldsymbol{r}_{ij} = \boldsymbol{r}_i - \boldsymbol{r}_j. \tag{3.16}$$

Then, Eq. (3.13) becomes

$$u_i = -\frac{1}{2}\alpha_{\mathrm{c}} \boldsymbol{E}_i^{\mathrm{f}} \cdot \boldsymbol{E}_i^{\mathrm{f}} = -\frac{1}{2}\frac{\alpha_{\mathrm{c}}}{(4\pi\epsilon_0)^2}\left(\sum_{i=1}^{n_{\mathrm{s}}} \frac{q_i^2}{r_i^4} + 2\sum_{i=1}^{n_{\mathrm{s}}}\sum_{j>i}^{n_{\mathrm{s}}} \frac{q_i q_j (\boldsymbol{r}_i \cdot \boldsymbol{r}_j)}{r_i^3 r_j^3}\right). \tag{3.17}$$

Unfortunately, we cannot apply the procedure used in deriving Eqs. (3.8)-(3.10) to obtain an integrated form for Eq. (3.17) because it is not a function only of the separation distance between the fluid molecule charge site and the carbon atom.

If the fluid particle is an ion, the second term on the right hand side of Eq. (3.17) disappears. Thus, u_i is only a function of r_i and integrated expressions for the ion/graphite

induced dipole, ion/graphite quadrupole interaction can be derived. The ion/induced-dipole interaction is given[73] by

$$u_{\mathrm{ii}}(r) = -\frac{q_{\mathrm{ion}}^2 \alpha_{\mathrm{c}}}{2(4\pi\epsilon_0)^2 r^4}. \tag{3.18}$$

The integrated ion/induced-dipole interaction potential is

$$U_{\mathrm{ii}}(z) = -\frac{\Delta\rho_{\mathrm{s}}\pi}{2}\frac{q_{\mathrm{ion}}^2 \alpha_{\mathrm{c}}}{(4\pi\epsilon_0)^2}\left[\frac{1}{z^2} + \frac{1}{\Delta(z+\Delta)}\right]. \tag{3.19}$$

The ion/point-quadrupole interaction potential is given[73] by

$$u_{\mathrm{i}\Theta}(r) = -\frac{1}{20}\frac{q_{\mathrm{ion}}^2 {\Theta_{\mathrm{c}}}^2}{kT(4\pi\epsilon_0)^2 r^6}. \tag{3.20}$$

The corresponding integrated potential is

$$U_{\mathrm{i}\Theta}(z) = -\frac{\Delta\rho_{\mathrm{s}}\pi}{40}\frac{q_{\mathrm{ion}}^2 \Theta_{\mathrm{c}}^2}{kT(4\pi\epsilon_0)^2}\left[\frac{1}{z^4} + \frac{1}{3\Delta(z+\Delta)^3}\right]. \tag{3.21}$$

In Eqs. (3.18)−(3.21), q_{ion} stands for the charge on the fluid ion. Note that Eq. (3.18) only accounts for the first term in the right hand side of Eq. (3.17). Therefore, it is incorrect to calculate the dipole-induced dipole energy between a fluid *molecule* and the graphite by summing up Eq. (3.19) over n_s.

3.3.3 Self consistency

In the derivation of integrated formulas we did not include polarization self consistency. Such approximation simplified the derivations significantly. In comparison to Eq. (3.14), the dipole induced on a carbon atom i including polarization self consistency is calculated as

$$\boldsymbol{\mu}_i^{ind} = \alpha_{\mathrm{c}}\boldsymbol{E}_i = \alpha_{\mathrm{c}}(\boldsymbol{E}_i^{\mathrm{f}} + \boldsymbol{E}_i^{\mathrm{c}}), \tag{3.22}$$

where $\boldsymbol{E}_i^{\mathrm{c}}$ is the local electric field resulting from the induced dipoles on the other carbon atoms. Here we neglected the induction effect on the fluid molecule from the carbon atoms. For a single fluid molecule the total induction energy is

$$U_{\mu\mathrm{i}} = -\frac{1}{2}\sum_{i=1}^{N_{\mathrm{c}}} \boldsymbol{\mu}_i^{ind}\cdot\boldsymbol{E}_i^{\mathrm{f}} = -\frac{1}{2}\sum_{i=1}^{N_{\mathrm{c}}} \alpha_{\mathrm{c}}\left(\boldsymbol{E}_i^{\mathrm{f}}\cdot\boldsymbol{E}_i^{\mathrm{f}} + \boldsymbol{E}_i^{\mathrm{f}}\cdot\boldsymbol{E}_i^{\mathrm{c}}\right), \tag{3.23}$$

where summation is over all N_c carbon atoms in graphite. In Eq. (3.23), the first term inside the summation stands for the contribution from the permanent dipole on the fluid molecule, and the second term comes from the self consistency of carbon atoms. $\boldsymbol{E}_i^f$ is given by Eq. (3.15). The local electric field at carbon atom i due to self consistency, $\boldsymbol{E}_i^c$, is given by

$$\boldsymbol{E}_i^c = \sum_{k \neq i}^{N_c} \frac{1}{r_{ik}^3} \left[\frac{3\boldsymbol{r}_{ik} \cdot \boldsymbol{\mu}_k^{ind}}{r_{ik}^2} \boldsymbol{r}_{ik} - \boldsymbol{\mu}_k^{ind} \right], \tag{3.24}$$

where $\boldsymbol{r}_{ik}$ is the vector from carbon atom k to carbon atom i,

$$\boldsymbol{r}_{ik} = \boldsymbol{r}_i - \boldsymbol{r}_k. \tag{3.25}$$

Note that $\boldsymbol{E}_i^c$ is dependent on $\boldsymbol{\mu}_i^{ind}$. The induced dipole on each carbon atom must be computed by iterating Eqs. (3.22) and (3.24) until $\boldsymbol{\mu}_i^{ind}$ converges.

We have performed test calculations for several polar fluids on graphite and found the self consistency polarization effect on the total potential energy can be safely neglected. Taking acetone/graphite as an example, at 300 K the potential minimum with and without including polarization self consistency are at -35.57 kJ/mol and -35.27 kJ/mol, respectively. Note that the potential model we used for acetone has a dipole of 2.7 Debye, which makes it the most strongly polar molecule we studied in this paper. For other less polar molecules, the self consistency effect on the potential energy minimum is even smaller in percentage. This is not surprising. Previous work by Jedlovszky and Pálinkás [75] compared polarizable and non-polarizable potentials for acetone by molecular simulation. They found that the contribution from self consistency calculation is about 9% of the total energy for bulk liquid acetone at 298 K. The polarizability of acetone is 5.76 $\times 10^{-40}$ C^2m^2/J, whereas the polarizability of a carbon atom is only 1.76 $\times 10^{-40}$ C^2m^2/J. In this light, the polarization self consistency in the induction term of the solid-fluid interaction does not contribute substantially to the total energy of the system given the smaller polarizability of the carbon atoms.

3.3.4 Comparison with atom-explicit potentials

We have calculated the interaction energy for the water/graphite, ammonia/graphite, and carbon dioxide/graphite from the integrated expressions, Eqs. (3.8) and (3.9), and compared the results with the atomistic angle averaged potentials, Eqs. (3.5), and (3.6). The atom-explicit potentials used ten graphene layers, each containing 1080 carbon atoms, about 58 Å on a side.The above system size was based on trial calculations and was found to contain more than enough atoms to accurately model the semi-infinite surface. For each calculation only a single adsorbate molecule was used (zero coverage limit). The fluid molecule was placed above the center of the graphite surface and the polar energy was computed by summing Eqs. (3.5) and (3.6) over all carbon atoms.

The LJ and electrostatic parameters for several polar molecules are given in Table 3. We should point out that there are often several different potential models available for a given molecule. Our goal in this work is to study the effect of including fluid-graphite polar interactions, so we have chosen the potential models in Table 3 rather arbitrarily. The values of the parameters for carbon atoms in graphite are $\sigma_s = 0.340$ nm, $\epsilon_s/k = 28.0$ K, $\Delta = 0.335$ nm, $\rho_s = 114$ nm^{-3},[76] and $\alpha_c = 1.76 \times 10^{-40}$ C^{2}m^2/J.[77] The standard Lorentz-Berthelot rules were used to obtain the values of σ_{sf} and ϵ_{sf}. The results from the atom-explicit potentials, Eqs. (3.5)−(3.7), were compared with the integrated potentials given in Eqs. (3.8)−(3.10).

In Figs. 13, 14, and 15 we compare potential energy surfaces computed from the nonpolar 10-4-3 potential, the integrated polar potentials, and the atom explicit polar potentials at 300 K, for water, ammonia, and carbon dioxide, respectively. The integrated expressions are in excellent agreement with the atom-explicit summation results. Taking the atom-explicit potentials as the standard, the errors in the integrated potentials are less than 1% over the range where energy is negative. We note, however, that the integrated potentials are biased with respect to the atom explicit potentials, always giving a slightly less attractive potential.

The contributions to the solid-fluid potential energy at the potential minimum are tabulated in Table 4 for several fluid molecules, the contributions to the total potential energy from the 10-4-3, induction ($U_{\mu i}$), dipole-quadrupole ($U_{\mu\Theta}$), and quadrupole-quadrupole

Table 3: The Lennard-Jones and multipole parameters for fluid-fluid potentials.

	ϵ_{ff}/k (K)	σ_{ff} (Å)	μ (D)	Θ (10^{-40}Cm^2)	Source
H_2O	78.02	3.152	1.85	-	[78]
NH_3	140	3.40	1.47	-	[78]
CO_2[1]	125.3	3.035	-	-12.2	[76]
Acetone[2]	85(Methyl)	3.88(Methyl)	2.70	-	[75]
	52.84(C)	3.75(C)			
	105.68(O)	2.96(O)			
N_2	96.42	3.663	-	-4.7	[79, 80]
Cl_2	357	4.115	-	10.79	[79, 81]
CO	110	3.59	0.112	-8.33	[79, 80]
H_2S	250	3.73	0.97	-	[82, 77]
SO_2	369.3	3.895	1.63	-	[79]
CS_2	488	4.438	-	12.0	[79, 83]
C_2H_4	219	4.20	-	6.67	[79, 80]
C_2H_5OH	327.8	4.575	1.69	-	[79]
N_2O	189	4.59	-	-11.67	[79, 80]

[1] CO_2 is a two site LJ model. [2] Acetone is a four site LJ model.

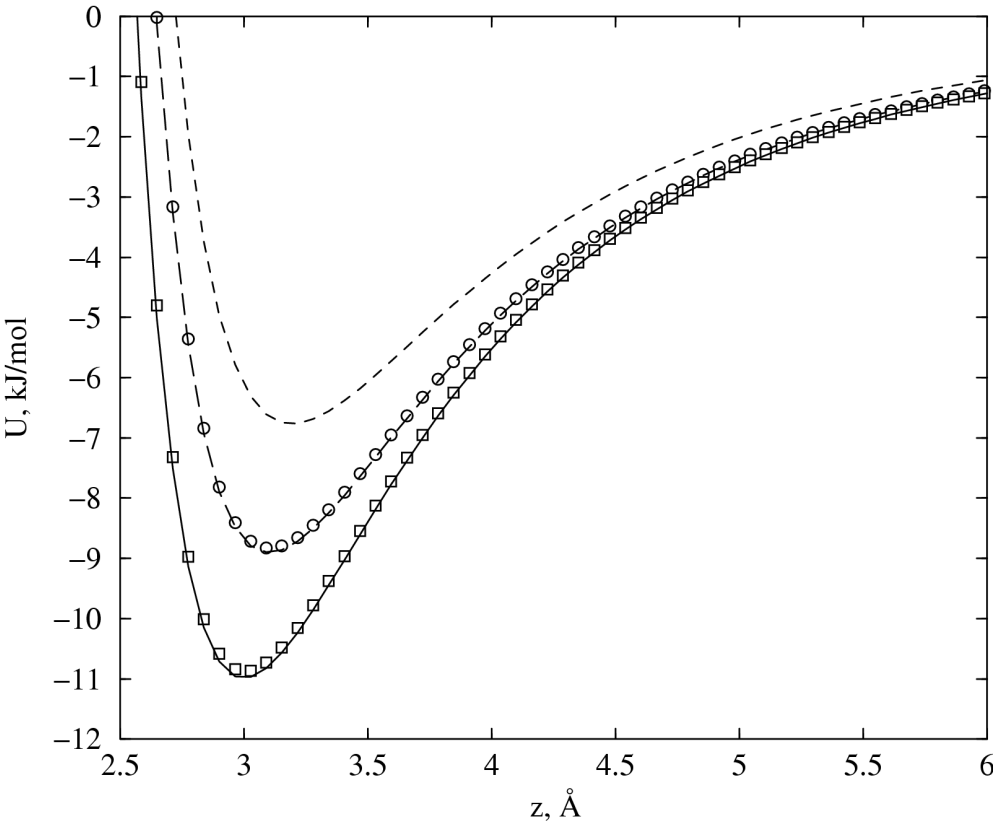

Figure 13: Comparison of potential models for water at 300 K. The dotted line is computed from the 10-4-3 potential, the dashed line is from 10-4-3 plus atomistic induction from Eq. (3.5), and the circles are from 10-4-3 plus the integrated induction term, Eq. (3.8). The solid line is the 10-4-3 plus atomistic induction and quadrupole-dipole interactions, Eqs. (3.5) and (3.6). The squares are from 10-4-3 plus the integrated induction and quadrupole-dipole interactions, Eqs. (3.8) and (3.9).

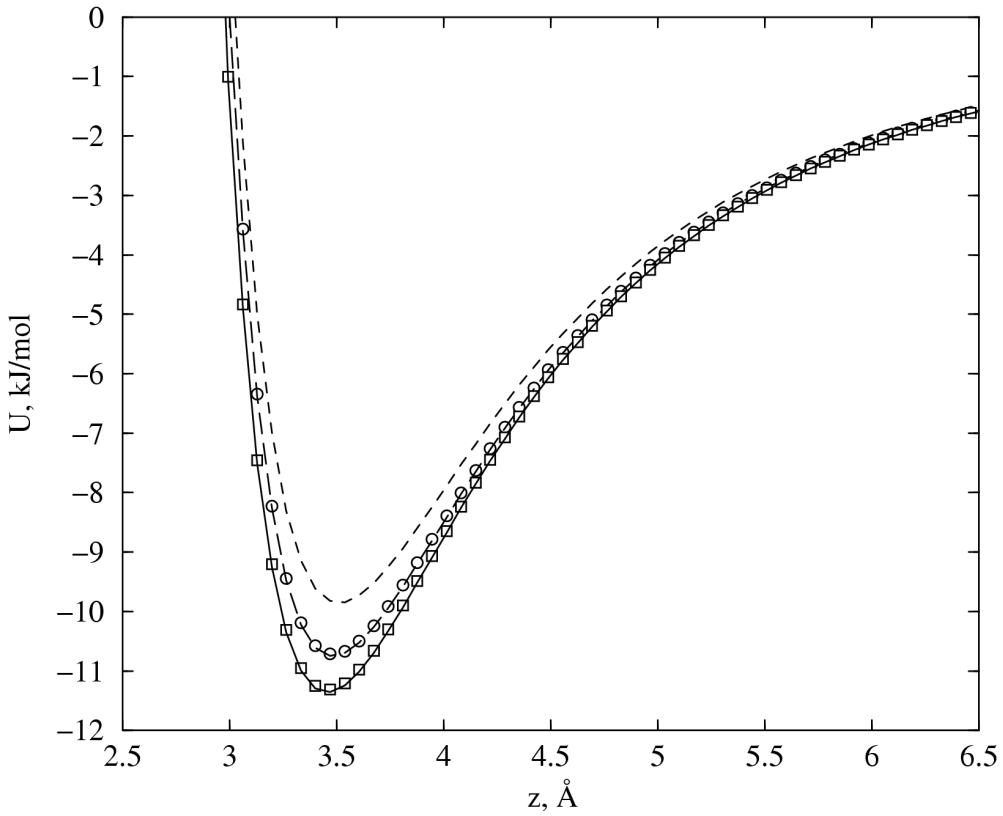

Figure 14: Comparison of potential models for ammonia at 300 K. The symbols have the same meaning as in Fig. 13.

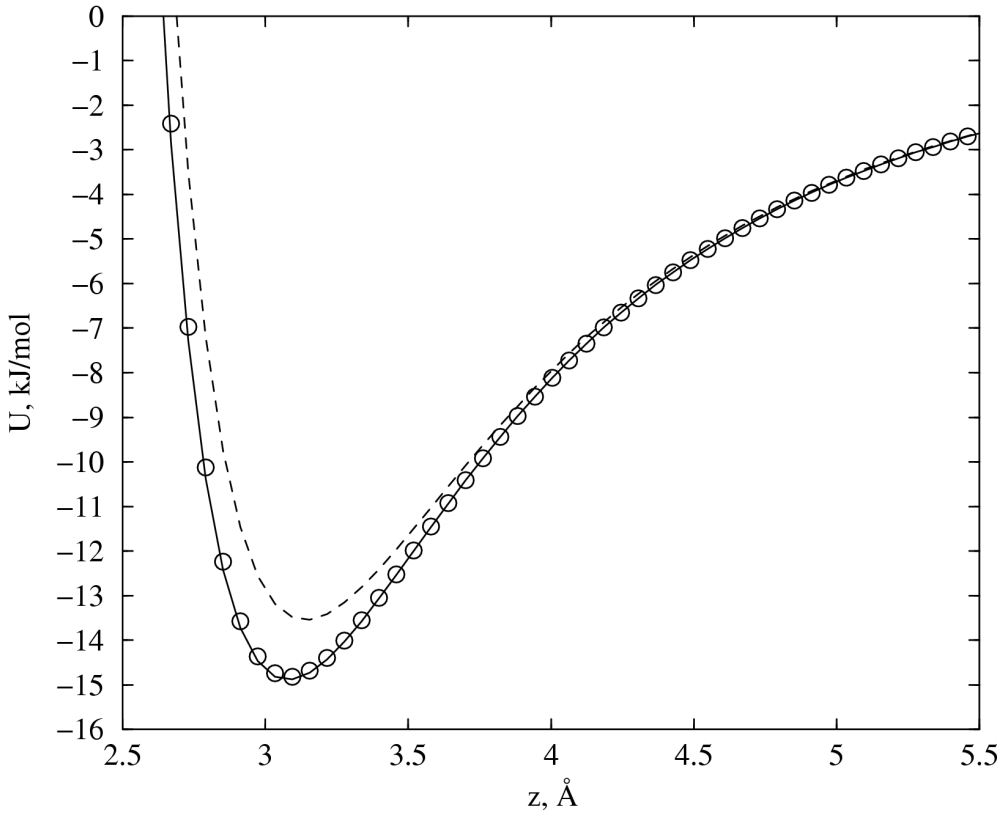

Figure 15: Comparison of potential models for carbon dioxide at 300 K. The dotted line is computed from the 10-4-3 potential, the dashed line is from 10-4-3 plus atomistic quadrupole-quadrupole interaction from Eq. (3.7), and the circles are from 10-4-3 plus the integrated quadrupole-quadrupole interaction term, Eq. (3.10).

($U_{\Theta\Theta}$) are evaluated at $z_{\min}$, the minimum in U_t. For strongly polar molecules like water and ammonia, the dipole-induced dipole and dipole-quadrupole interaction contribute significantly to the total energy. For carbon dioxide, the quadrupole-quadrupole interaction is about 10 percent of the total energy at the PES minimum.

For the water/graphite system the electrostatic and induction terms adds about -4.7 kJ/mol to the total energy at the PES minimum (see Table 4), which is about 40% of the total energy on the basis of the water potential model we employed. It is difficult to judge if such a high fraction of contribution is accurate or not because the percentage is also a function of potential we choose for water. The existing theoretical and experimental studies give binding energies for water/graphite ranging from -6.9 kJ/mol to -24.0 kJ/mol,[69, 84, 66, 85, 86] comparing with our result, -11.0 kJ/mol. However, it is no doubt that the induction and electrostatic contributions to the total energy as much as -4.7 kJ/mol is not negligible when we perform simulation of water/graphite.

The dominant contribution to the energy in Eqs. (3.8)$-$(3.10) comes, not surprisingly, from the first term in each equation, which accounts for the interactions with the first surface graphene sheet in graphite. The summation over the deeper layers is accounted for by the second term in each of the equations, which contains the Δ term. This second term is typically only about 5% of the polar interaction energy near the PES minimum. Therefore, retaining only the first terms in Eqs. (3.8)$-$(3.10) is a very good approximation for most fluid-graphite systems.

3.3.5 Comparison with the image potential approximation

Another method for computing the dipole-induced dipole interaction of an adsorbate molecule with a polarizable adsorbent is the image charge potential approximation [87, 88]. The image charge potential is given by

$$u_{\mu i}(z) = -\frac{\mu_{\rm f}(1+\cos^2\theta)}{16(4\pi\epsilon_0)(z-\delta)^3}, \tag{3.26}$$

where θ is the angle between the direction of the dipole moment of the adsorbate molecule and the normal to the surface, and δ is the distance of the image charge from the surface.

Table 4: Contribution of polar interactions at the potential minimum for several fluids on graphite, $T = 300$ K, energies are in kJ/mol.

	U_t	U_{LJ}	$U_{\mu i}$	$U_{\mu\Theta}$	$U_{\Theta\Theta}$
H_2O	-10.98	-6.31	-2.49	-2.18	-
NH_3	-11.35	-9.82	-0.92	-0.61	-
CO_2[1]	-14.88	-13.48	-	-	-1.40
Acetone[2]	-35.57	-30.70	-3.03	-1.84	-
N_2	-9.00	-8.91	-	-	-0.09
Cl_2	-20.45	-19.75	-	-	-0.30
CO	-9.61	-9.29	-0.005	-0.004	-0.32
H_2S	-15.27	-14.64	-0.38	-0.25	-
SO_2	-20.35	-18.74	-0.92	-0.54	-
CS_2	-25.70	-25.46	-	-	-0.24
C_2H_4	-15.98	-15.88	-	-	-0.10
C_2H_5OH	-22.85	-21.73	-0.75	-0.38	-
N_2O	-16.78	-16.57	-	-	-0.21

[1] CO_2 molecule is parallel to the surface. [2] Acetone molecular plane is parallel to the surface.

It is a common approximation to take the value of θ to be zero. The largest uncertainty in Eq. (3.26) is in the value of δ. The recommended value of δ is half the distance between carbon layers in graphite, which is $\Delta/2$.[87, 88] However, if we equate Eq. (3.26) to (3.8), we can solve for the value of δ that would give the same value as $U_{\mu i}$ from Eq. (3.8). To consider the simple case where the z^4 term in Eq. (3.8) dominates, δ is then given by

$$\delta(z) = z - \left(\frac{z^4\epsilon_0}{\alpha_c\rho_s\Delta}\right)^{\frac{1}{3}}. \tag{3.27}$$

This shows that for graphene the value of δ is not a constant, but depends on the distance between the dipole and the surface. We calculated $U_{\mu i}$ for several fluid molecules to compare the Eqs. (3.8) and (3.26) and found that in most cases the image charge potential is prone to overestimate the induction energy at the PES minimum. Fig. 16 shows an example for calculation of induction energy of water/graphite using Eq. (3.26) and Eq. (3.8).

3.4 APPLICATIONS

3.4.1 Isosteric heat of adsorption at zero coverage

We have computed the zero coverage isosteric heat of adsorption for a number of different polar molecules on graphite in order to assess the importance of multipole and induction terms. The isosteric heat of adsorption at zero coverage, $q_{\rm st}^0$, can be computed from [58]

$$q_{st}^0 = RT - N_a\frac{\int_V u_{\rm s}(\boldsymbol{r},\boldsymbol{\omega})\exp[-\beta u_s(\boldsymbol{r},\boldsymbol{\omega})]d\boldsymbol{r}d\boldsymbol{\omega}}{\int_V \exp[-\beta u_s(\boldsymbol{r},\boldsymbol{\omega})]d\boldsymbol{r}d\boldsymbol{\omega}}, \tag{3.28}$$

where $u_{\rm s}$ is the interaction energy between the graphite surface and a molecule located at position $\boldsymbol{r}$ with orientation $\boldsymbol{\omega}$, $\beta = 1/kT$ and N_a is Avogadro's number. We used a Monte Carlo integration method with 1×10^7 trial insertions in order to evaluate the integral. The 10-4-3 potential and the 10-4-3 plus polar interactions were used in our calculations.

The zero coverage isosteric heats of adsorption for several fluids are given in Table 5. It can be seen that in most cases, the interaction involving the quadrupole of fluids can be neglected. The only exception is carbon dioxide, for which the quadrupole-quadrupole interaction accounts for more than 10% of the total energy at the PES minimum. On

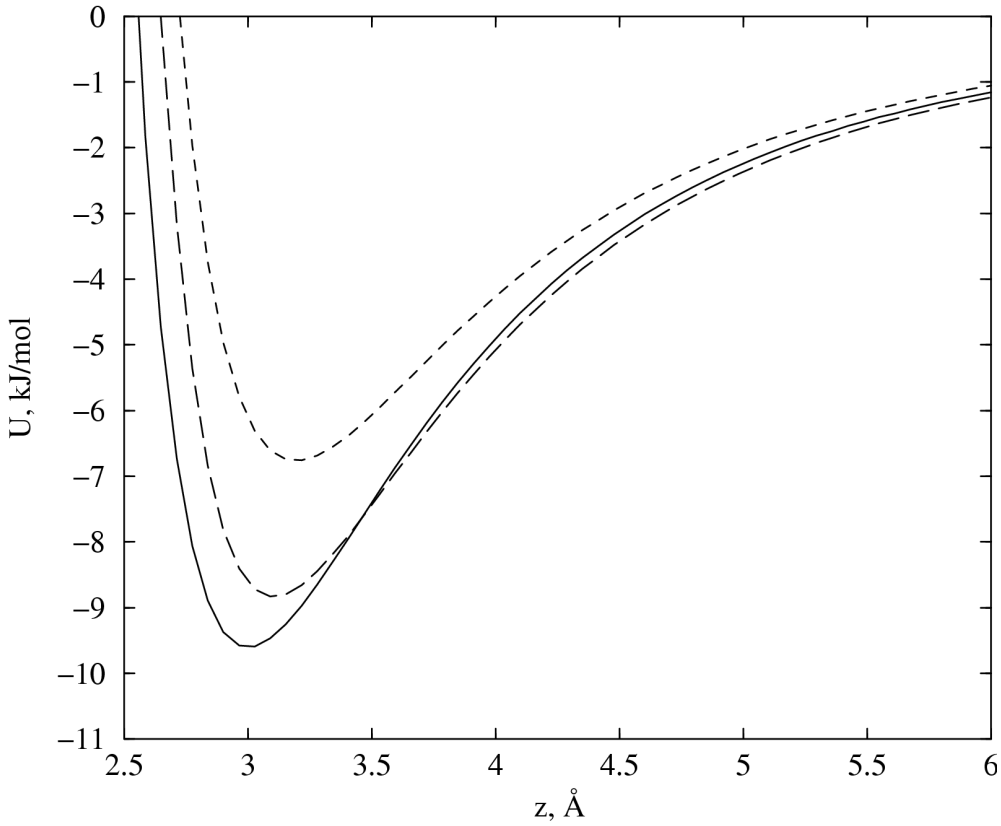

Figure 16: Calculation of the induction energy the using image potential, Eq. (3.26), and Eq. (3.8) for water molecule on graphite. The short dashed line is from 10-4-3 potential, the long dashed line is from 10-4-3 plus Eq. (3.8), and the solid line is from 10-4-3 plus Eq. (3.26).

the other hand, for strongly polar fluids the induction energy always makes a substantial contribution to the total energy. It is difficult to give a rule of thumb for under what situation we need to include the induction terms. However, we may safely conclude that we should not neglect induction for any fluid molecule with a dipole moment bigger than 1 Debye in order to control the q_{st}^0 error less than 10%.

3.4.2 Adsorption isotherms

Many molecule potentials have a variety of different parameterizations, most of which are designed to reproduce liquid phase experimental data. While several different potential models may do an equally good job of describing the bulk pure fluid properties, it is probable that the different fluid-fluid potentials will generate quite different solid-fluid potentials, assuming that one applies the standard Lorentz-Berthelot combining rules to generate the solid-fluid potentials. For example, it was shown that for the propane-graphite system five different propane potential models gave rise to five quantitatively different adsorption isotherms. [89] This emphasizes the importance of the accuracy in calculating the solid-fluid interactions.

We have performed calculations to test the influence of polar interactions on the adsorption isotherms. Two fluids, acetone and hydrogen sulfide, were chosen as typical examples of strong and weak polar fluids, respectively. The dipole moment of acetone is 2.70 Debye, while that of hydrogen sulfide is 0.97 Debye. The details of the potential models for these two fluids can be found in the literature[75, 82]. Since the induction energy is proportional to the square of the adsorbate dipole moment, we expect the effect of induction on adsorption isotherm be quite different for these two fluids. Molecular simulations were carried out in the grand canonical Monte Carlo (GCMC) ensemble. [90] Conventional GCMC works well for hydrogen sulfide adsorption. However, insertion and deletion of molecules is extremely inefficient for simulation of acetone adsorption on graphite. We implemented the orientationally biased GCMC technique [91] to improve the efficiency of the acetone adsorption calculations. Each attempted insertion or deletion of a molecule utilized information from five random orientations. All the GCMC simulations were performed at 150 K. A typical simulation run included 50 million moves for equilibration and an additional 50 million pro-

Table 5: The isosteric heat of adsorption at zero coverage, $q_{\rm st}^0$, for some polar fluids on graphite in kJ/mol.

	μ (D)	Θ (10^{-40}Cm^2)	10-4-3	10-4-3 +polar terms
H_2O	1.85	-	3.32	5.58
NH_3	1.47	-	4.84	6.63
CO_2	-	-12.2	11.50	13.04
Acetone	2.70	-	31.9	36.80
N_2	-	-4.7	4.28	4.28
Cl_2	-	10.79	20.02	20.11
CO	0.112	-8.33	4.58	4.79
H_2S	0.97	-	12.30	13.34
O_2	1.63	-	16.85	20.08
CS_2	-	12.0	26.46	26.71
C_2H_4	-	6.67	13.99	14.35
C_2H_5OH	1.69	-	22.62	23.35
N_2O	-	-11.67	15.02	15.20

duction moves. Displacements, reorientations, insertions, and deletions were attempted with equal probability. The average number of molecules in the simulation box varied from about 90 to 200. The potential cutoff was set to about 10 Å.

Adsorption isotherms for acetone on graphite at 150 K are presented in Fig. 17. The circles are simulation results computed from the non-polar 10-4-3 potential only and the squares include polar interactions through the integrated expressions, Eqs. (3.8)−(3.10). The simulations focused on the 1-2 layering transition region. It can be seen that the addition of polar interactions changed the character of the layering transition pattern from continuous to apparently first-order. However, the location of the transition is not significantly shifted. This observation is consistent with previous observations showing that an increase or decrease in the solid-fluid potential changed the character of the 1-2 layering transition without greatly affecting the pressure at which the transition took place. [89]

The isotherms hydrogen sulfide on graphite at 150 K computed from the non-polar potential and the full potential including polar interactions are plotted in Fig. 18. It can be seen that shape of the isotherm and apparent order of the 1-2 layering transition are insensitive to the inclusion of polar interactions. Thus, polar interactions of H_2S with graphite may be safely ignored in computing accurate adsorption isotherms. In general, isotherms for weakly polar fluids may be computed accurately without including polar terms in the solid-fluid interaction potential, while for strongly polar fluids such as water require inclusion of these terms for high accuracy.

3.5 CONCLUSION

We have derived angle averaged integrated expressions for interactions between a polar adsorbate molecule and a graphite surface. The integrated potentials account for dipole-quadrupole, dipole-induced dipole, and quadrupole-quadrupole interactions. The integrated potential functions depend only on the perpendicular distance between the fluid molecule and the graphite surface. They are simple, easy to implement into computer simulations, and computationally inexpensive. The potential energy calculated from Eqs. (3.8)−(3.10) agrees well with the results from calculations utilizing atomistic potentials. The self-consistent

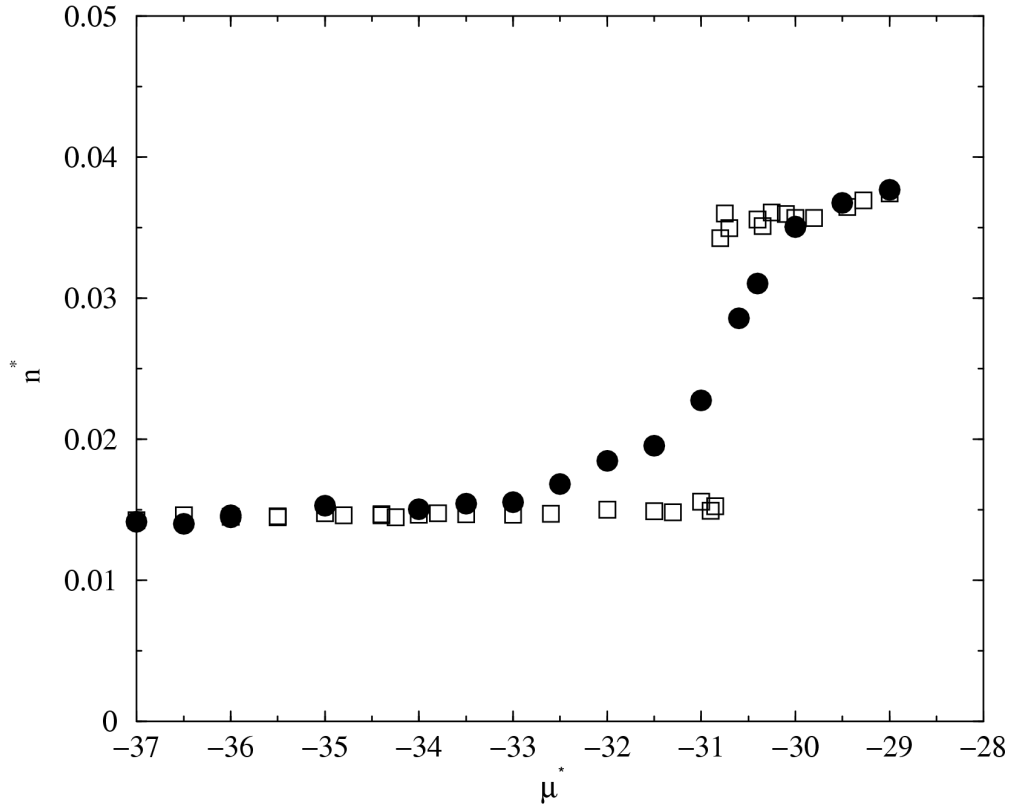

Figure 17: Comparison of adsorption isotherm of acetone on graphite at 150 K. The squares are the simulations using 10-4-3 plus Eq. (3.8), and the circles are the simulations using 10-4-3 only. The chemical potential μ^* and coverage n^* are in reduced unit.

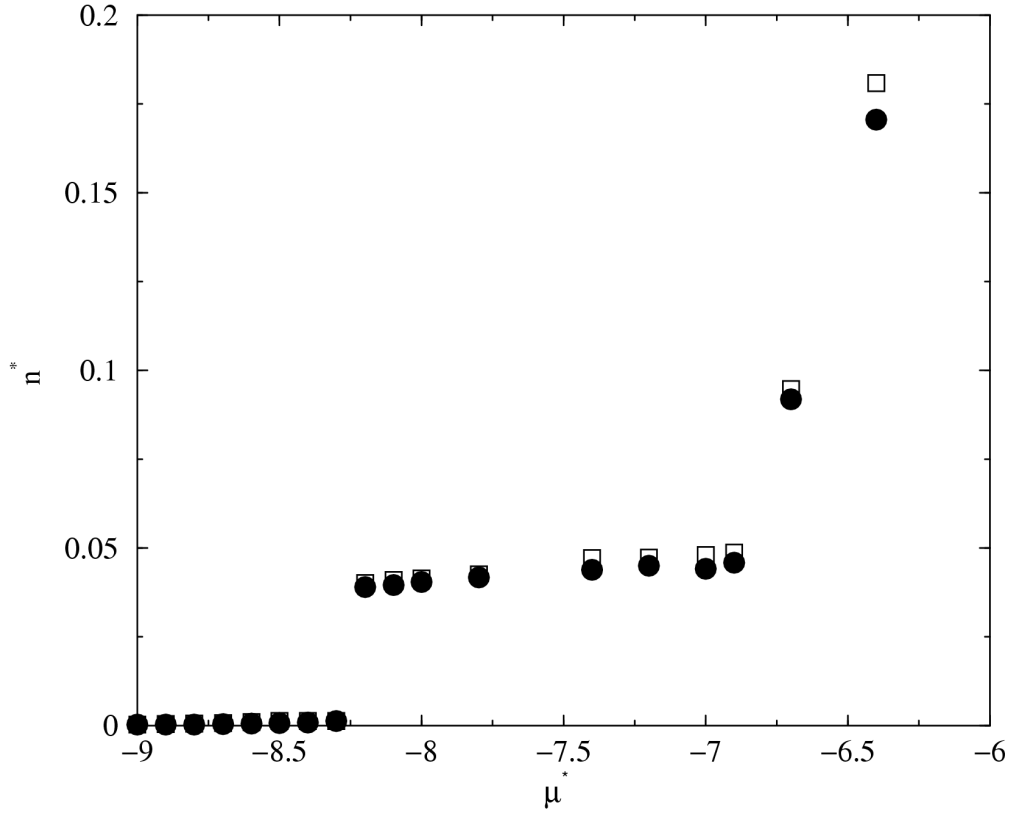

Figure 18: Comparison of adsorption isotherm of hydrogen sulfide on graphite at 150 K. The squares are the simulations using 10-4-3 plus Eq. (3.8), and the circles are the simulations using 10-4-3 only. The chemical potential μ^* and coverage n^* are in reduced unit.

polarization was neglected in Eq. (3.8). Calculations on several polar fluids were used to test the derived formulas. It was found that for weakly polar fluids, like hydrogen sulfide, the solid-fluid polar terms are negligible compared with the LJ interactions. For strongly polar fluids, such as water and acetone, the contribution from the polar terms to the total potential energy is significant and must be included for accurate calculations.

The derived formulas were used in calculation of the zero coverage isosteric heat of adsorption for several different polar fluids on graphite and compared with the values computed from the non-polar potential only. For strong polar fluids the electrostatic and induction interactions increase the heat of adsorption substantially. GCMC simulations were performed to test the influence of polar interactions on adsorption isotherms. Addition of polar interactions to solid-fluid potential can change the character of 1-2 layering transition for strongly polar fluids adsorbing on graphite.

4.0 STUDY OF ACETONE ADSORBED ON GRAPHITE

4.1 INTRODUCTION

We have performed NVT and GCMC simulations of acetone adsorption on graphite in order to investigate the layering transitions, geometry, and coverage of acetone in the first, second and third layer. It was found from experiments that the 1-2, 2-3 layering transitions of acetone on graphite at 91 K follow a Volmer-Weber pattern rather than a layer by layer pattern. [92] That is, the second layer of acetone molecules start to grow on the graphite surface before the first layer is filled, and the third layer begins before the second layer is filled. Molecular simulation is used to probe the mechanism behind this phenomena.

4.2 POTENTIALS AND SIMULATION METHODS

The interaction between acetone-acetone molecules was modeled as a nonpolarizable potential.[75] The model consists of four Lennard-Jones sites to account for the CH_3, C, and O groups, plus explicit charges centered on each of the Lennard-Jones sites to account for the polar interactions. The Lennard-Jones and charge parameters are given in Table 6. The molecule was held rigid with CH_3-C bond lengths of 1.572 Å, a C=O bond length of 1.223 Å, a CH_3-C=O bond angle of 121.35°.

The reaction field correction was applied to account for the long-range electrostatic interactions. The cutoff for the Lennard-Jones interactions was taken to be about 15 Å. The acetone-graphite interaction was computed from the 10-4-3 potential developed by Steele [57], as shown in Eq. (3.4), plus induction and quadrupole interactions to account for the

Table 6: Parameters for the acetone model used in the simulations[a].

	CH_3	C	O
$\sigma(\AA)$	3.88	3.75	2.96
$\epsilon/k(K)$	85	52.84	105.68
$q(e)$	-0.032	+0.566	-0.502

[a] The Lennard-Jones parameters are the diameter σ and well depth ϵ/k, where k is the Boltzmann constant. The charges are placed at the center of each Lennard-Jones site.

charge sites on acetone interacting with the graphite surface, shown in Eq. (3.8) and (3.10). The 10-4-3 potential parameters were computed from the Lorentz-Berthelot combing rules, Eq. (2.2) and (2.3).

Canonical ensemble (NVT) Monte Carlo simulations were performed to generate equilibrium configurations of adsorbed acetone at fixed coverage. The simulation cell consisted of one surface representing the basal plane of graphite with a repulsive (reflecting) wall fixed opposite the graphite plane. The distance between the graphite plane and the reflecting wall was 59 Å. Periodic boundary conditions were applied in the remaining two directions. One or more layers of acetone molecules were placed in close proximity to the graphite surface in order to generate the initial configuration. Different coverages were simulated by varying the number of layers of acetone in the box. The system was equilibrated for 2 milion moves, each move consisted of either a random displacement of a random reorientation of an acetone molecule. The maximum displacement and reorientation parameters were adjusted during equilibration to achieve approximately a 50% acceptance rate for each type of move. Data taking for an additional 2 million moves followed equilibration. A few very long NVT simulations were performed to check the long-time stability of the structures. These longer simulations consisted of up to 150 million moves.

Molecular simulations of acetone adsorption were also carried out in the grand canonical Monte Carlo ensemble wherein the chemical potential, volume, and temperature of the system are held fixed and the number of molecules adsorbed on the surface is changed through randomly inserting and deleting molecules in the simulation cell. Because of the size and

polarity of the acetone molecule, conventional GCMC simulations are extremely inefficient for inserting and deleting molecules, We have implemented orientationally biased GCMC[91] to improve the efficiency of the calculations. Each attempted insertion or deletion of a molecule utilized information from five random orientations. The GCMC simulations were carried out at 90 and 150 K. Simulation were equilibrated for 50 million moves, consisting of displacements, reorientations, insertions, and deletions, attempted with equal probability. Data were collected over an additional 50 million GCMC moves. The average number of acetone molecules in the simulation box varied between 110 and 280. The potential cutoff for the GCMC simulations was set to about 10 Å.

4.3 LAYERING TRANSITIONS

Experimental work performed by our collaborators shows that the layering transition of acetone adsorbed on graphite was a Volmer-Weber mechanism[93] at 91 K. That is, the bilayer coverage begins to grow before the first layer is fully covered, and third layer begins to grow before the monolayer and bilayer reach their saturation coverage. The mechanism is illustrated in Fig. 19. The experimental data indicate that the monolayer is about one-thirds of its saturation coverage when the bilayer begins to grow, and when the multilayer appears the monolayer is about 90% complete and the bilayer is about 75% complete.

Fig. 20 is a plot of adsorption coverage, calculated by the NVT simulations, in each layer as a function of the total coverage. The second layer begins to grow at a total coverage of about 4.5×10^{-6} mol/m^2, at which point the monolayer is about 75% full. This is in reasonable quantitative agreement with the estimate from the experiment findings. The simulation data in Fig. 20 confirm that the third layer begins to grow before the second is filled, which also agrees with the experimental data.

Additional simulations in the NVT ensemble were run for very long times at a coverage that would correspond to monolayer completion. The simulations indicate that the Volmer-Weber growth model is apparently a kinetic phenomenon rather than the equilibrium configuration. The simulation show that molecules from the second layer slowly relax to the first layer over the course of the run. However, even after 150 million moves not all

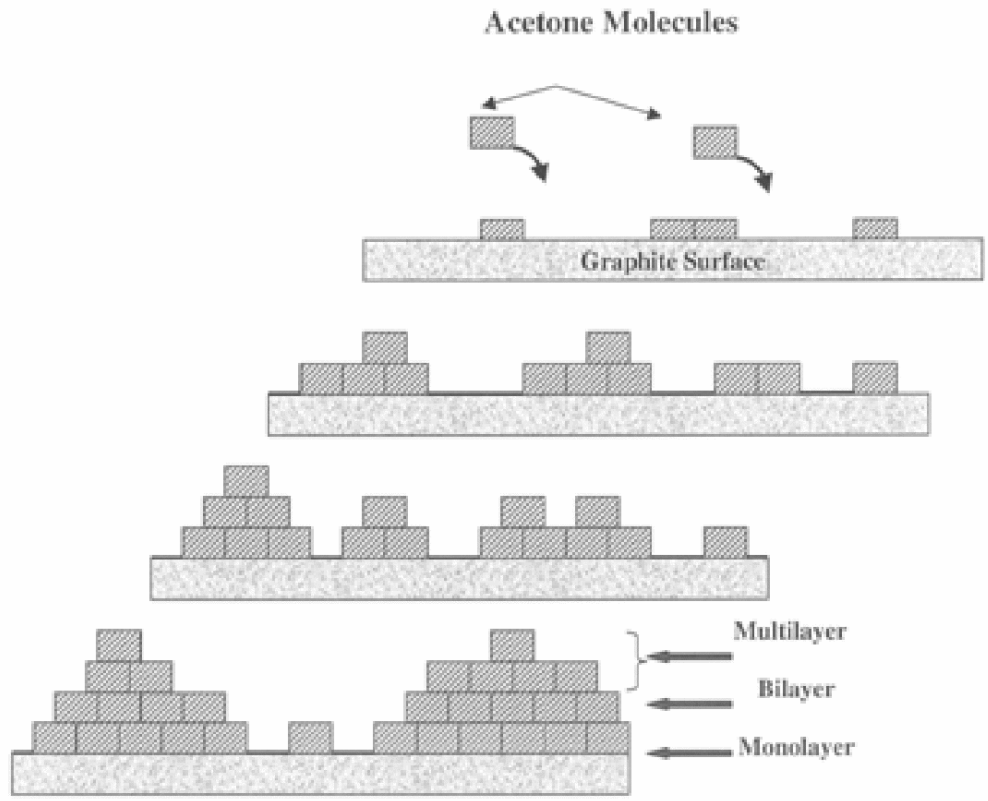

Figure 19: Schematic drawing of the proposed topological growth mode (Volmer-Weber) of acetone on graphite at 91 K. The bilayer appears before the monolayer state is completely saturated. As the bilayer feature grows, the monolayer feature continues to increase, though more slowly. The multilayer also appears before monolayer or bilayer saturation has been achieved.

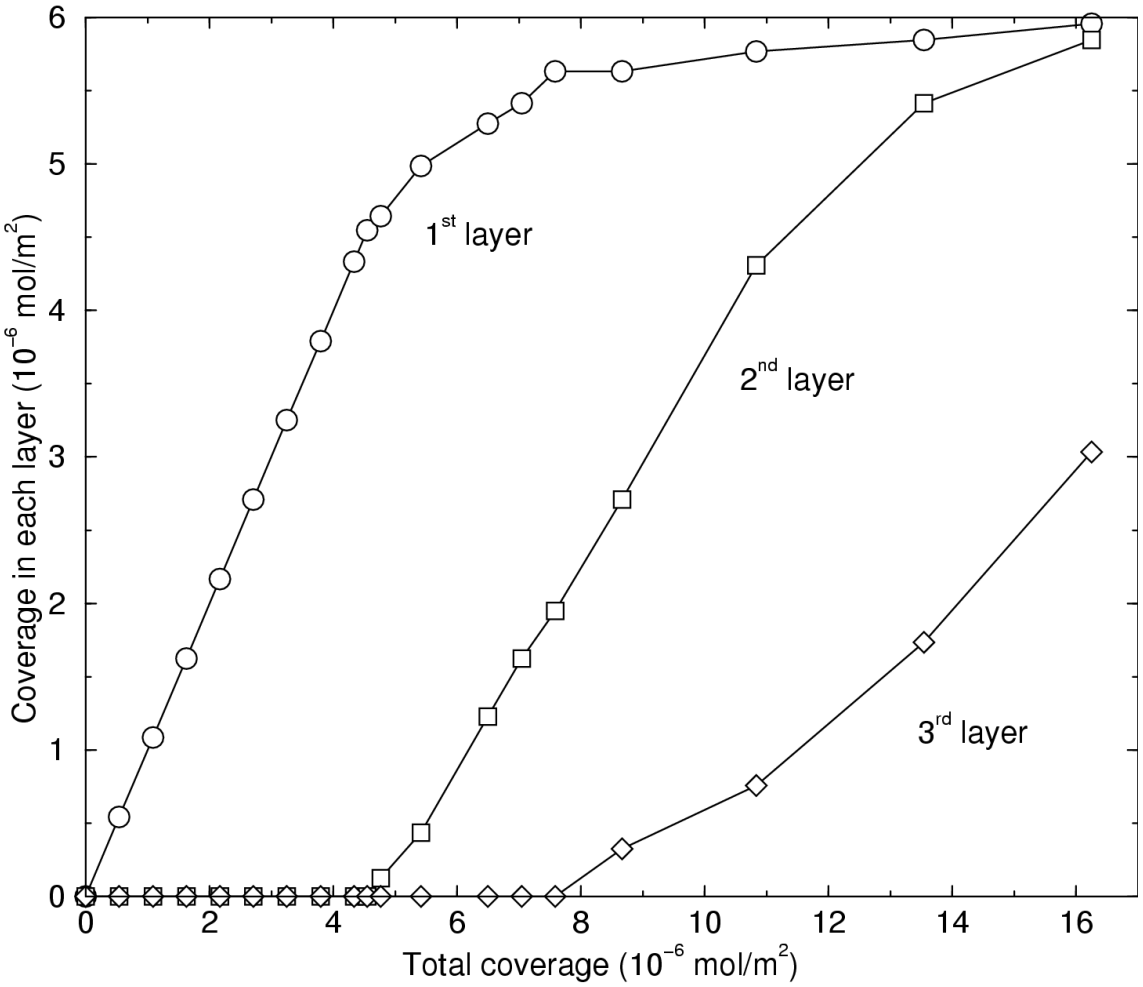

Figure 20: The growth pattern of acetone on graphite from NVT simulations. at 91 K. The bilayer appears before the monolayer state is completely saturated. As the bilayer feature grows, the monolayer feature continues to increase. The multilayer also appears before monolayer or bilayer is full.

molecules in the second layer were able to diffuse to the first layer. The NVT simulations are more closely related to the experimental situation because molecules strike the surface very rapidly and then slowly relax. Simulations in the GCMC ensemble put molecules on the surface one by one with relaxation of the adsorbate molecules taking place as new molecules are added to the system. Our GCMC simulations show that when acetone is added slowly to the surface, a complete monolayer is formed before adsorption in the second layer starts. Thus, the equilibrium situation is for layer by layer growth rather than Volmer-Weber.

4.4 STRUCTURES

The molecular simulations show that the average angle between the dipole moment of the acetone molecules in the first layer and the graphite surface normal is about 80°. Likewise, the angles between the molecular and graphite planes for molecules in the first layer is about 10°. The molecules are pointed slightly down, with the oxygen atoms pointing toward the graphite plane. This orientation can be observed in the snapshot from the simulations shown in Fig. 21. It can be seen from this figure that the dipoles tend to align into local domains such that the dipole-dipole energy is minimized.

4.5 CONCLUSION

We have performed molecular simulation of adsorption of acetone on graphite surface in GCMC and NVT ensembles. The simulation results support the experimentally observed layering transition pattern of acetone/graphite systems at 91 K. The growth of monolayer and multilayers follow Volmer-Weber mechanism rather than layer by layer mechanism. Molecular simulations show that acetone adsorbs nearly parallel to the graphite surface in the first layer, but some molecules begin to orient perpendicular to the surface as the second layer forms. We observed in molecular simulation that the monolayer acetone molecules tend to order into local domains according to their dipole directions. For multilayer molecules, we did not observe the similar phenomena but random packing.

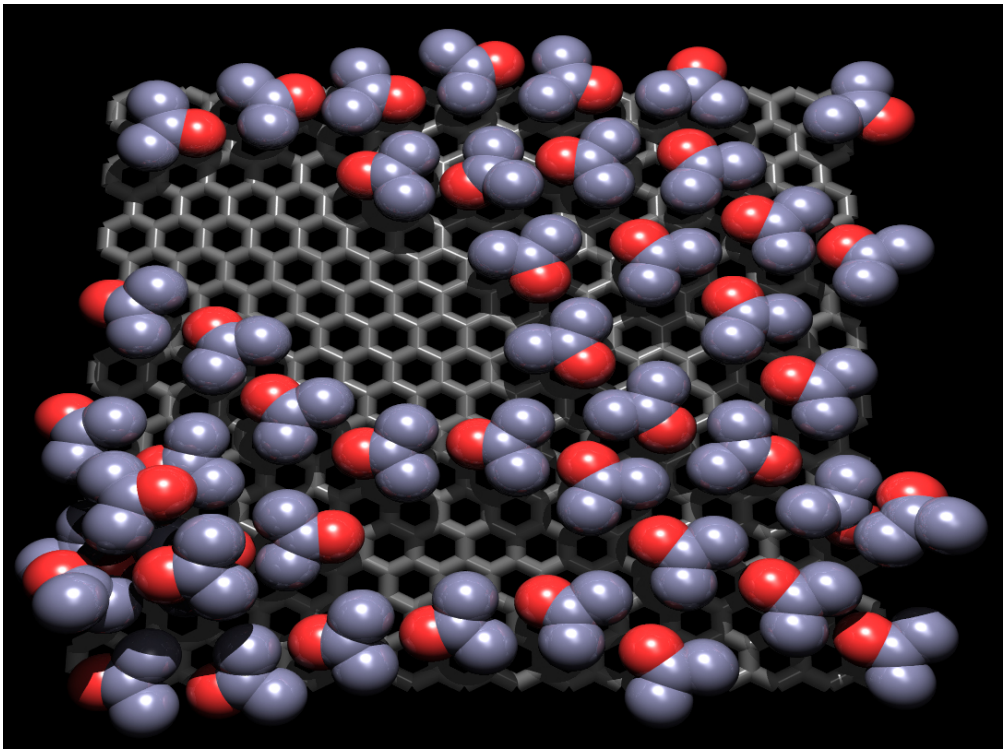

Figure 21: A snapshot of acetone molecules on graphite surface. Note that the dipoles tend to order into local domains so that the dipole-dipole interaction is favorable. The graphite surface in not completely covered at this coverage, revealing an incomplete first layer. Molecules adsorbed in the second layer are apparent in the lower left-hand corner for example.

5.0 SIMULATION OF CO ON SILVER

5.1 INTRODUCTION

Since the early days of the development of surface science, it is believed that chemisorbed first layer on planar crystalline surfaces involves the formation of relatively strong chemical bonds with the surface, which helps producing translationally ordered and azimuthally-oriented molecules.[94, 95] The second layer is generally described as a more weakly-bound layer held mainly by van der Waals forces and usually envisioned as being liquid like. However, recent experimental work by Lee *et al.*[96] found that in contrast to the postulate of a liquid-like second physisorbed layer, CO adsorbed on Ag(110) can involve molecules which possess a distinct azimuthal registry in the second layer with the underlying localized chemisorbed monolayer and the single crystal substrate. Their investigation by electron stimulated desorption ion angular distribution (ESDIAD) method [97] shows that first layer chemisorbed CO molecules on bare Ag(110) tilt away from the surface normal in azimuthal directions parallel to the $\langle 001 \rangle$ azimuth of the crystal, with C-O bond tilt angle from the normal being 26 °. Surprisingly, they found the second layer CO molecules are also ordered, with azimuthal angles of about 45° to the principal azimuthal axes of the metal surface. This indicates that the second layer of CO recognizes the structure of the underlying first layer of chemisorbed CO and the crystal substrate by adopting specific C-O bond directions which relate in a new geometrical manner to the principal azimuths of the surface. The C-O bonds in the second layer are inclined by a angle of about 43^o to the normal.

In order to verify this new finding, we performed computer simulations to study the physical adsorption of CO on top of the chemisorbed CO molecules and Ag(110) metal surface.

Table 7: Parameters for the CO model used in the simulations.

	σ(Å)	ϵ/k(K)	$q(e)$	l(Å)
C	3.385	29.89	0.831	-0.6446
O	2.885	61.57	0	0.4836
site 1	-	-	-0.636	-1.0820
site 2	-	-	-0.195	0.3256

l is the distance from the molecular center of mass.

5.2 POTENTIAL MODELS

The potential model[98] used for calculating the interaction between any pair of CO molecules include two parts. The first part is the Lennard-Jones interaction centered on C and O atoms. The second part of the potential is the electrostatic part, which is represented by three explicit charge sites on the molecular axis, with one of the charge sites located on the carbon atom. The potential parameters are shown in Table 7.

Because the interest in this part is to study the structures of CO adsorbed on silver surface at the temperature range of 30 K (experiments were performed around 30 K), we carried out NVT ensemble simulations of pure CO fluid to test the accuracy of the potential at this temperature range. We have used simulated annealing approach to freeze the fluid to solid state and look at the crystal structure of the solid CO. The simulation were performed at 80, 70, 65, 60 and 55 K consecutively, in each simulation the final configuration from the previous higher temperature simulation was taken as the starting lattice. At 55 K the CO fluid was frozen into solid crystal and the structure was compared with the experimental data. Fig. 22 shows a side-view of the solid state structure of CO we obtained from NVT simulations. It shows the lattice composed by the center of mass of CO. It is clear that simulations successfully reproduced the α-FCC lattice, which agrees with experimental measurement [99]. Thus we established that the chosen CO potential works fine with calculating the structure of CO at low temperatures.

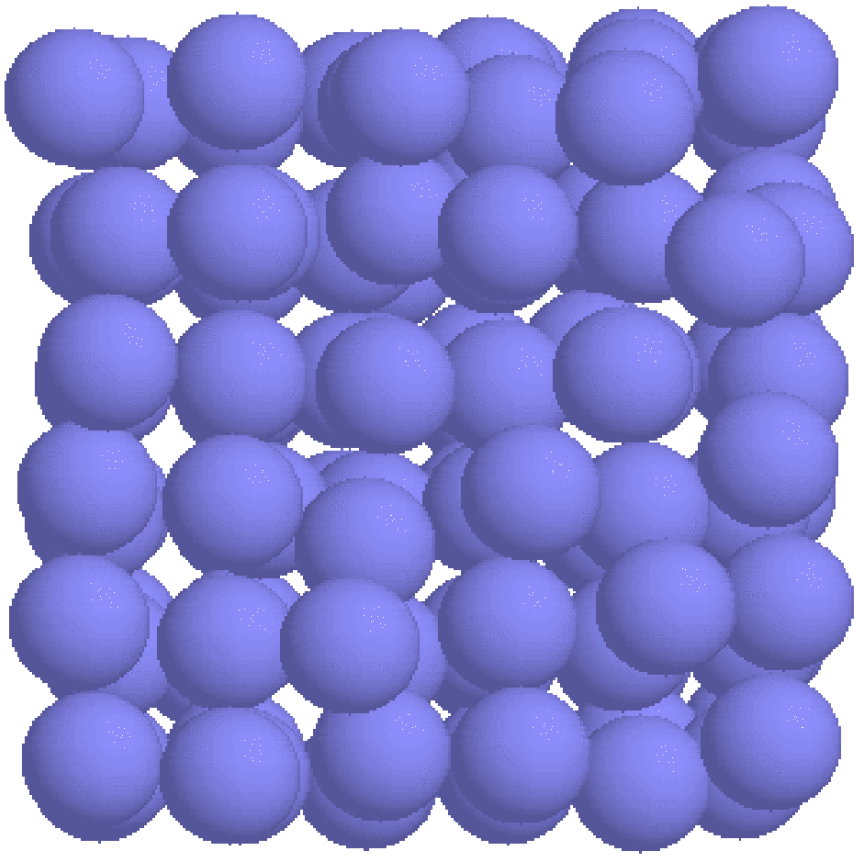

Figure 22: The simulated FCC lattice of CO. This figure shows the lattice composed of center of mass of CO molecules.

The interaction of Ag-C and Ag-O also includes Lennard-Jones part and electrostatic part. The Lennard-Jones parameters for Ag atom are $\sigma = 3.654$ Å and $\epsilon/k = 66.36$ K. [100] The cross interactions were computed from Lorentz-Berthelot combining rules for the Lennard-Jones parameters.

The Ag(110) surface used in the simulation consists of four unit cells in the z direction, 8 unit cells in the x, or $\langle 1\bar{1}0 \rangle$ direction, and 12 unit cells in the y, or $\langle 001 \rangle$ direction. Periodic boundary conditions were applied in the x and y directions. A repulsive potential was applied opposite to the adsorbing Ag(110) surface at a distance of 74.5 Å above the top Ag layer to keep the gas phase CO molecules in the simulation cell. The Ag atoms in the outer layer are given a slight positive charge of $+0.2e$. The second layer Ag atoms are given a charge of $-0.2e$. This charging scheme is qualitatively consistent with the Smoluchowski effect for a corrugated metal surface [101, 102, 103]. Chemisorbed CO molecules were placed on the Ag(110) surface in the experimentally observed 2×1 periodicity. The CO bond directions tilting at about 26° from the surface normal along the $\langle 001 \rangle$ azimuth with CO molecules tilted in opposite directions in each of the row as one moves along the close packed $\langle 110 \rangle$ azimuthal direction. Fig. 23 is a schematic graph for the layout of monolayer CO and Ag substrate underlying it used in our simulations. We assumed that the chemisorbed CO molecules maintained the same geometry as gas phase CO. A potential cutoff of 15.3 was applied to all Lennard-Jones interactions and no long-range corrections were applied. The electrostatic interactions were computed with the same cut off, but the reaction field method was used to account for the long-range corrections.

5.3 STRUCTURES OF SECOND LAYER CO ON AG

We performed grand canonical Monte Carlo (GCMC) simulations at various CO gas pressures in order to generate coverages comparable with those observed in the experiments. In GCMC simulations the systems were equilibrated for 20 million moves, where a move consists of either translation, reorientation, creation, or deletion, chosen randomly with equal probability. NVT simulations following GCMC equilibration with an additional 10 million moves, consisting of translations and rotations, were performed to efficiently sample angle

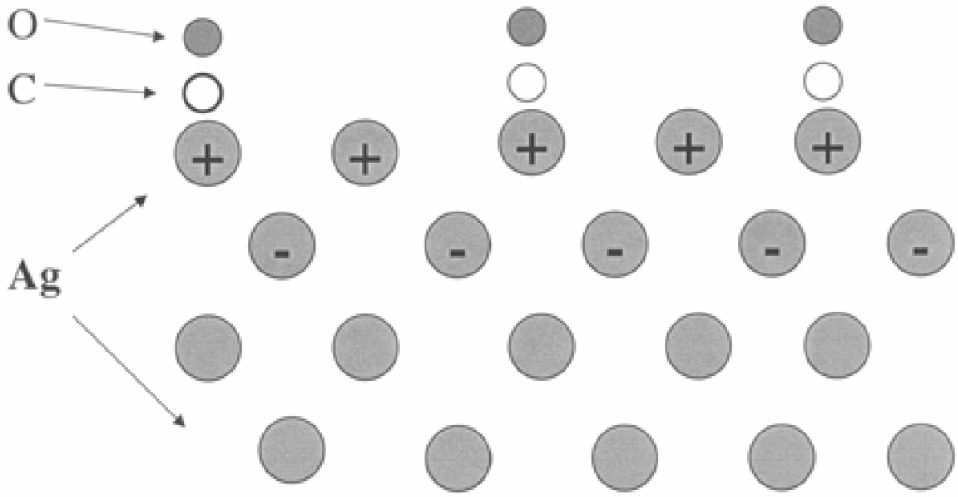

Figure 23: The schematic figure for the substrate used in our simulations. The substrate includes four layer of Ag(110) atoms and monolayer of chemisorbed CO. C atoms of chemisorbed CO are bonded with Ag atoms on the surface. C-O bonds bend into the paper by 26°, which is not shown in the figure.

Table 8: Shifted charge distribution for the chemisorbed CO potential.

Units of electron charge	Distance from center of mass ($\mathring{A}$)
-0.826	-1.0820
$+0.831$	-0.6446
-0.005	$+0.3256$

and position distribution. The histograms of the orientations of the second layer physisorbed CO molecules were collected. The Ag atoms and chemisorbed CO molecules were held fixed throughout the simulation. A representative snapshot from a simulation at 25 K and ultra high vacuum pressure is shown in Fig. 24. We can observe from the snapshot that virtually all the second layer CO molecules adsorb with the oxygen atoms pointing away from the surface and most molecules are tilted at one of four different azimuthal angles to the principal crystal axes of the $\langle 1\bar{1}0\rangle$ surface. Fig. 25 gives the probability distributions of the CO bond angles at the same conditions as in Fig. 24. The solid line is the probability density of observing CO molecules with various azimuthal angles with respect to the $\langle 1\bar{1}0\rangle$ direction. It can be seen that there are peaks in the azimuthal angle probability at about 30°, 150°, 210° and 330°. The dashed curve is the probability density of observing the C-O bond at a given angle with respect to the Ag(110) surface normal. It can be seen that the most probable C-O bond angle is at about 53°. Both angle distributions are in qualitative but not quantitative agreement with the ESDIAD experiments.

One possible fact that may affect the orientation of second layer CO adsorbed on silver metal is the redistribution of charges on the chemisorbed CO in the monolayer. To explore that situation, we modified the potential model for the chemisorbed CO by redistributing the charges. A charge amount of $0.19e$ was added to and subtracted from the charge site closest to and farthest from the O site, respectively. The modified potential for the chemisorbed CO is shown in Table 8. Thus, the total positive charge on the chemisorbed CO is unchanged but the dipole moment of it is increased. We performed similar simulation for comparison.

Fig. 26 and Fig. 27 shows the snapshot and the probability of orientational distribution curves from this approach. The dark spheres (partially bonded to the other atom) stand for

O atoms in the second layer CO molecules, grey spheres are the O atoms in the chemisorbed CO molecules, the light spheres are C atoms, and the grey sphere in the bottom (most of them are covered by CO molecules) are Ag atoms. We can see that all the second layer CO are ordered with O atom pointing up from the substrate, which agrees with the experiment observation. It can be seen in Fig. 27 that azimuthal angles are peaked at 45°, 135°, 225°, and 315° with respect to $\langle 1\bar{1}0 \rangle$, in excellent agreement with experiment results. The agreement with experiment is remarkable given the simplicity of the model. The dashed curve is the probability density of observing the second layer CO bond at a given angle with respect to the Ag(110) surface normal. It can be seen that the most probable CO bond angle is at about 50°, in reasonable agreement with the experimentally measured angle of 43°.

From the simulation we also learned that the azimuthal ordering of CO in the second layer can be directly attributed to the charges on the Ag atoms in the first and second layer in the model. If we remove the charges from the Ag atoms then no azimuthal ordering is observed, even with the chemisorbed CO molecules in place. On the other hand, the orientation and charge redistribution on the chemisorbed CO molecules are also crucial for generating the correct angular distribution.

Therefore, molecular simulation verified the rare observation from experiment that a physisorbed second layer can exhibit unique azimuthal orientations as a result of weak interactions with an underlying ordered chemisorbed layer bound to a single crystal substrate. The observation of ordered molecular registry for weakly-adsorbed second-layer of physisorbed molecules indicates that the common assumption of a liquid-like character for these layers is not a valid generalization.

5.4 CONCLUSION

We have carried out molecular simulations to investigate the mechanism governing the rare experimental observation of physisorbed second layer CO ordering on Ag surface. We have used two different models for CO molecules and compared the structures generated with the experiments. The simulations results indicate that the azimuthal ordering of CO can be directly attributed to (1) the charges on the Ag atoms in the first and second layer; (2) the

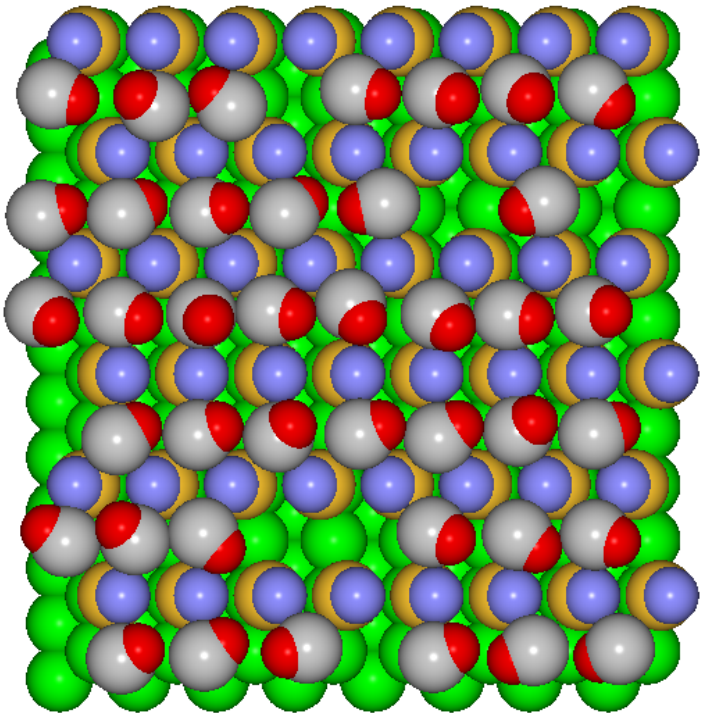

Figure 24: The snapshot from simulation of second layer CO adsorbed on Ag and monolayer CO. The Ag atoms forms a $\langle 1\bar{1}0 \rangle$ 4×1 substrate, chemisorbed CO are bonded to the Ag atoms on the surface. Positive and negative charges are placed on the Ag atoms in the top and second layers. Both bulk CO and chemisorbed CO are treated equally with the same potential model.

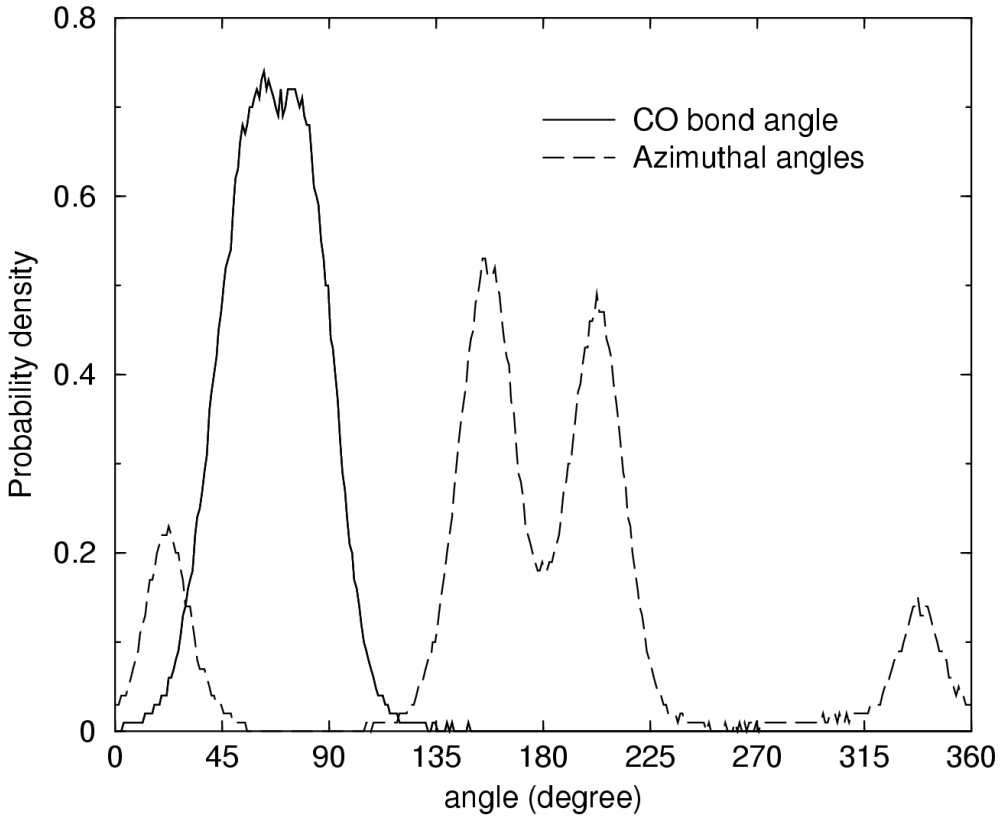

Figure 25: The distribution of orientations of the second layer CO molecules corresponding to the snapshot in Fig. 24. This figure shows the distributions of both dipolar angles and azimuthal angles of second layer CO.

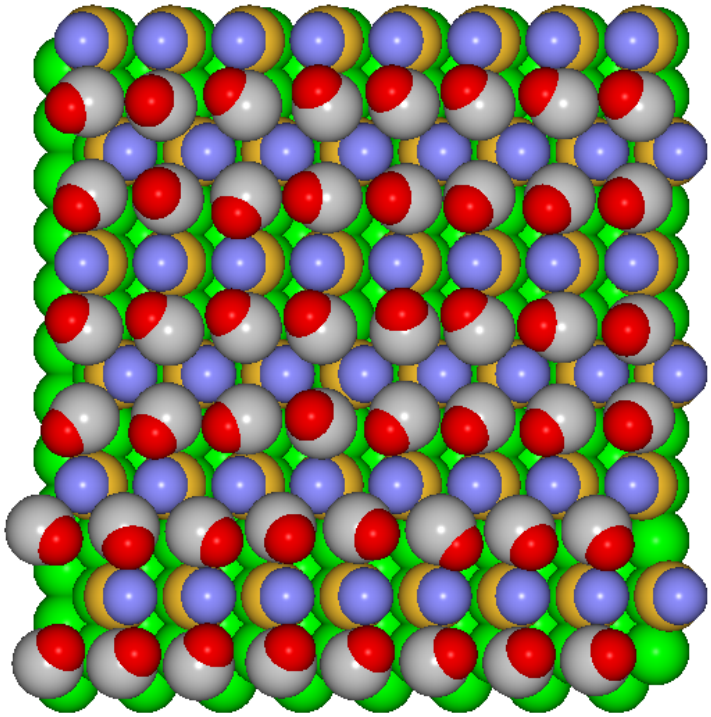

Figure 26: The snapshot from simulation of second layer CO adsorbed on Ag and monolayer CO. All the simulation conditions are the same as that shown in Fig.24 except that bulk CO molecules are modeled by the potential model shown in Table 7, while chemisorbed CO molecules are treated slightly different, with charge distribution shown in Table 8 .

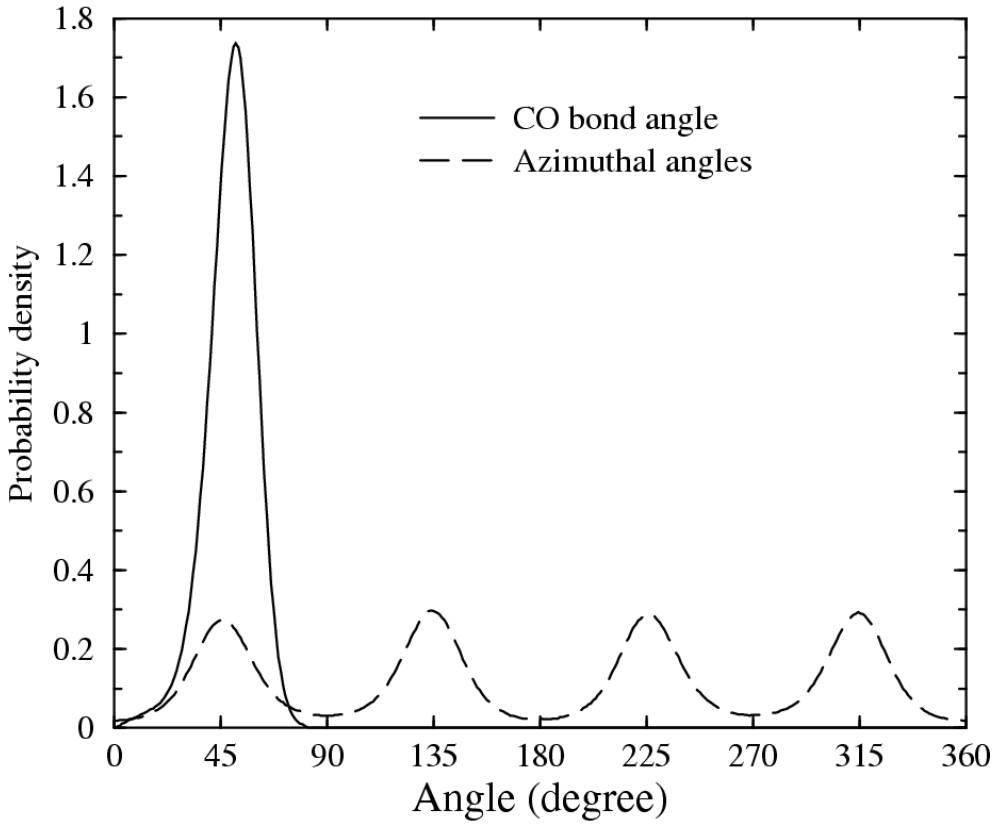

Figure 27: The distribution of orientations of the second layer CO molecules corresponding to the snapshot in Fig. 26.

orientation of the chemisorbed CO molecules; (3) charge redistribution on the chemisorbed CO. The very good agreement between the simulation and experiments shows that a weakly bound physisorbed second layer can exhibit unique azimuthal orientation ordering and the common assumption of a liquid like character for these layers is not a valid generalization.

6.0 SIMULATION OF QUANTUM FLUID INTERFACES

6.1 INTRODUCTION

Surface tension is a key fluid property in applications such as coatings, adhesives, and surfactants. Surface tension is also of fundamental importance in wetting phenomena, prewetting transitions, hydrophobic effects, and probing interactions between solids and fluids. Theoretical and empirical methods have been used to calculate surface tension since the 1920s. [104, 105, 106, 73, 107, 108, 109, 110, 111, 112]. Some of the more modern methods are able to predict the surface tension of classical fluids with an error of less than 5% compared to experimental data.[108] Similar methods have been suggested for quantum fluids, [73, 113, 114, 115] but they are either dependent on the parameters fitted from experimental data or not capable of quantitatively predicting the surface tension of quantum fluids. For example, Sinha and coworkers pointed out that the method developed by Hirshfelder *et al.* based on the de Boer parameter predicts that the surface tension of both classical and quantum liquids have the same temperature dependence, but that this is contradicted by experimental observations.[114] The methods proposed by Frisch and Nielaba[115] and by Hooper and Nordholm[113] do not give quantitative agreement with experiments for some important quantum fluids such as He and H_2. The method for computing surface tension given by Sinha *et al.* does work quite well for hydrogen isotopes.[114] However, this method is not strictly predictive because it relies on parameter fitting to experimental data.[114]

Molecular simulations have been used since 1974 to compute vapor liquid surface tension.[116, 117] All previous surface tension simulations have involved classical fluids. [116, 117, 118, 119, 120, 121, 122, 123, 124, 125, 126, 127, 128, 129, 130, 131, 132, 133, 134] In this paper we report the first molecular simulations of the surface tension of quantum fluids. We

compute the interfacial properties of hydrogen, deuterium, and their mixtures. Orthobaric densities and surface tension for pure H_2 and D_2 are computed over a range of temperatures and compared with experimental data. Mixture vapor-liquid equilibrium (VLE) and surface tension data were computed for the H_2/D_2 mixture over the entire composition range at 24 K. We assess the importance of quantum effects on the surface tension, phase diagram, and interfacial segregation by comparing quantum and classical simulations.

6.2 METHODOLOGY

6.2.1 Surface tension from path integral hybrid Monte Carlo

We have combined the path integral formalism of Feynman [135] with the standard slab method for computing the interfacial properties of a liquid in equilibrium with its own vapor. We started each simulation by generating a lattice at a liquid-like density in a cubic simulation cell. The lattice was melted by equilibrating the homogeneous liquid, after which empty cells of same size as the liquid cell were added to each side of the liquid slab in the z-direction. The system was then equilibrated to generate stable interfaces and liquid and vapor phases. The VLE densities were computed from the average densities of the fluids near the centers of the vapor and liquid boxes. The surface tension was calculated during the simulation by means of the virial expression[127]

$$\gamma = \frac{1}{2A} \left\langle \sum_{i<j}^{N} \left(r_{ij} - \frac{3z_{ij}^2}{r_{ij}} \right) \frac{du(r_{ij})}{dr_{ij}} \right\rangle, \tag{6.1}$$

where $A = 2xy$ is the total surface area, $u(r_{ij})$ is the potential energy between molecules i and j, and r_{ij} is the distance between molecules i and j. The angle brackets denote a time average. The summation extends over all pairs of molecules within the cutoff radius r_c.

Systems containing thousands of molecules are required to obtain stable coexisting phases and large enough values of the potential cutoff. Long equilibration times are required to fully develop the interfacial and bulk regions. This makes accurate simulations of the interfacial properties of fluids a computationally demanding task. Calculation of interfacial properties of quantum fluids is even more challenging. Feynman established an isomorphism between a

quantum particle and a classical ring polymer containing a number of beads, P, connected by harmonic springs. [135] The average manybody properties of a system of quantum molecules can be computed from the correct statistical mechanical averages of the system of ring polymers. This isomorphism is exact in the limit as $P \to \infty$. In practice, the thermodynamic properties converge rapidly with P for hydrogen isotopes in the liquid phase. The value of P required to converge the properties depends on the isotope mass, the temperature, and the density. We have found that 10 to 20 beads gives sufficient accuracy for the conditions considered in this work. Thus, a simulation of 1000 H_2 molecules will contain as many as 20000 beads. The virial expression for the path integral fluid is analogous to Eq. (6.1) and is given by

$$\gamma = \frac{1}{2AP} \left\langle \sum_{i<j}^{N} \sum_{\alpha=1}^{P} \left(r_{ij}^{\alpha} - \frac{3z_{ij}^{\alpha 2}}{r_{ij}^{\alpha}} \right) \frac{du(r_{ij}^{\alpha})}{dr_{ij}^{\alpha}} \right\rangle, \tag{6.2}$$

where r_{ij}^{α} is the distance between bead α on molecule i and bead α on molecule j.

The intra-bead harmonic potential in the path integral formalism is typically very stiff. This leads to time scale coupling problems. We have therefore implemented multiple time scale hybrid Monte Carlo to decouple the stiff intramolecular motion and the weaker intermolecular forces. This path integral hybrid Monte Carlo (PIHMC) technique was developed by Tuckerman et al. [136] We have previously used the PIHMC technique to simulate fluid hydrogen over a wide range of temperatures and pressures. [137, 138]

6.2.2 Long range corrections

It is known that both a long potential cutoff and accurate long-range corrections are required to obtain converged values of the surface tension. The surface tension is much more sensitive to the details of the potential cutoff and long range correction than other properties such as orthobaric densities and saturation pressures. Several methods have been proposed for computing tail corrections to the surface tension.[139, 118, 121, 140, 131, 132] In this work we used the method of Mecke and coworkers for both pure fluids [131] and mixtures. [132] The long range correction to the surface tension is calculated by

$$\gamma_{\text{lrc}} = \frac{1}{2A} \left\langle \sum_{\substack{i=1 \\ r>r_c}}^{N} \gamma_i^{\text{lrc}} \right\rangle, \tag{6.3}$$

where the angle bracket refers to the time average of the summation of γ_i^{lrc} and γ_i^{lrc} is the individual tail contribution from each molecule i at each time step during the simulation. γ_i^{lrc} is given by

$$\gamma_i^{\text{lrc}} = \frac{1}{2}\int_{r_c}^{\infty} dr \int_0^{\pi} d\theta \int_0^{2\pi} d\phi \left(r - \frac{3z^2}{r}\right) \rho(r) r^2 \sin\theta u'(r), \tag{6.4}$$

where the prime denotes differentiation, and $\rho(r)$ is the inhomogeneous number density at r. Equation (6.4) can be simplified by integrating over ϕ because the system is inhomogeneous only in the z-direction. This gives

$$\gamma_i^{\text{lrc}}(z_i) = \pi \int_{r_c}^{\infty} \int_0^{\pi} \rho(z_i + r\cos\theta) \sin\theta (1 - 3\cos^2\theta) r^3 u'(r) d\theta dr. \tag{6.5}$$

Equation (6.5) can be extended to mixtures, such as a binary system composed of molecules of type a and b. For this case, the long range correction for molecule i of type a is

$$\gamma_{i(a)}^{\text{lrc}}(z_i) = \pi \int_{r_c}^{\infty} \int_0^{\pi} \sin\theta (1 - 3\cos^2\theta) r^3 \sum_{k=a,b} \rho_k(z_i + r\cos\theta) u'_{a,k}(r) d\theta dr. \tag{6.6}$$

Strictly speaking, numerical integration of Eqs. (6.5) or (6.6) should be performed at every time step for each particle i in order to calculate the instantaneous γ_i^{lrc} because density profiles ρ vary with time. However, this procedure is computationally prohibitive. We can use the fact that γ_i^{lrc} only depends on the position of particle i in the z-direction to improve the efficiency of the tail correction calculations. We divide the simulation box into slabs of thickness δz, with the slabs oriented perpendicular to the z-axis. We precompute the value of $\gamma^{\text{lrc}}(z_k)$, where z_k indicates position of the center of the k^{th} slab. The values are stored in an array after the system is equilibrated. During the production run, the long range correction for the surface tension for molecule i can be read from the array according to the particle's z coordinate. The array of $\gamma^{\text{lrc}}(z_k)$ values can be updated every several hundred time steps during the production run, since the density profile does not change significantly once the system is equilibrated.

Table 9: CPU timings for the parallel simulation of H_2 liquid at 25 K. The system contains 1024 ring molecules, each molecule having 10 beads. The timing is for 1000 hybrid Monte Carlo moves on the Cray T3E clusters.

# of CPU used	Timing per CPU	Total timing
2	213 min	426 min
4	107 min	428 min
32	14 min	448 min

6.2.3 Parallel techniques

Serial simulation techniques are inadequate for computing the surface tension of quantum fluids because of the large number of molecules and beads needed to accurately compute surface tension. We have developed a parallel PIHMC simulation code in order to facilitate the calculation of accurate surface tension values in an acceptable amount of real time. Currently available parallel MD techniques enable large-scale simulations of millions of atoms.[141] The most common parallel MD algorithms include replicated data, force decomposition, and domain decomposition. [142] We have adopted the replicated data algorithm in this work because of its simplicity compared with the other two algorithms. In the replicated data algorithm each processor is assigned a subset of the particles, regardless of where they are located in the physical domain. The forces computed at each time step on each processor are communicated to other processors. The total forces acting on each particle are then summed and the positions and velocities of the particles are updated on each processor. Finally, the updated positions are communicated to all processors for the calculation of potentials and forces in the next time step. The disadvantage of the replicated data technique is that it requires more message passing than many other algorithms, making it inefficient for massively parallel implementations. We have tested the scalability of our parallelized code by performing the same calculation on 2, 4, and 32 Cray T3E processors. The testing results are shown in Table 9, where it can be seen that the code scales almost linearly up to at least 32 processors.

6.2.4 Potentials for hydrogen isotopes

There are several effective pair potentials available for hydrogen isotopes.[143, 144, 145, 146] Pure pair potentials, such as those derived from high-level quantum mechanical methods, [147, 148, 149] are not suitable for use in condensed phase calculations because they ignore manybody effects. Previous work by Wang and Johnson [137, 138] has shown that the Silvera-Goldman (SG) potential [143] and the Buch potential [144] gave the best results for coexistence and single phase properties over a range of conditions for H_2, with the SG potential giving the best overall values. Since the value of the surface tension is strongly dependent on the equilibrium densities of vapor and liquids phases,[105, 73, 108] we adopted the SG and Buch potentials for our simulations. The SG potential [143] is given by

$$\phi(r) = \exp\left[\alpha - \beta r - \gamma r^2\right] - \left[\frac{C_6}{r^6} + \frac{C_8}{r^8} + \frac{C_{10}}{r^{10}} - \frac{C_9}{r^9}\right] f_c(r), \tag{6.7}$$

where $f_c(r)$ is a damping function of the form

$$f_c(r) = \begin{cases} e^{-\left(\frac{r_c}{r}-1\right)^2} & r < r_c \\ 1 & r \geq r_c \end{cases}. \tag{6.8}$$

The parameters for SG potential in atomic units are: $\alpha = 1.713$, $\beta = 1.5671$, $\gamma = 0.00993$, $C_6 = 12.14$, $C_8 = 215.2$, $C_9 = 143.1$, $C_{10} = 4813.9$, $r_c = 8.321$. The Buch potential has the standard Lennard-Jones form,

$$\phi(r) = 4\epsilon\left[\left(\frac{\sigma}{r}\right)^{12} - \left(\frac{\sigma}{r}\right)^{6}\right], \tag{6.9}$$

with $\epsilon/k = 34.2$, where k is the Boltzmann constant, and $\sigma = 2.96$ Å. Note that both the SG and Buch potentials are spherical. Thus, the rotational states of the molecules are not explicitly included in the simulations. The rotational states can be included approximately by using the ideal gas statistical mechanical expressions.

6.3 SIMULATION DETAILS

We have used multiple time-step PIHMC in the canonical or NVT ensemble to calculate the interfacial properties of hydrogen and deuterium and their mixtures. The reversible reference system propagator algorithm [150] was used to separate the intramolecular harmonic spring forces from the intermolecular forces. The velocity Verlet algorithm [90] was used to integrate the equations of motion. The harmonic forces were integrated with a time step that was ten times smaller than that used for the intermolecular forces. In each hybrid Monte Carlo move, ten long MD steps were used. The MD trajectories were carried out in the microcanonical (NVE) ensemble. The value of the long time step was adjusted during equilibration to achieve an acceptance ratio of roughly 50%. At the beginning of a single PIHMC move the positions of all particles were stored and the trajectories of all the molecules were allowed to evolve for ten long MD time steps. The change in the total energy was evaluated, and the move was accepted or rejected according to the conventional Metropolis Monte Carlo acceptance rule. If the move was accepted then the new positions were saved; otherwise the positions were reset to the previous values. In either case, new velocities were drawn at random from a Gaussian distribution at the desired temperature.

The simulation was started with molecules located on a face-center-cubic lattice in a cubic box. We chose densities slightly higher than the experimental liquid densities in order for the equilibrated liquid slab to have approximately the thickness of the starting box. For pure fluid simulations we employed 1024 molecules. For mixture simulations we employed a total of at least 3200 molecules. Periodic boundary conditions were applied in all three directions. After 2000 (5000 for mixtures) PIHMC moves to equilibrate the bulk liquid, empty cubic boxes of the same dimensions were added to each side of the liquid in the z-direction, allowing the vapor phases to develop. Typically another 40000 (100000 for mixtures) PIHMC moves followed to equilibrate and stabilize the interfaces. The production period included 40000 (100000 for mixtures) PIHMC moves to evaluate the surface tension. The VLE densities were determined from averages of density profiles in each phase, excluding the interfacial regions. We used a potential cutoff of 18 Å for all calculations. In the integration of Eq. (6.5) or (6.6), $\rho(r)$ was updated every 500 PIHMC moves using the current density profiles. The integration

was carried out using the trapezoid rule. The integration range for r was $r_c \leq r \leq 150$ Å. The integration units were $dr = 0.15$ Å, and $d\theta = \pi/200$.

Many of the calculations were performed on a Cray T3E supercomputer. Most simulations employed 32 processors, with each processor assigned $N/32$ molecules, where N is the total number of molecules. The calculations were performed according to the replicated data algorithm, described above, with the head node performing initialization and output of the final results.

As a comparison, we also performed regular classical MD simulations to calculate the interfacial properties of H_2 and D_2. The simulation conditions were same as those used for PIHMC and the SG potential was used. Quantum and classical simulation results will be compared in the following section.

6.4 RESULTS AND DISCUSSION

6.4.1 Pure H_2 and D_2

We first consider the interfacial properties of pure hydrogen isotopes. We calculated the coexisting densities and surface tension values for hydrogen and deuterium using both the SG and Buch potentials. The temperature range covered for H_2 was from 18 to 30 K and 18 to 34 K for D_2. We were able to observe clear vapor-liquid phase separation over these temperature ranges. The experimental critical temperatures for normal-H_2 (75% ortho) and normal-D_2 (75% para) are 33.19 K and 38.34 K, respectively. Density profiles for H_2 calculated from simulations at two different temperatures are shown in Fig. 28.

The VLE phase diagrams of H_2 and D_2 from simulations are shown in Figs. 29 and 30. The ability to compute accurate orthobaric vapor and liquid densities is a necessary condition for computing accurate values of the surface tension because the surface tension depends critically on the difference between coexisting vapor and liquid densities.[73, 105, 108] We observe from Figs. 29 and 30 that PIHMC simulations with the the SG potential give saturated liquid and vapor densities in good agreement with experimental data[151, 152] for both H_2 and D_2. In contrast, classical simulations with the SG potential, also shown

in Figs. 29 and 30, failed to give even qualitative agreement. The classical simulations overestimate the liquid density of H_2 by about 45% and the liquid density of D_2 by about 30% on average. Interestingly, the Buch potential is not as accurate for D_2 as for H_2. It should be noted that we used exactly the same potential for both isotopes of hydrogen. Therefore, the VLE diagrams of the two isotopes from classical simulations are exactly the same in terms of molar density. The assumption that the pair potentials for different hydrogen isosoptes are identical is not exactly valid, as D_2 has a slightly shorter bond length and lower polarizability than H_2, but these effects are relatively small. The main factor in determining the differences in interfacial properties of the isotopes is the difference in quantum effects, due to the change in mass. Values of the surface tension for pure H_2 and D_2 as a function of temperature are plotted in Fig. 31 and Fig. 32, respectively. The results from quantum simulations are in excellent agreement with experimental data.[151, 152, 153] As a comparison, classical simulations overestimate the surface tension by as much as a factor of three. Note that, in the absence of quantum effects, the surface tension of H_2 and D_2 are identical within the approximation of the potentials used in this study. As with the VLE densities, simulated values of the surface tension using the SG potential are in very good agreement with experimental data for both H_2 and D_2, while the Buch potential works better for H_2 than for D_2. We found that the long range corrections contribute about 10% to 15% to the values of simulated surface tension. This confirms the importance including of long range corrections when simulating surface tension.

The critical temperature (T_c) and surface tension of quantum fluids are lowered significantly due to the quantum effects, as can be seen by comparing the results from path integral and classical simulations in Figs. 29-32. Quantum effects can be divided into diffraction (zero point motion) and symmetry (indistinguishability) effects. Our implementation of the path integral formalism includes the former but not the latter. The use of Boltzmann statistics (distinguishability) is a very good approximation for liquid hydrogen isotopes. The lowering of the surface tension for quantum H_2 compared with "classical" H_2 (see Fig. 31) is mainly a result of the larger saturated liquid densities of the classical fluid.

Faizullin has recently proposed a method for calculation of fluid surface tensions by correlating the surface tension of pure nonpolar fluids in terms of thermodynamic similarity.[112]

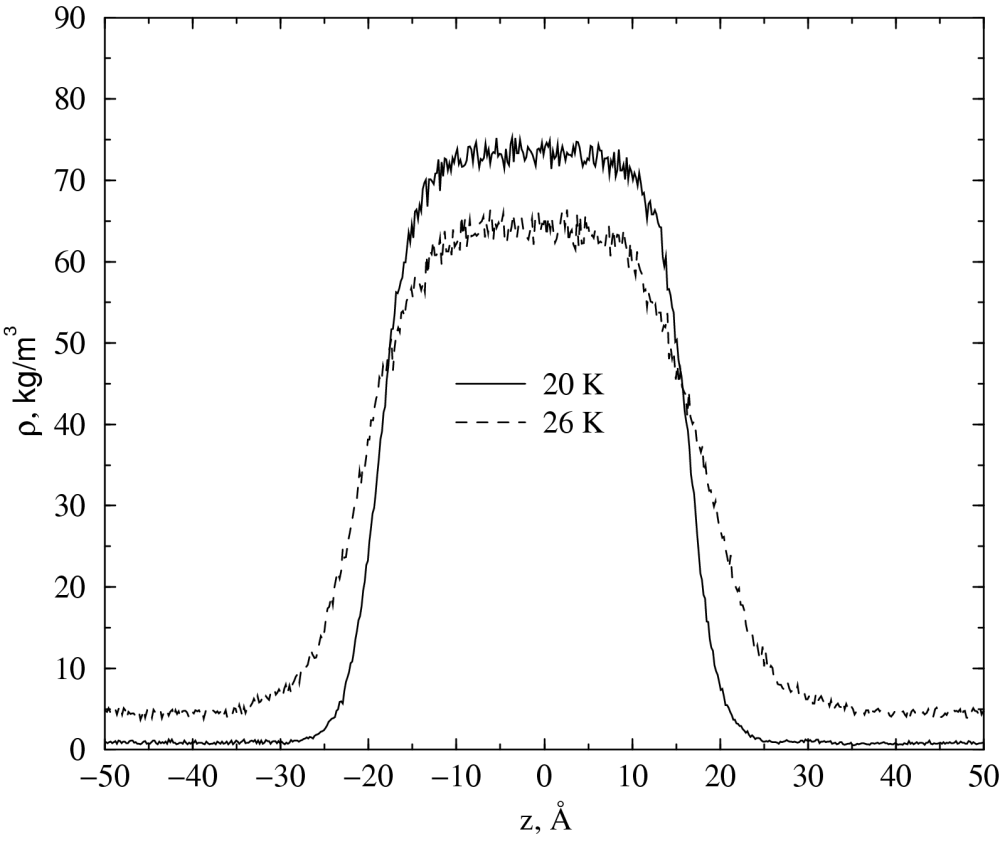

Figure 28: Density profiles from vapor-liquid interfacial simulations of H_2 at 20 K (solid line) and 26 K (dashed line). The SG potential was used in the simulations.

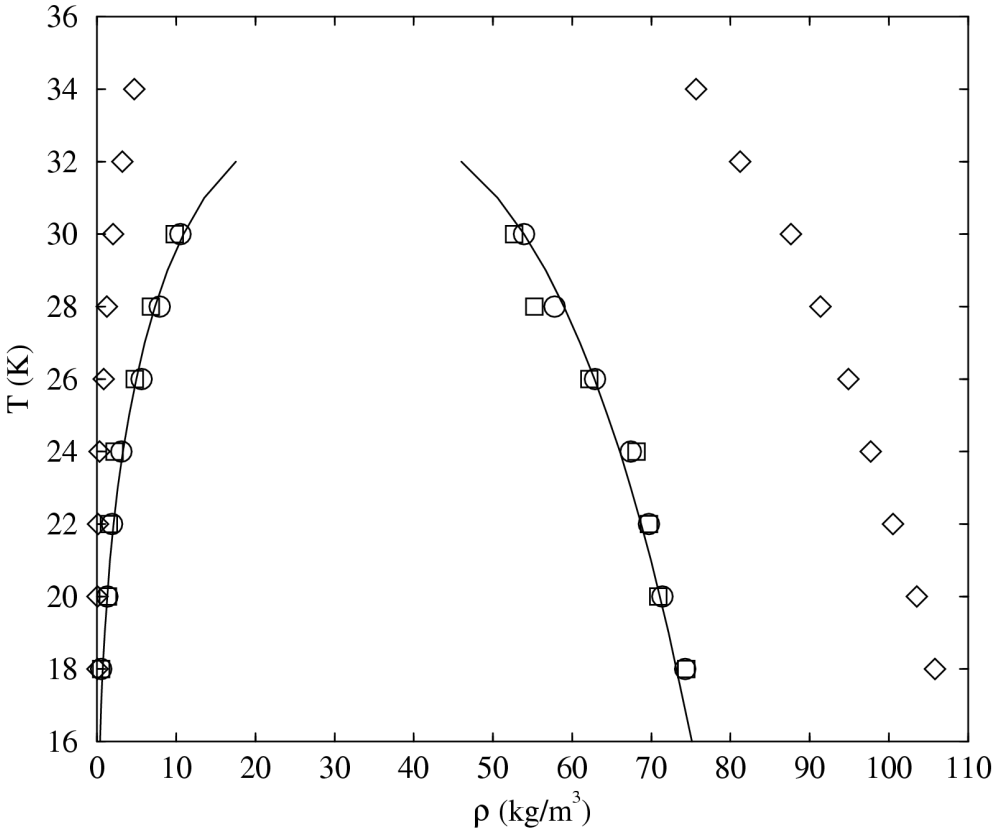

Figure 29: The vapor-liquid phase diagram of H_2 from simulations and experiments. The solid line represents experimental data.[151] The circles are PIHMC simulations with the SG potential, the squares are PIHMC simulations with the Buch potential, and the diamonds are classical simulations with the SG potential.

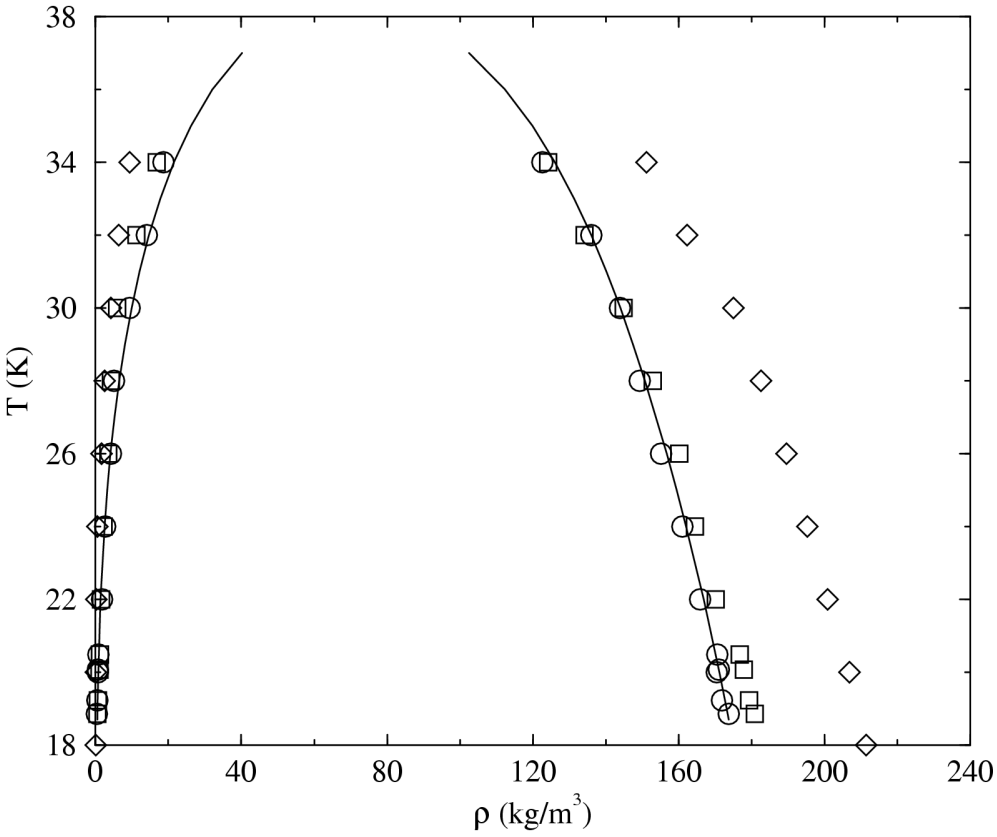

Figure 30: The vapor-liquid phase diagram of D_2 from simulations and experiments.[152] The line and symbols have the same meaning as in Fig. 29.

This method relates the surface tension of a fluid to the vaporization enthalpy per unit volume of the liquid phase by

$$\gamma^* = \left(\frac{\Delta h^*}{v^*} \right)^m , \tag{6.10}$$

where $m = 2.15$ is an adjustable parameter and γ^*, Δh^*, and v^* are the reduced surface tension, vaporization enthalpy, and specific volume of coexisting liquid phase, respectively. These are given by

$$\gamma^* = \frac{\gamma}{(\gamma)_{T_r=0.6}}, \tag{6.11}$$

$$\Delta h^* = \frac{\Delta h}{(\Delta h)_{T_r=0.6}}, \tag{6.12}$$

$$v^* = \frac{v}{(v)_{T_r=0.6}}, \tag{6.13}$$

where $T_r = T/T_c$. This method is very successful at correlating the surface tension for classical pure non-associated fluids ranging from argon to hexafluorobenzene.[112] It is interesting to ask whether this same relationship holds for quantum fluids as well. We have therefore used Faizullin's method to correlate the experimentally measured values of surface tension for H_2 and D_2. The results are shown in Fig. 33. The thermodynamic similarity method does not work well for H_2. The shape of the predicted curve [solid line, Fig. 33(a)] is wrong. Indeed, no value of m is able to adequately account for the curvature of the H_2 data. A least-squares fit of the H_2 data to Eq. (6.10) gives a value of $m = 2.11$, which produces a curve that is virtually indistinguishable from the solid line plotted in Fig. 33(a). On the other hand, the thermodynamic similarity methods appears to work fairly well for D_2, as shown in Fig. 33(b). We expect that if the D_2 surface tension data were extended to lower temperatures one would also see a sharp upturn in the value of γ^*, as is seen for the H_2 data below a temperature of about 18 K. However, the triple point of D_2 is about 18.7 K, so that the sharp upturn may not be observable.

6.4.2 H_2-D_2 mixtures and surface segregation

We have performed calculations on the properties of H_2/D_2 mixtures and have compared our results with experimental data where possible. [154] We adopted the SG potential for

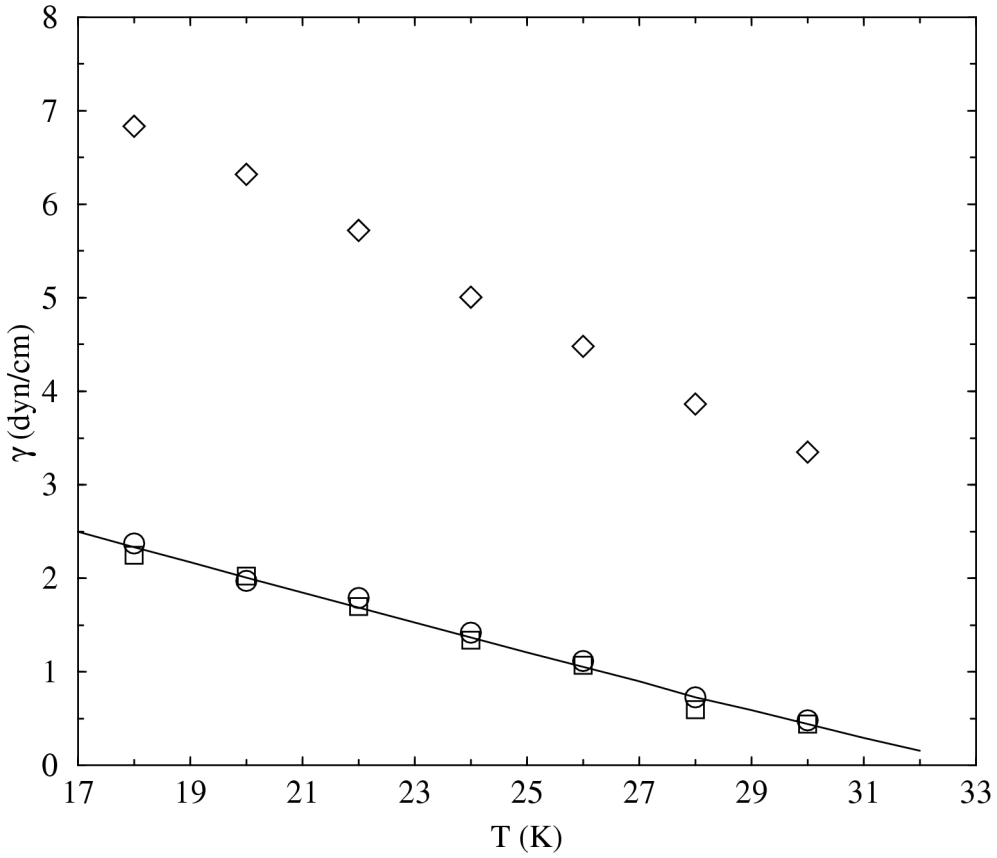

Figure 31: Surface tension of pure normal-H_2 calculated from simulations. The solid line represents experimental data.[151] The circles are PIHMC simulations using the SG potential, the squares are PIHMC simulations using Buch's potential, and the diamonds are classical simulations with the SG potential.

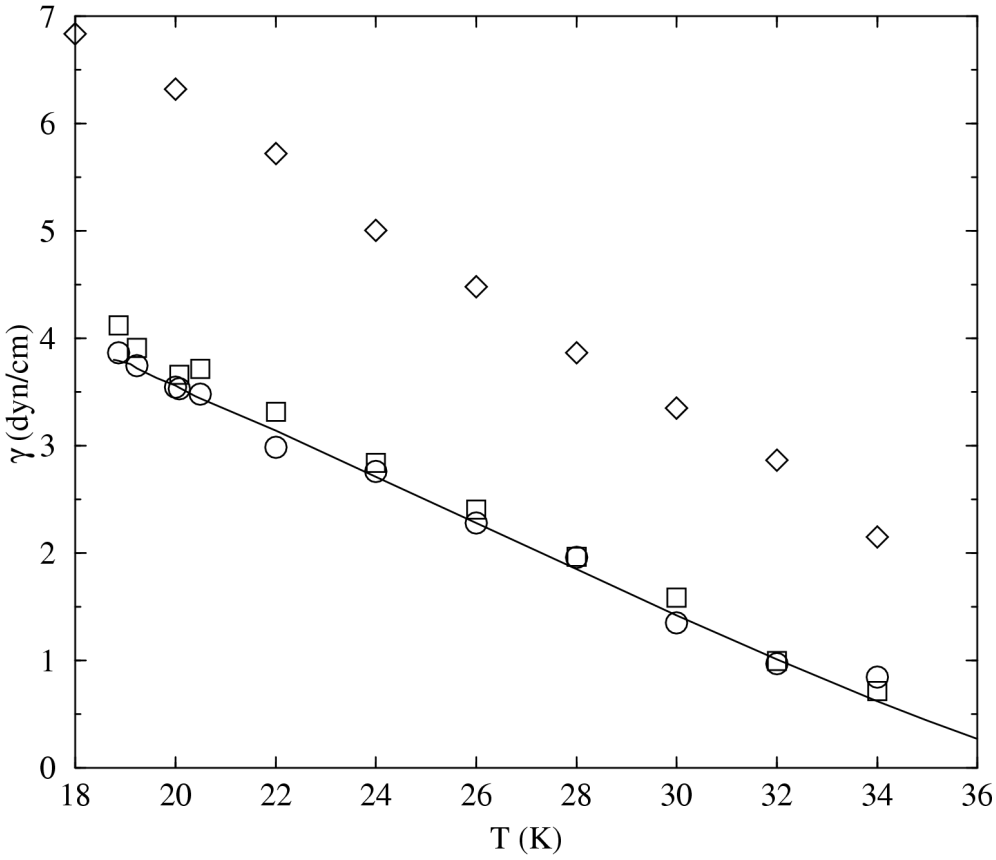

Figure 32: Surface tension of pure normal-D_2 as a function of temperature. The line represents experimental data.[152, 153] The symbols have the same meaning as in Fig. 31.

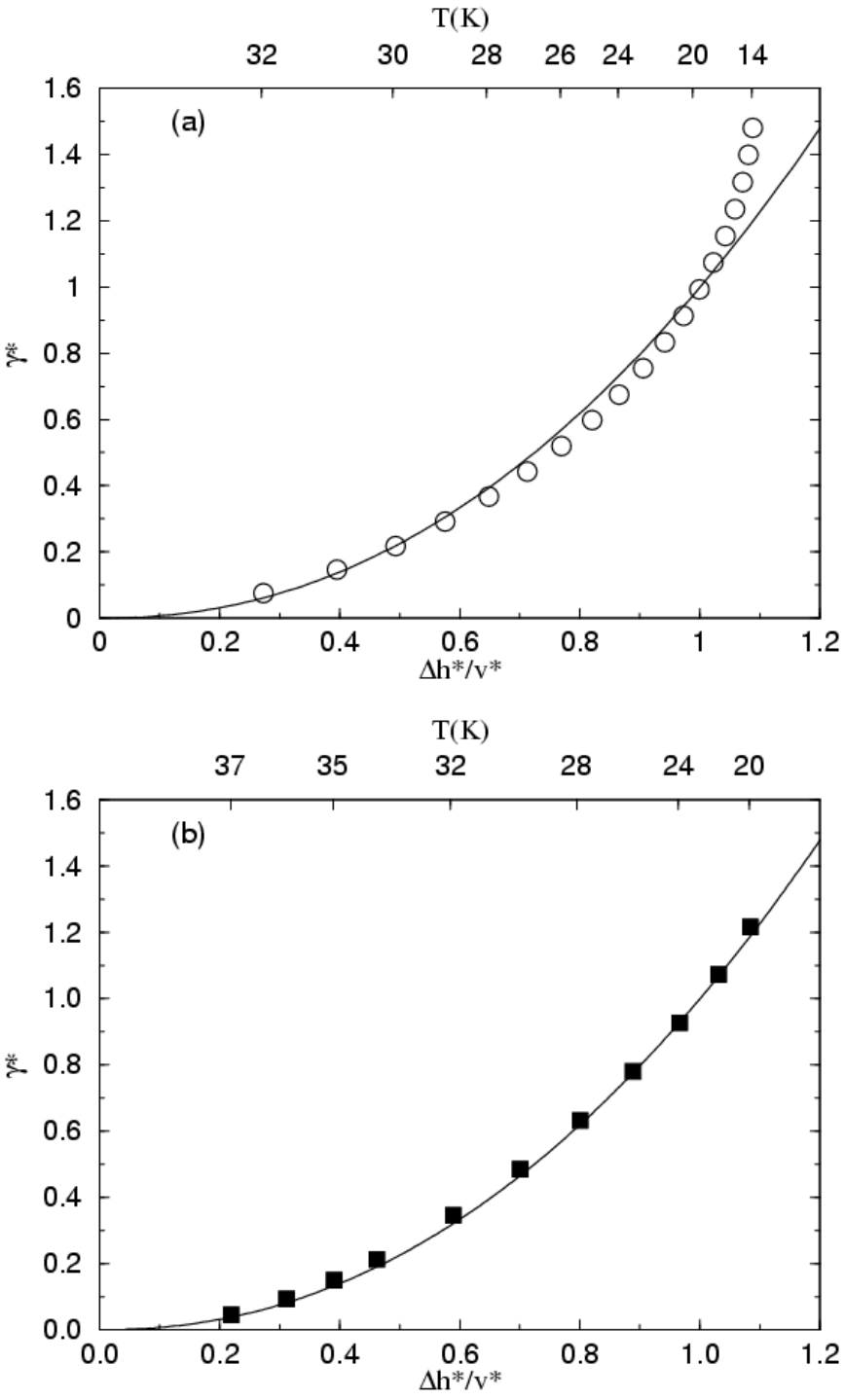

Figure 33: Surface tension of pure H_2 (a) and D_2 (b) calculated from the method of thermodynamic similarity.[112] The line are calculated from the theory. The circles and filled squares are experimental data for H_2 and D_2, respectively. The top x-axis on each graph gives the temperature at selected points.

the simulation of mixtures because it performs well for pure fluids of both isotopes. In Fig. 34 we compare VLE compositions calculated from simulations with those measured from experiments. The simulation data are in excellent agreement with the experimental data.

Values of the surface tension for H_2/D_2 mixtures at 24 K are plotted in Fig. 35. The dashed line represents the surface tension for an ideal mixture,

$$\gamma_{\text{id}} = \sum_i x_i \gamma_i. \tag{6.14}$$

The relative excess surface tension,

$$\Delta\gamma/\gamma_{\text{id}}, \tag{6.15}$$

is also plotted in Fig 35, where

$$\Delta\gamma = \gamma - \gamma_{\text{id}}. \tag{6.16}$$

Note that the H_2/D_2 mixture exhibits negative deviations from ideal behavior, $\Delta\gamma/ \leq 0$. Negative deviations from the ideal solution surface tension for mixtures of H_2 and D_2 have been observed by Grigoriev and Rudenko.[155] They reported negative deviations ranging of as much as -4.2% at a temperature of 20.4 K. They point out that the trends of their data are in qualitative agreement with Prigogine's theory for quantum mixtures.[155, 156, 157] However, their calculations of Prigogine's theory gives a larger magnitude for $\Delta\gamma/\gamma_{\text{id}}$; they report a value of about -12% for an equimolar mixture of H_2 and D_2 at 20.4 K. Note that our simulations are in quantitative agreement with Prigogine's predictions. The nonideal behavior of the H_2/D_2 mixture is purely due to quantum effects. A classical simulation of the mixture gives surface tension values identical to those of the pure fluid. This is in contrast to nonideal behavior observed in Ne/H_2 mixtures, which was shown to be due to differences in the cross interaction potential rather than to quantum effects.[158]

The lowering of the mixture surface tension relative to a mole fraction average of the pure component values can be understood in terms of enrichment of H_2 at the interface. The density profiles of H_2 and D_2 for a bulk liquid concentration of $x_{H_2} = 0.22$ are plotted in Fig. 36. Surface segregation is not obvious from this plot. However, if we transform the

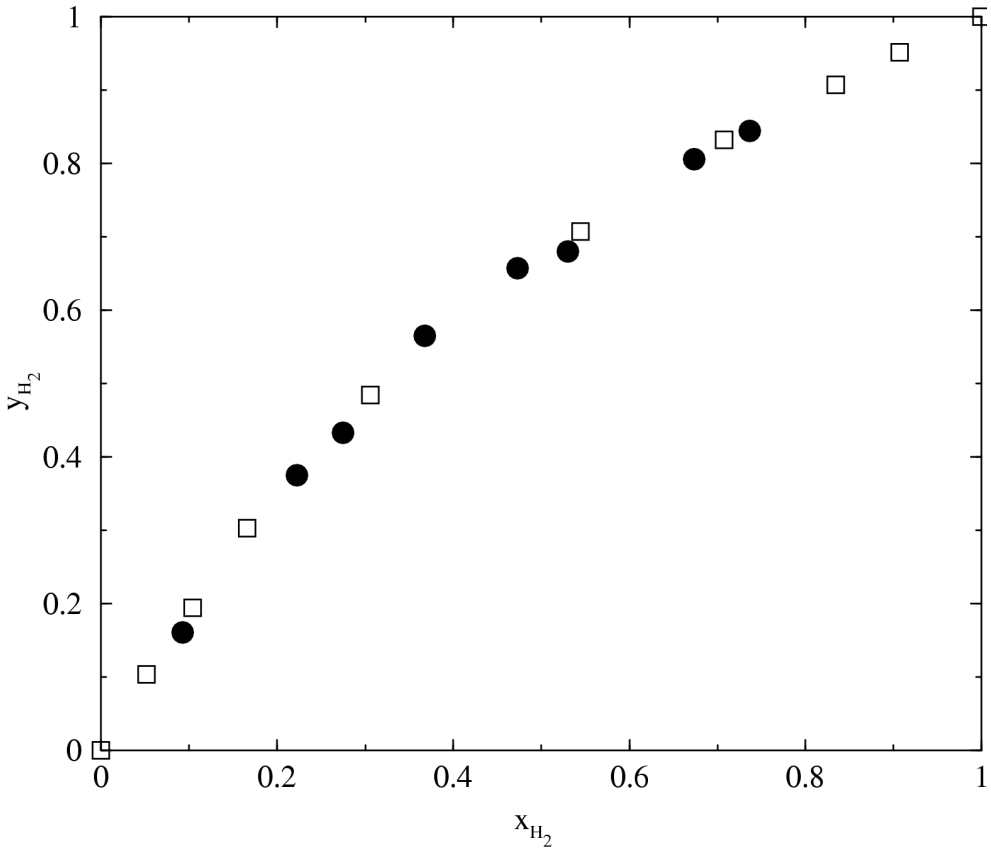

Figure 34: Saturation vapor (y) and liquid (x) compositions for H_2/D_2 mixtures at 24 K The squares are experimental data[154] and the filled circles are PIHMC simulation results using the SG potential.

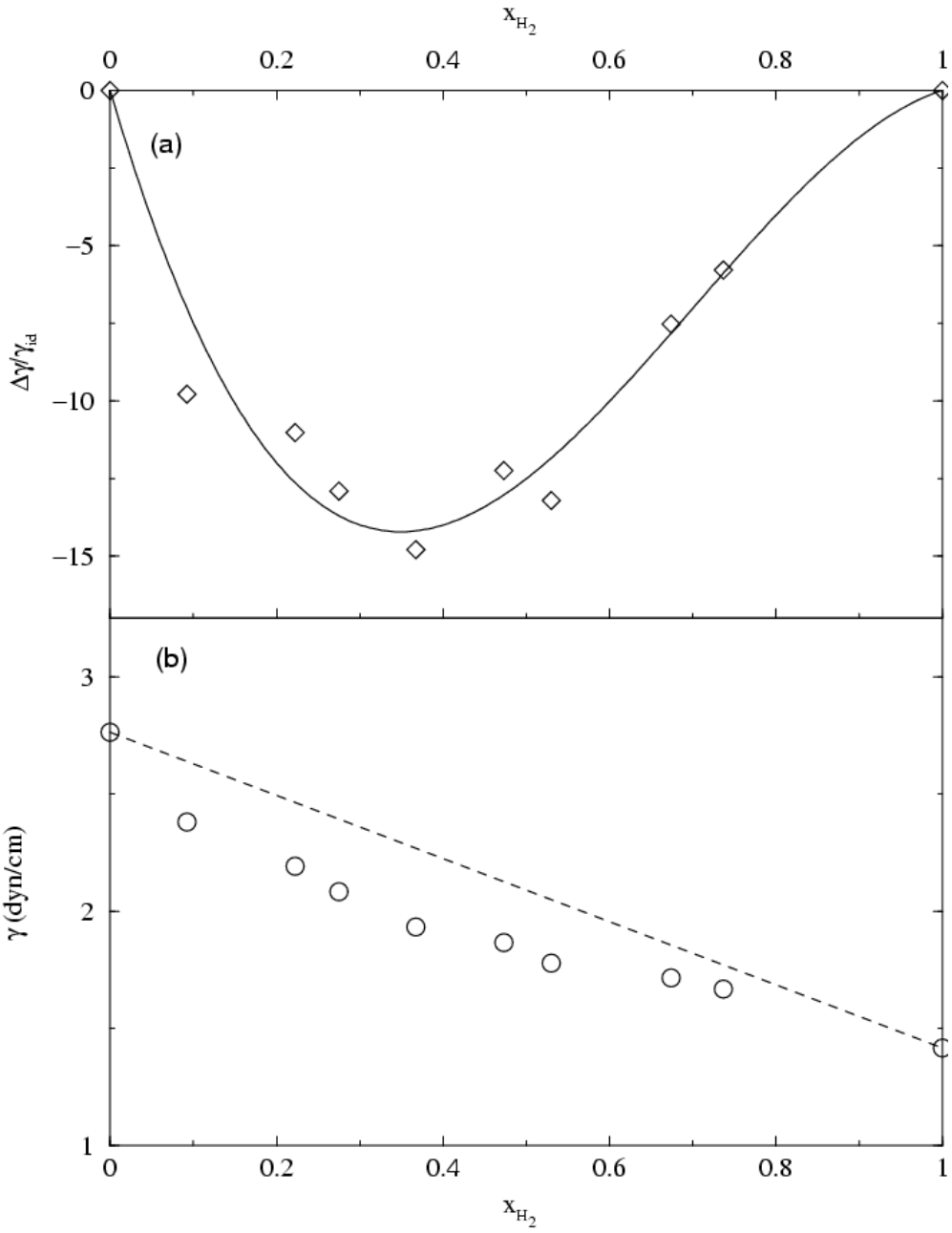

Figure 35: Surface tension of H_2/D_2 mixture at 24 K as a function of the liquid composition calculated from simulations. (a) The relative excess surface tension (diamonds) from Eq. (6.15). The solid line is drawn as a guide to the eyes. (b) The circles are simulation results from the SG potential and the dashed line is the ideal mixture value, γ_{id} given by Eq. (6.14).

data using the symmetrized surface segregation function $\Delta C(z)$,[159] we can observe clear evidence of surface segregation. The function $\Delta C(z)$ is given by

$$\Delta C(z) = \frac{\rho_1(z) - \rho_1^l}{\alpha_1} - \frac{\rho_2(z) - \rho_2^l}{\alpha_2}, \tag{6.17}$$

where α_i is defined as

$$\alpha_i = \frac{\rho_i^l - \rho_i^v}{(\rho_1^l + \rho_2^l) - (\rho_1^v + \rho_2^v)}. \tag{6.18}$$

In Eqs. (6.17) and (6.18), the subscripts 1 stands for H_2, 2 for D_2, the superscript l stands for liquid, and v for vapor. Figure 37 is a plot of $\Delta C(z)$ as a function of z determined from the density profiles in Fig. 36. The two large peaks at the interfaces show that H_2 migrates to the interface, thus lowering the overall free energy of the system by reducing the surface tension. The fluctuations in the data and differences in the peak shapes are due to insufficient sampling. The segregation evident in Fig. 37 indicates that H_2 acts as a surfactant in the H_2/D_2 mixture. Similar phenomena have been noted for mixtures of $^3He/^4He$ and He/H_2. [160, 161, 162] In these cases, the component having a lower pure fluid surface tension segregates to the interface, acting as a surfactant for promoting wetting on alkali metal surfaces. The segregation of the lower surface tension component to the interface was also observed from simulations of classical mixtures.[132]

6.5 CONCLUSION

We have calculated the surface tension of hydrogen isotopes and their mixtures from molecular simulations using the path integral hybrid Monte Carlo technique. The surface tension and coexisting densities of pure H_2 and pure D_2 obtained from simulations are in good agreement with experimental data. Quantum effects are seen to be extremely important for these fluids, as shown by comparison of the path integral simulations with classical calculations. We have used the SG and Buch potentials in the simulations. The SG potential is accurate for both H_2 and D_2, while the Buch potential is not as accurate for D_2 as for H_2.

We have calculated interfacial properties for H_2/D_2 mixtures at 24 K. The VLE compositions obtained from simulations agree very well with available experimental data for the

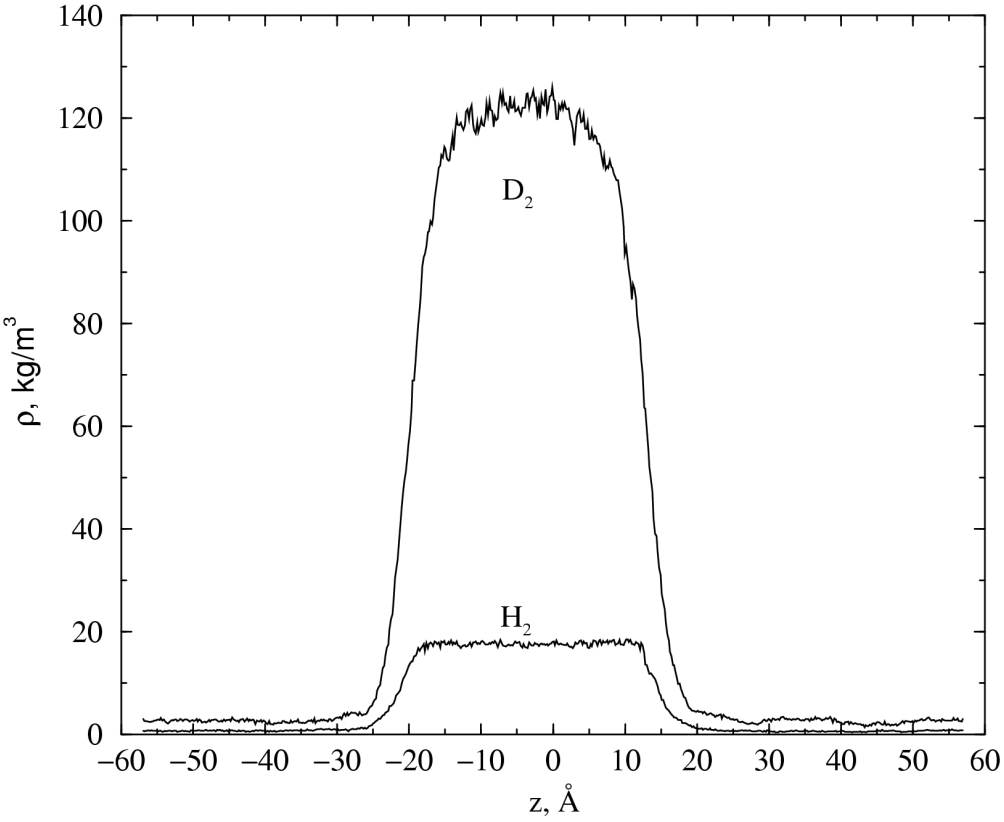

Figure 36: The density profile of H_2-D_2 mixtures at 24 K with $x_{H_2} = 0.22$.

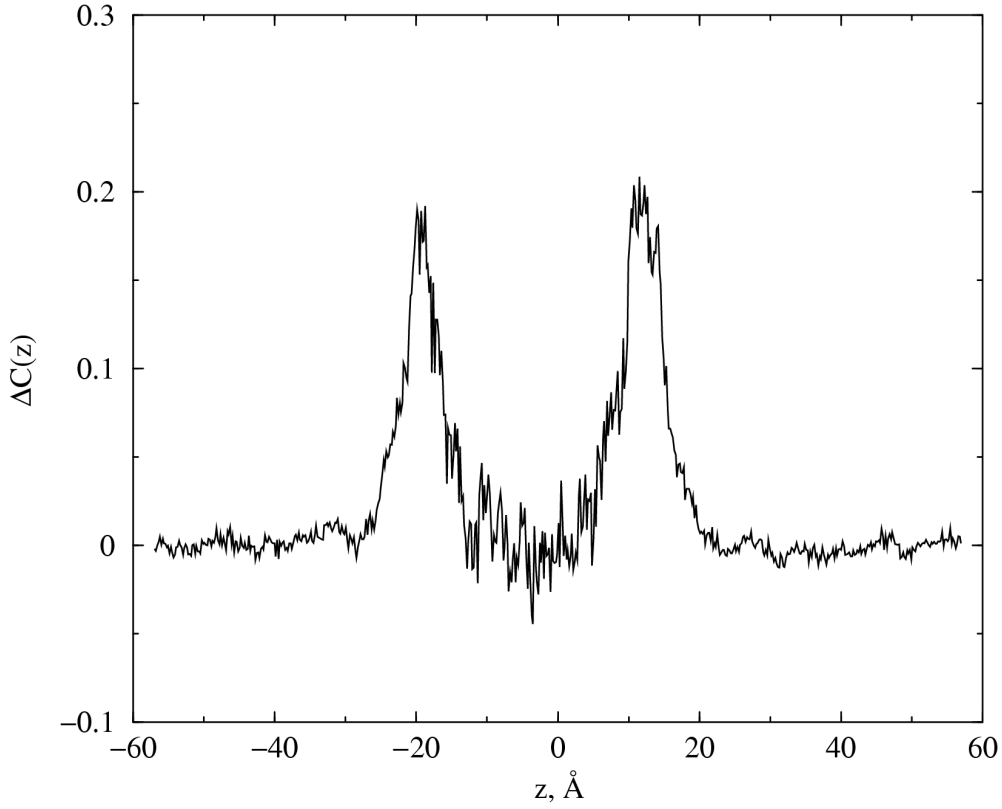

Figure 37: The symmetrized surface segregation function $\Delta C(z^*)$ for a PIHMC simulation at 24 K with $x_{\mathrm{H_2}} = 0.22$.

compositions of the liquid and vapor phases. We have calculated the surface tension of the mixture at 24 K over the entire composition range. The mixture surface tension exhibits negative deviations from ideal solution behavior. Surface segregation of H_2 contributes to the surface tension lowering. The segregation is due solely to quantum effects. Our simulations are in qualitative agreement with experiments for H_2/D_2 mixtures, although our values of $\Delta\gamma/\gamma_{\rm id}$ are about a factor of three larger in magnitude than experimental values. Our simulations are in good quantitative agreement with predictions from Prigogine's theory for quantum mixtures.

7.0 SIMULATION OF DNA SEGMENT AND CARBON NANOTUBE IN WATER

7.1 INTRODUCTION

The first atomic simulations were performed in the early 1950's. [163] However, the large-scale simulation of macro-biomolecules was not possible until the mid 1990s. [164] The major problem was the limitation of computing power. Before massively parallel computers appeared, it was impossible for researchers to apply computationally accurate techniques such as Ewald summation [165] to treat the electrostatic interactions encountered in simulating biomolecules because of the tremendous system size involved. It was long recognized that the proper handling of long-range electrostatic forces for highly charged systems like proteins in solution is essential in order to obtain reliable simulation results. Limitation of computing power also prohibited the development of accurate empirical potential functions for biomolecules.

In the past decade important progress has been made in the simulation of biomolecules due to the development of more powerful computers, more accurate empirical force fields such as CHARMM [166] and AMBER [167], and more efficient simulation methods like the particle mesh Ewald technique. [168] It is now routine to run simulations of proteins containing thousands of atoms lasting up to tens of ns in atom explicit water with a proper treatment of the long-range electrostatic interactions. [169] Satisfactory agreement had been obtained between the simulation data and experiments on the structures and dynamics of DNA molecules in solution. [170]

Numerous experimental and simulation studies have been performed on carbon nanotubes. Interest in carbon nanotube is due to their novel mechanical and electronic prop-

erties. [171, 172] Research has focused primarily on three areas: adsorption, [173, 174] electronic properties, [175, 176] and mechanical properties. [177, 178] Some potential applications of nanotubes involving macro-biomolecules like DNA have also been proposed. For example, nanotubes have been used as experimental tips in AFM to image biological nanostructures, such as DNA strands. [179, 180] It has been found that aligned SWNT bundles exhibited superior resolution compared to conventional tips when probing biomolecules. [179, 180] Another possible application is using a single nanotube to mark the mutation regions of the DNA that are associated with diseases. [181] Recent experiments have shown that DNA molecules may be used to separate nanotubes, [182, 183] or used as 'molecular Velcro' to assemble target nanostructured materials by preattaching nanotubes to each strand of the DNA double helix before they recombine. [184]

All of the above potential applications of DNA together with SWNT requires a better understanding of the forces between DNA and SWNT in solution. In this study, we focus on the behavior of a DNA segment with a SWNT in an aqueous solution. Our simulation studies employed the potentials and techniques used in simulating DNA in solvents without other external forces, together with those developed for simulating carbon nanotubes. We have investigated (1) the adsorption of the DNA segment on charged and neutral SWNTs; (2) the dynamics of the DNA segment in an aqueous environment in the presence of a SWNT; (3) the structural and conformational changes of a DNA segment in the presence of a SWNT.

7.2 SIMULATION METHODOLOGY

We have used the commercially available MD software package, AMBER version 7 as the simulation engine for this work. AMBER is one of the most extensively used programs employed in parallel simulation of biomolecules. This software package has been well tested and proved effective and robust for study of bio-molecular systems. [170] It was also shown that simulation of SWNTs can be carried out successfully with AMBER. [185, 186]

AMBER is the collective name for a suite of programs that allows users to carry out molecular dynamics simulations, particularly on biomolecules. It includes programs in three categories, (1) preparatory programs; (2) simulation programs; and (3) analysis programs.

The preparatory programs include `LEaP` and `Antechamber`. The simulation programs include `Sander`, `Gibbs`, `Nmode`, and `Roar`. The analysis programs include `Anal`, `Ptraj`, `Carnal`, `Nmanal/Lmanal`, and `MM-PBSA`. In this work, `LEaP`, `Sander`, `Carnal`, and `Anal` are most extensively used.

`LEaP` functions as the major program for preparing input files for the simulations. It can be used to set up the initial structures of molecules, allocating the proper potential parameters, and generating the necessary input files to be read by the simulation programs. One can also use commands in `LEaP` to build new molecules or residues that are not included in the AMBER libraries.

`Sander` is the major simulation engine in the AMBER that can perform energy minimization and molecular dynamics. `Sander` provides support for several force fields for proteins and nucleic acids, for several water models and other organic solvents. The particle mesh Ewald procedure is a standard choice in `Sander` for handling long-range electrostatic interactions.

`Carnal` is the most commonly used analysis program in AMBER. It is a general purpose utility for analyzing and processing trajectory or coordinate files created from MD simulations. It can be used to calculate the distance and angles between atoms, residues, and planes formed by atoms or residues. It can also be used to extract snapshot coordinates of the simulation box and used to calculate root mean square displacements (RMSDs). Nearly all the information involving dynamics can be obtained by using `Carnal` to process the trajectory files generated during simulations.

`Anal` is the energy analysis module of AMBER. Its purpose is to do energetic analysis of individual structures. The key function of this program is decomposition of the energy among different groups of atoms in order to find the interaction energies between different parts of the systems.

7.3 POTENTIALS

7.3.1 Potential models for the DNA segment

Inter- and intra-molecular interactions are typically described by the following potential function:

$$\begin{aligned} U &= \sum_{bonds} k_b(r - r_{eq})^2 + \sum_{angles} k_\theta(\theta - \theta_{eq})^2 + \sum_{dihedrals} \sum_{n} \frac{V_n}{2} \\ &\times [1 + \cos(n\phi - \gamma)] + \sum_{i} \sum_{j>i} \left[\left(\frac{A_{ij}}{r_{ij}^{12}} - \frac{B_{ij}}{r_{ij}^{6}} \right) + \frac{q_i q_i}{\epsilon \cdot r_{ij}} \right]. \end{aligned} \tag{7.1}$$

The first two terms in the equation involve the potential energy of distortion from equilibrium bond lengths and bond angles (r_{eq} and θ_{eq}). The constants k_b and k_θ come from empirical data on vibrational frequencies of molecular fragments. The next three terms reflect the torsional, van der Waals, and electrostatic forces. The torsional energy function describes the energy as a function of rotation angle around a given bond described by four atoms connected in series. The parameters for the torsional term are usually fitted to reproduce the energies from *ab initio* calculations. The parameters for van der Waals and electrostatic interactions are based on empirically derived values for molecular segments of small molecules, or obtained from high level quantum calculations.

Currently available potential models for biomolecules include the one developed by Cornell *et al.*, [167] which is used in the AMBER software package, the CHARMM potential, [166] which is used in the CHARMM software package, the OPLS model, [187] which is used in the BOSS software package, and the GROMACS potential, [188] which is used in the GROMOS software package. The most widely adopted potentials are AMBER and CHARMM. Both AMBER and CHARMM potentials have been proved to be successful for simulating proteins. [170]

7.3.2 Potential models for SWNTs

The interaction of the DNA segments with a SWNT can be expressed as

$$U = \sum_{N_D} \sum_{N_C} (u_{disp} + u_{qq}). \tag{7.2}$$

Here N_D and N_C denotes number of DNA atoms and SWNT atoms, respectively. u_{disp} is the dispersion and repulsion interactions between an atom in the DNA segments and a carbon atom in the SWNT. u_{qq} stands for the electrostatic interaction between a DNA atom and a SWNT carbon atom if the SWNT is charged. For dispersion and repulsion interactions, available potentials for SWNT include the isotropic Lennard-Jones potential and the Crowell-Brown potential. [189] We adopted the atom explicit Lennard-Jones potential because it is simple to implement and computationally faster than the Crowell-Brown potential. For the Lennard-Jones parameters of SWNT carbon atoms, we chose parameters similar to those used by Hummer *et al.*, [185] with $\epsilon_C/k = 43.2$ K, and $\sigma_C = 3.4$Å. These parameters correspond to the sp^2 carbon in the AMBER '99 force field. [167] The Lennard-Jones cross interactions between different atoms are calculated by Lorentz-Berthelot combining rules. For charged nanotubes, we simply add desired amounts of charge uniformly at the centers of carbon atoms in the SWNT. [189]

7.3.3 Potential models for water

Explicit representation of water molecules in the system plays an important role when simulating biomolecules in aqueous solutions. For the calculation of DNA segments in water this is even more essential since the nucleic acid groups are highly charged species. Their interaction with the electrostatic water molecules often determines the conformational behavior and thus the properties of the DNA fragment. There are a large number of water potentials available for simulations. [190, 191, 192, 193, 194, 195, 196] Comparison of these potentials [196, 197] has also been carried out by simulations, but there are still controversies on them. These water potentials have both strengths and weaknesses. By far the most widely used ones include three and four point transferable interaction potentials (TIP3P [192], TIP4P [196]), simple point charge (SPC [190]) potential, and extended simple point charge (SPC/E [191]) potential. SPC and TIP3P potentials are standard choices for AMBER. Successful protein simulations have been performed with both of them. [169] In this work we have used TIP3P as the potential for water because the TIP3P was most extensively used for simulating bio-systems and had been shown to give accurate results. [169, 170]

7.4 SIMULATION DETAILS

The typical simulation box has a starting size of about $70 \times 65 \times 70$ Å^3 that contains about 4600 TIP3P water molecules. The water molecules were added into the box using the equilibrated water box provided in AMBER to save equilibration time. We have used a (8,8) 'armchair' type SWNT [171] with 576 carbon atoms. The nanotube has a length of 44.3 Å and a diameter of 10.7 Å. The SWNT carbon-carbon bond length is 1.40 Å and the bond angles are 120°. The DNA segment we modeled was a Dickerson Dodecamer, d[CGCGAATTCGCG]$_2$. The structure of the DNA segment was produced using the program `nucgen`, which is provided in AMBER. This DNA segment has a backbone length of about 40 Å. The typical center of mass distance between each of the base pairs is about 11.7 Å.

For most of the simulations, the DNA and SWNT are initially placed parallel to each other in the box. The distance between the axis of the DNA duplex and the box origin is 10 Å, which is same as that between the SWNT axis and the box origin (see Fig. 38). Throughout the simulation, water molecules and the atoms of the DNA segment are free to move in the box, while the atoms of the SWNT are held fixed. Counter ions were added to maintain charge neutrality.

Molecular Dynamics simulations were performed at a constant pressure of 1 bar and a temperature of 300 K. [198] The particle-mesh-Ewald method [168] with a fourth order interpolation was applied to evaluate electrostatic interactions. The time step used was two femtoseconds and the structures were saved every two picoseconds.

The setting up of the starting configurations and initial equilibrations were carried out on a local workstation. The production simulations were performed on the Lemieux Cluster at the Pittsburgh Supercomputing Center. A typical 3 nanosecond simulation takes about 33 hours on 16 CPUs on the Lemieux Cluster. Data analysis were performed on local workstations. Typically, the procedures of a simulation include the following steps:

- Preparing the initial configurations using `LEaP`
  - Generate DNA structure using `nucgen`.
  - Relax the hydrogen atoms in the DNA segment using `Sander`.
  - Build a SWNT residue from the PDB file so that it can be read into the AMBER

using `LEaP`. This step includes setting up the proper potential parameters for the SWNT potential in the AMBER library.

  - Edit the DNA-SWNT structure and solvate the box with TIP3P water molecules. Add in the counter ions to make the system neutral if necessary.
  - Generate a topology file and a coordinate file using the standard AMBER '99 potential models.

- Equilibrating the system using `Sander`
  - Initial energy minimization holding the DNA and SWNT fixed.
  - Initial dynamics holding the DNA and SWNT fixed.
  - Relax the DNA segment gradually with energy minimization and dynamics after each relaxation step, with the SWNT held fixed. Typically five steps are needed to fully relax the DNA segment.
  - Equilibration for 20 picoseconds after the DNA is fully relaxed (free to move); the SWNT is held fixed.

- Production simulations using `Sander`
  - Run simulation for 3 nanoseconds, using the equilibrated structures as the starting configuration. During the production period the information on structure, potential energy, pressure, temperature, etc. are collected.

- Data analysis
  - Use `Carnal` to look at the atomic positional fluctuations over a dynamics run.
  - Use `Anal` to calculate the binding energy between DNA and SWNT.
  - Use `ambpdb` command to generate snapshot files in PDB format.
  - Use `process_perl` program in the packages to extract temperature, pressure, energetics, water density etc. as functions of time from MD output files.
  - Use free software like `gopenmol` or `MD-display` or `VMD` to generate movies of the dynamics.

A sample input files for the above procedures can be found in the Appendix.

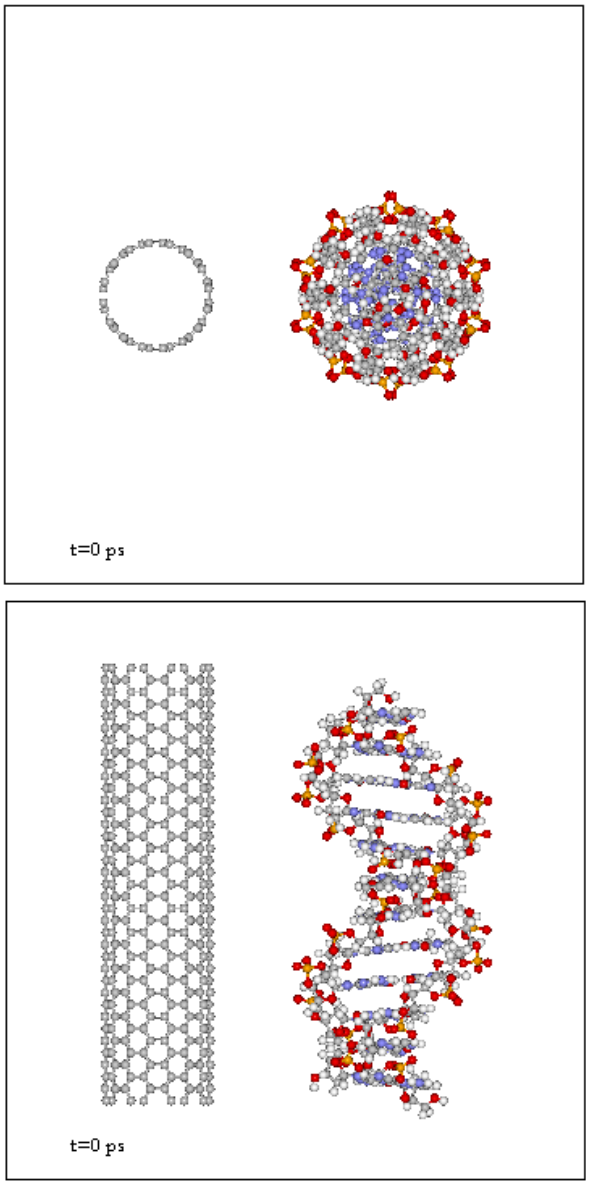

Figure 38: The starting configuration of DNA and SWNT in water. Water molecules are omitted in this figure. Here we show both the top-view and side-view of the starting configuration.

7.5 RESULTS AND DISCUSSION

7.5.1 The DNA segment in water

We began our study from MD simulations of the Dickerson dodecamer d[CGCGAATTCGCG]$_2$ in water without putting the SWNT in the system. This DNA segment has previously been studied using AMBER. [170, 199, 200] Our simulation were carried out at the same conditions as those used by Cheatham and Young. [170] We compared our simulation results with the previous work to make sure our simulation method was working properly.

We chose to study the transition of the A-form DNA to the B-form DNA in an aqueous environment to test our simulation methodology. One of the early success of the AMBER package was that spontaneous A-DNA to B-DNA transitions could be observed in simulations of various DNA molecules under physiological conditions. [169] In order to be able to observe this transition, one needs to set up the molecular structures correctly and equilibrate the simulation box properly. Thus, studying of the A-B transition of the DNA segment is a comprehensive test of the proper usage of the techniques and methods in AMBER.

In Fig. 39 we show structures of the A-form and B-form of the Dickerson Dodecamer. The A-form DNA is only stable under high salt solution conditions. So, we expect the DNA segment to transform to the stable B-form structure under low salt solution conditions we use in this study. The major differences between the structures of the A and B forms includes: (1) The B-DNA has a more clear major and minor groove structure than the A-DNA; (2) The rise along the axis per each base pair for a B-DNA is 0.34 nm, while that for an A-DNA is 0.255 nm; (3) The rotation of the helix per base pair for B-DNA is 36°, while that for A-DNA is 33°. That is, a B-DNA helix turns 360° every 10 base pairs, while an A-DNA helix turns 360° every 11 base pairs. These structural differences result in the B-form Dickerson Dodecamer being about 1 nm longer along the axis, but narrower in diameter than the A-form.

When AMBER is used to simulate DNA molecules, the conversion from an A-form structure to a B-form structure usually occurs very rapidly, in the range of 100 to 1000 ps. [169] One easy and simple measure of the conversion is to plot the end-to-end length of

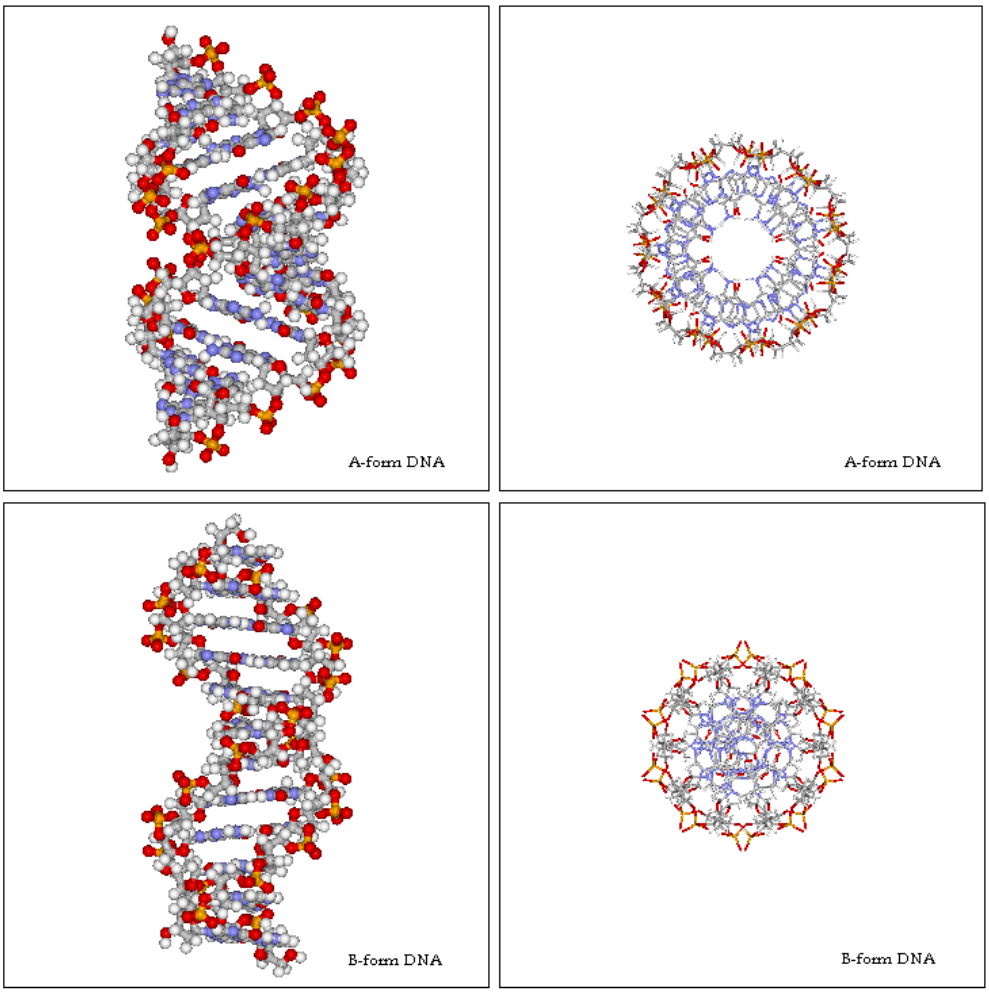

Figure 39: Comparison of structures of the A-form and B-form Dickerson dodecamer. Both the top-view and side-view are shown.

the DNA segment as a function of time. In Fig. 40 we show such a plot for the Dickerson dodecamer DNA. The simulation was started from an A-form DNA. We can see the length of the DNA segment stretched from about 2.8 nm to 3.8 nm in about 300 ps, which indicates the structure spontaneously transformed to the B-form. Note that the end-to-end length shown in Fig. 40 is measured between the centers of mass of the head and tail base pairs, not the full length of the DNA. The time scale over which the conversion occurred agrees with the reported range of 100 to 1000 ps. [169] The transformation of the structures during the dynamics can be seen from the snapshots taken during the simulations, as shown in Fig. 41. We can see that by 1000 ps, the original A-form structure of the DNA segment is completely stabilized into the B-form. (See Fig. 39 for comparison.) The disorder in the structure shown in the top view of Fig. 41 is due to the fluctuations of the DNA atoms.

7.5.2 The adsorption of the DNA segment on the SWNT in water

Based on the success of simulating the single Dickerson DNA in water, we performed simulations of a variety of DNA plus SWNT systems. The systems we studied include: (1) DNA with an uncharged SWNT in water; (2) DNA with a charged SWNT in water; (3) DNA with an uncharged SWNT, but from a modified starting configuration; (4) DNA with uncharged and charged SWNT, but with DNA starting from the A-form structure instead of the B-form structure. For charged SWNTs we studied three different situations. Firstly, we put a positive charge of $0.05e$ uniformly on each carbon atom of the SWNT. Secondly, we put $0.01e$ positive charge on each carbon atom. Thirdly, we applied negative charge of $-0.05e$ on each carbon atom. These charging schemes are based on previous experimental findings that electrons in SWNTs are spatially extended over the length of the tube. [201, 202] In (3) we started our simulations from a configuration of DNA axis perpendicular to the SWNT axis, instead of the parallel geometry as other systems studied.

From simulations we found that the DNA segment adsorbs onto the walls of the uncharged and positively charged SWNTs easily under the conditions we investigated. The initial contact between DNA and SWNT occurs very rapidly. In Fig. 42 we show the distance between the centers of mass of the DNA and the SWNT, d, as a function of time. It can

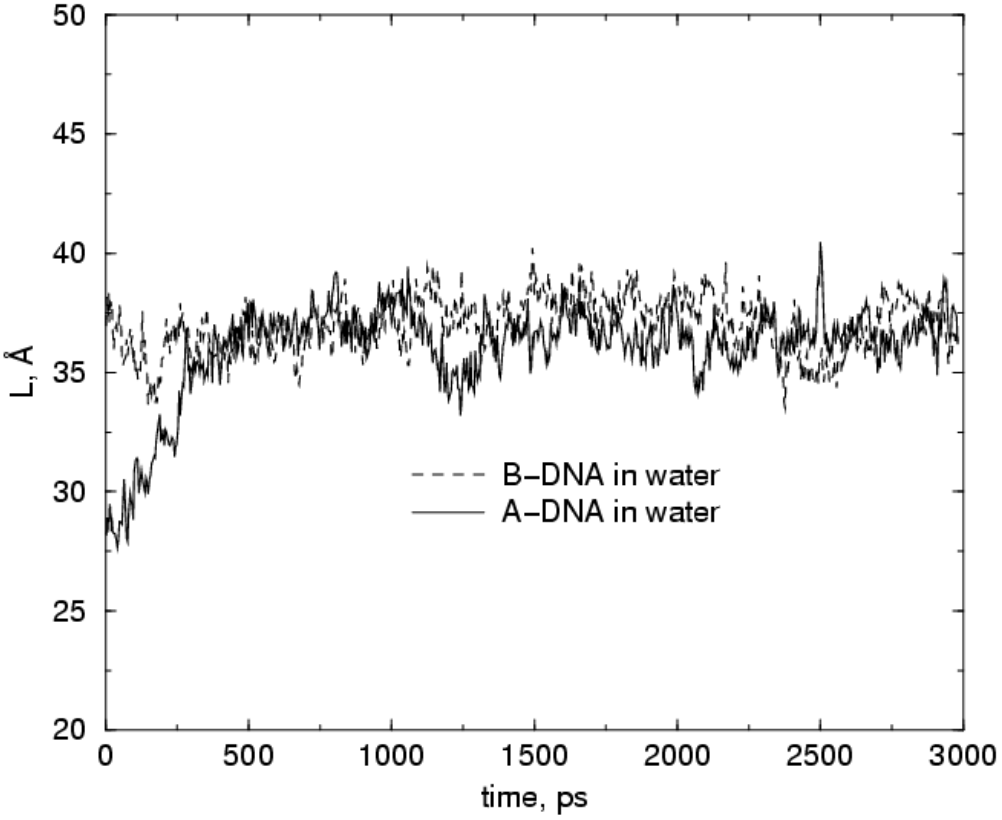

Figure 40: The end-to-end length (distance between the centers of mass of the head and tail base pairs) of the A-form and B-form Dickerson Dodecamers as a function of simulation time. The length of the A-form DNA (in solid curve) grows from about 2.8 nm to about 3.8 nm within 300 ps, which shows the conversion of the A-form to the B-form. For comparison, the end-to-end length of the B-form Dickerson Dodecamer as a function of time under the same simulation conditions is shown by the dashed curve.

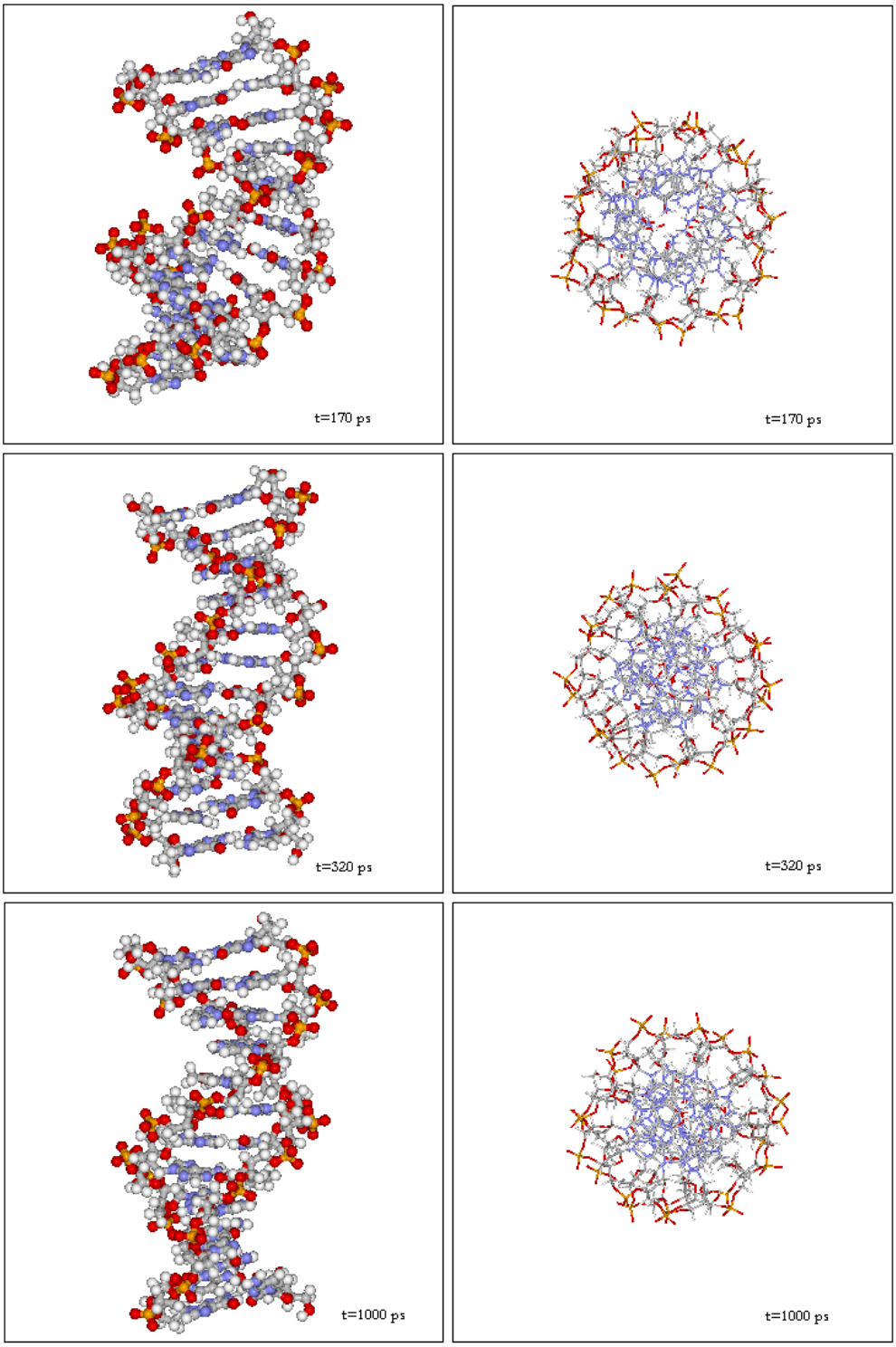

Figure 41: Snapshots taken during the molecular dynamics simulation show the A-form to B-form conversion of the DNA segment. Both top-view and side-view are shown.

be seen that d drops from the initial 20 Å to about 18 Å in about 20 ps and it continues to drop to about 17.5 Å within about 200 ps. After 200 ps, the adsorption patterns of DNA on uncharged SWNT and positively charged SWNT begin to vary. For DNA on the uncharged SWNT, one end of the DNA segment begins to drift away from the SWNT, with the other end bound to the SWNT wall. The overall effect is that the center of mass distance between the DNA and SWNT increases with time. This phenomena is illustrated in Fig. 43(b) and the snapshots in Fig. 44. As can be seen, at about $t = 100$ ps, both C1-G24 and G12-C13 ends of the DNA bind with the SWNT wall. After 200 ps, the C1-G24 end of the DNA desorbs from the SWNT as time evolves, while the G12-C13 end of the DNA binds to the SWNT in a relatively stable position. The middle part of the DNA, such as the T8-A17 base pair, is relatively quiescent up to 1800 ps, then begins to fluctuate slightly around its initial position due to the movement of the C1-G24 end.

However, for DNA on the positively charged SWNT, the situation is different. As can be seen in Fig. 42, when we put $0.05e$ positive charge on each carbon atom in the SWNT, the center of mass distance between the DNA and the SWNT is much more stabilized throughout the simulation. This is due to the fact that both the head and tail of the DNA binds to the wall of the SWNT and the partial desorption of the DNA segment from the SWNT is limited. Such binding can be inferred from the dynamics of the head, tail, and middle part of the DNA, as shown in Fig. 45. During the simulation, C1-G24, G12-C13, and T8-A17 base pairs all fluctuate around their initial positions. The amplitudes of the fluctuations are quite small compared with those of C1-G24 when the SWNT is not charged (see Fig. 43 for comparison). At about t=2000 ps and t=2500 ps, slight "rocking" of the head and tail groups on the SWNT wall was observed. "Rocking" refers to the originally adsorbed end of the DNA desorbs and the other originally unadsorbed end binds to the SWNT at the same time. Since the DNA has a net negative charge and we charge the SWNT positively, the enhanced stability of DNA on the charged SWNT is not surprising. The adsorption process is also shown in the snapshots in Fig. 46. When we reduce the positive charge on each carbon atom to $0.01e$, the adsorption pattern of the DNA is similar to the adsorption of the DNA on the $+0.05e$/C SWNT. As shown in Fig. 47(a), the center of mass distance between the DNA and SWNT is stabilized around 17.5 Å. However, movement of the DNA body is more active

than the movement of DNA on the $+0.05e$/C charged SWNT. This phenomena is illustrated in Fig. 47(c). The fluctuations of the three base pairs chosen to represent the head, tail, and the middle of the DNA are much more severe. The amplitudes of these fluctuations are between those of DNA on the uncharged SWNT and DNA on the $+0.05e$/C charged SWNT. The"rocking" of the head and tail groups was observed again. The larger amplitude of the "rocking" indicates that the binding between the DNA and the $+0.01e$/C charged SWNT is not as strong as that between the DNA and the $+0.05e$/C charged SWNT. Thus, we can decrease the stability of the adsorption of DNA on SWNT by decreasing the positive charge on the charged SWNT. The adsorption process of DNA on $+0.01e$/C charged SWNT is also shown in the snapshots in Fig. 46.

We have also performed simulations of DNA adsorption on the negatively charged SWNT. Each carbon atom was charged with $-0.05e$. As we expected, the negatively charged SWNT and DNA repel to each other and we did not observe adsorption over a time scale of 3 ns. This observation also suggests that we can desorb a DNA segment from a SWNT wall by applying negative charge to the SWNT. The simulation process is shown in Fig. 48.

We found that DNA and SWNT tend to have their axes tilted at an angle relative to each other rather than keeping their initial parallel configuration after the DNA adsorbs. This was seen for either DNA on the uncharged or positively charged SWNTs (see Figs. 43(a), 45(a), and 47(b)). It is not clear if a single stable configuration exists between DNA and SWNT when the adsorption occurs. We performed a simulation with the DNA and an uncharged SWNT starting from a new relative geometry in order to assess the stability of the relative configuration between the DNA and the SWNT. In this simulation, the axes of DNA and SWNT were initially perpendicular rather than parallel to each other.

Interestingly, we found that DNA on an uncharged SWNT do have a specific stable binding geometry that consists of on end of the DNA bound to the surface with the other end free (see Fig. 49 and snapshots in Fig. 44). In contrast, the angle between the DNA and SWNT axes does not appear to have a preferred value (see Fig. 43(a) and Fig. 49(b) for comparison). Furthermore, the ends and middle of the DNA are unbound and relatively free to move (see Fig. 43(b) and Fig. 49(c) for comparison). We did not observe binding between the middle of the DNA and the SWNT in either case. We noted that the middle

of a Dickerson dodecamer DNA is composed of A-T base pairs, while its ends are C-G base pairs. The DNA segment we used in the simulation is symmetric in sequence. Thus, the binding of either end onto the SWNT is possible. It is unclear why the binding seems to occur more favorably for the DNA ends than for the middle residues. Recent experimental work [203] suggested that the wrapping of SWNT by single-stranded DNA (ssDNA) to be sequence-dependent. We can not tell if sequence dependent binding occurs in our simulations.

7.5.3 The structure of adsorbed DNA

In the simulations we found that the adsorption process of DNA on SWNT did not affect the structure of the DNA segment significantly. This is true for both DNA on uncharged SWNT and DNA on charged SWNT. In Fig. 50(b)-(d) we show the center of mass distances between the DNA base pairs as a function of time. Here we give the averaged values of the distances between the 12 base pairs collected during the simulation, since the distances between different base pairs vary. For comparison, the corresponding values for DNA in water without SWNT is plotted in Fig. 50(a).

As can be seen, the average center of mass distance between the DNA base pairs is quite stable, either with or without a SWNT in the system. In Fig. 50(b) we show the situation when the DNA interacts with an uncharged SWNT; Fig. 50(c) is for DNA plus charged SWNT with $q = +0.05e$/C, and (d) represents the case when SWNT is charged with $+0.01e$/C. They all behave in the same way as in (a). Under all the situations, the average base pair distance of the DNA fluctuates around 11.7 Å. The magnitudes of the fluctuations at these different conditions are also similar to each other. This indicates that the interaction between the DNA and the SWNT is not strong enough to disrupt the binding between the DNA base pairs. We also calculated the rotation angle per base pair of DNA as a function of time, as shown in Fig. 51. For the stable B-form DNA, the rotation angle per residue is 36°. In Fig. 51, we give the averaged value of 11 rotation angles formed by 12 base pairs. It is clear that the adsorption process does not affect the rotation angle. The DNA rotation angle per residue fluctuates around 36° regardless of the presence of the SWNT.

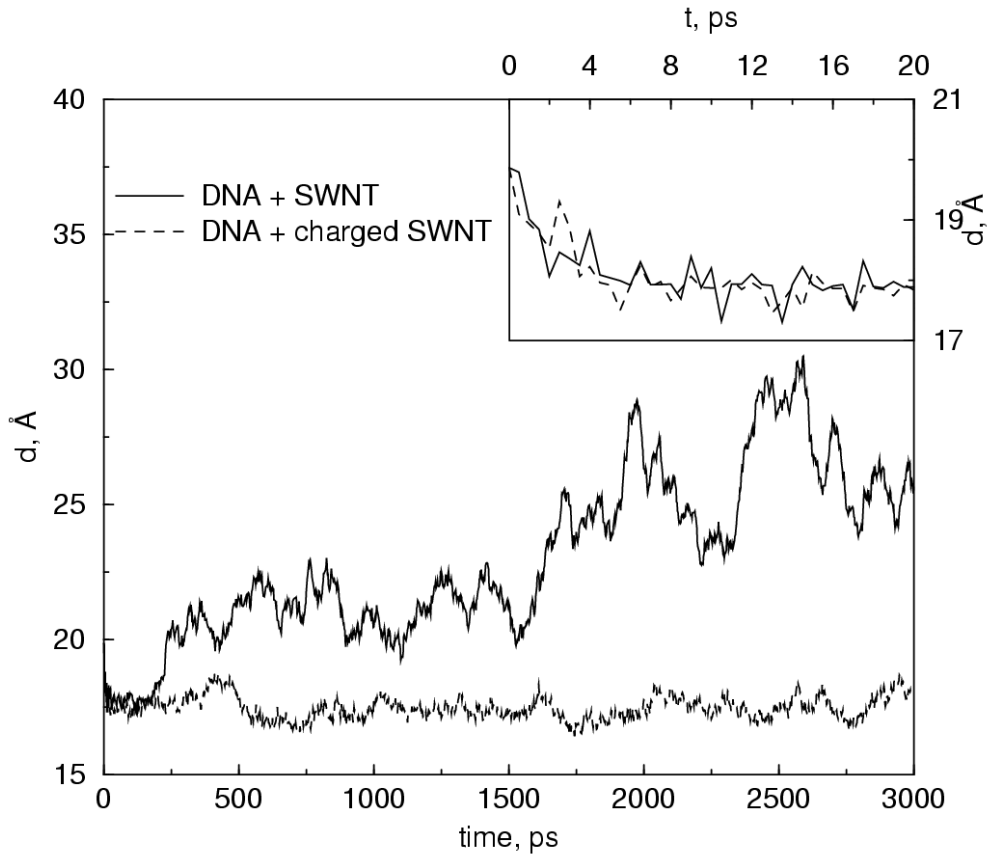

Figure 42: The distance between the centers of mass of the SWNT and DNA segment. The solid and dashed curves show the center of mass distance as a function of time between DNA and uncharged SWNT, and charged SWNT ($+0.05e$/C), respectively. The inset shows the initial 20 ps to give an indication of the time scale for the initial contact.

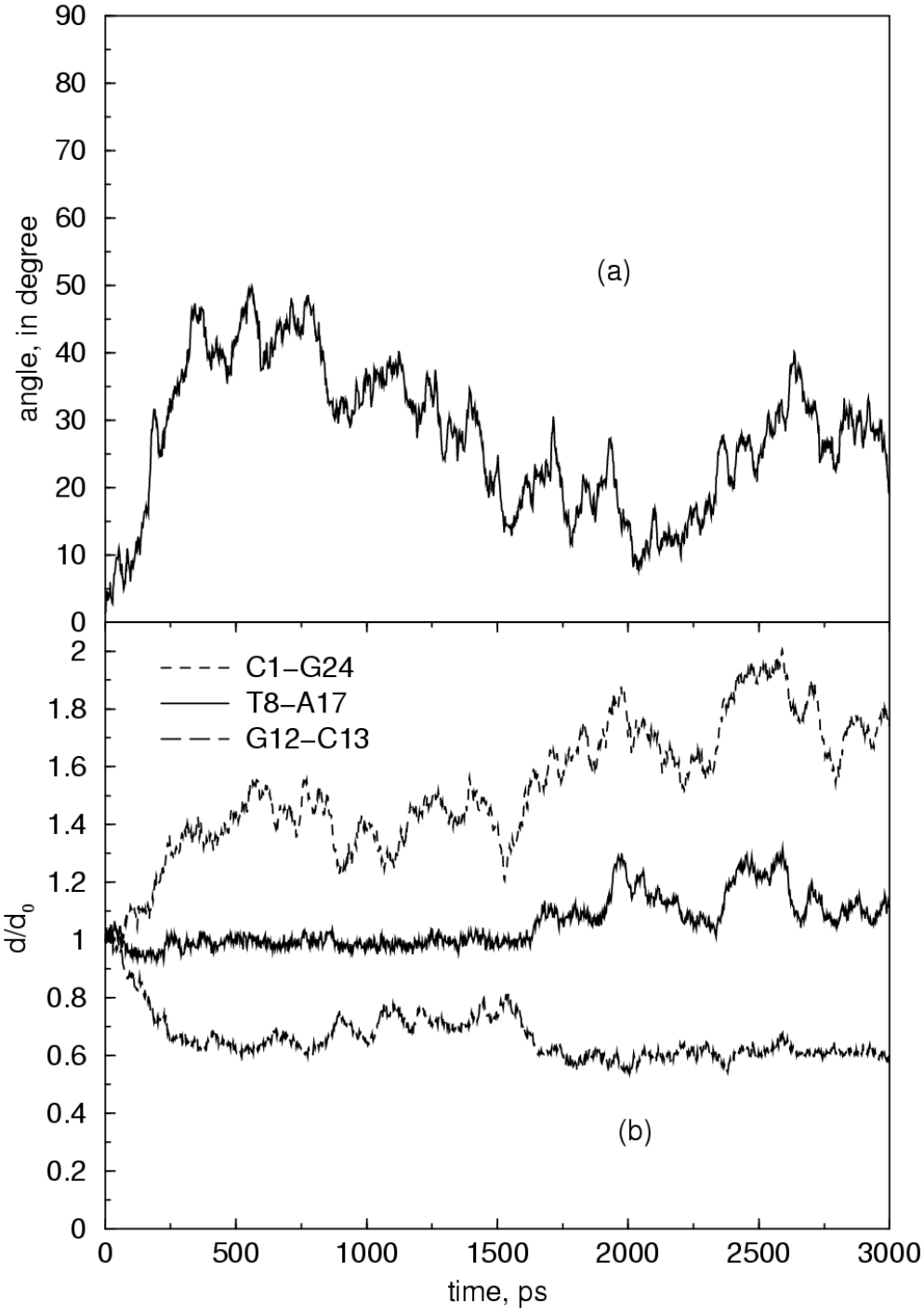

Figure 43: The adsorption of DNA on an uncharged SWNT: (a) The angle between the axes of the DNA and the SWNT; (b) The normalized distance between the centers of mass of the SWNT and the head, tail, and the middle part of the DNA.

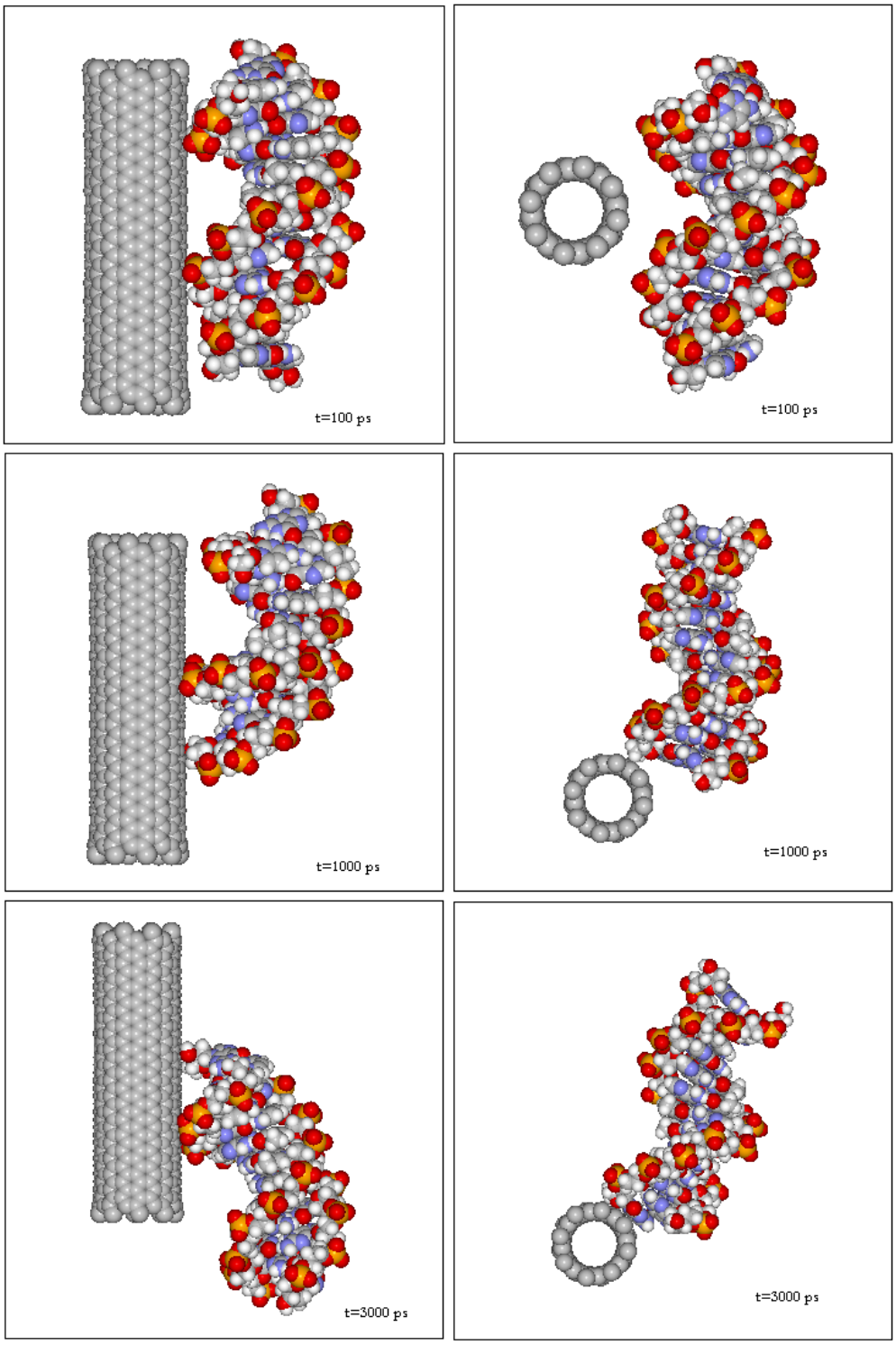

Figure 44: Snapshots taken during the simulations for DNA adsorption on uncharged SWNTs. The snapshots on the left hand side column show the adsorption of DNA on an uncharged SWNT, starting with the DNA and SWNT parallel to each other. The right hand side column is for an initial configuration with the axes of the SWNT and DNA perpendicular to one another.

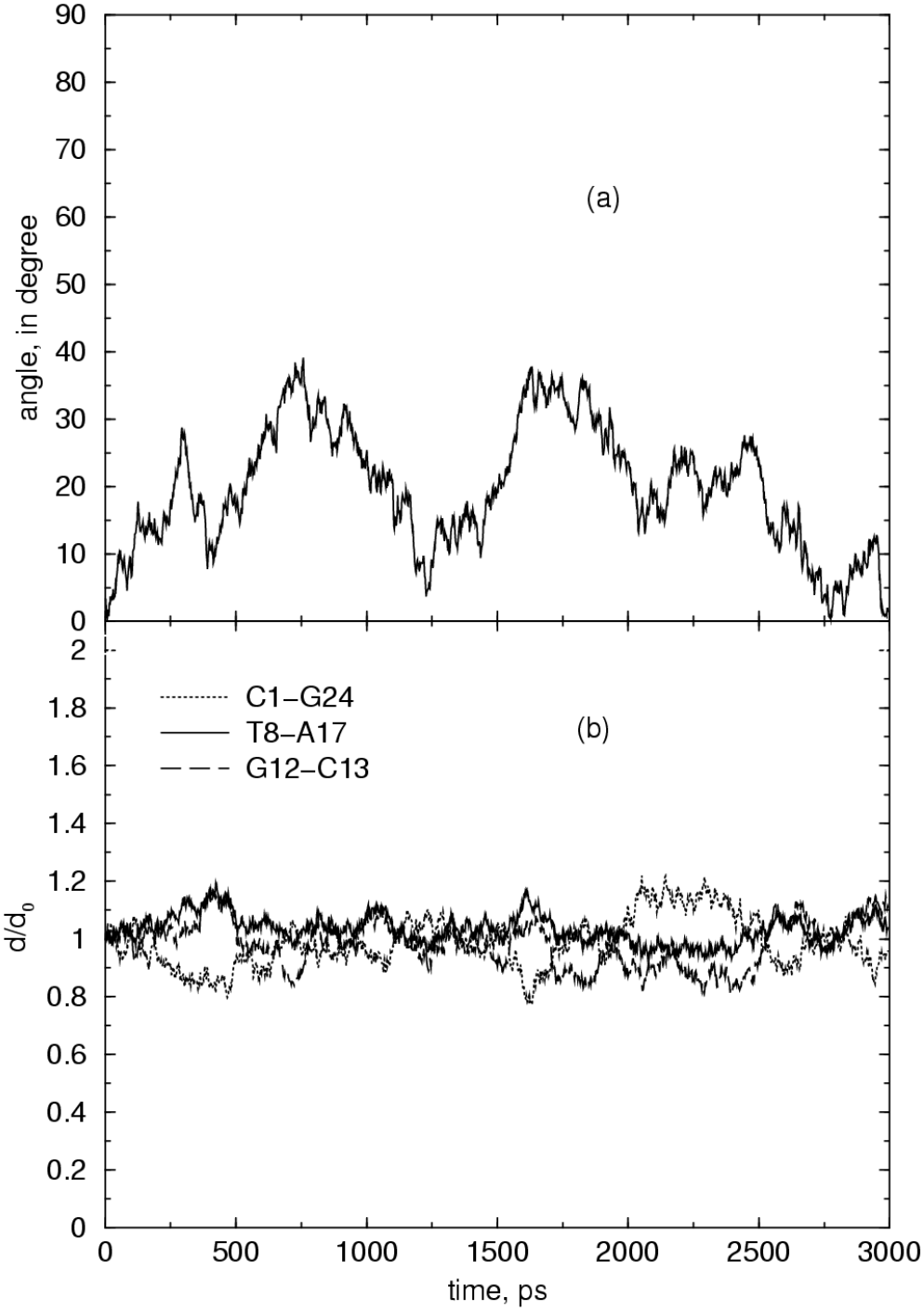

Figure 45: The adsorption of DNA on a positively charged SWNT. A charge of q=+0.05e/C was placed on the center of each carbon atom in the SWNT: (a) The angle between the axes of the DNA and the SWNT; (b) The normalized distance between the centers of mass of the SWNT and the head, tail, and the middle part of the DNA.

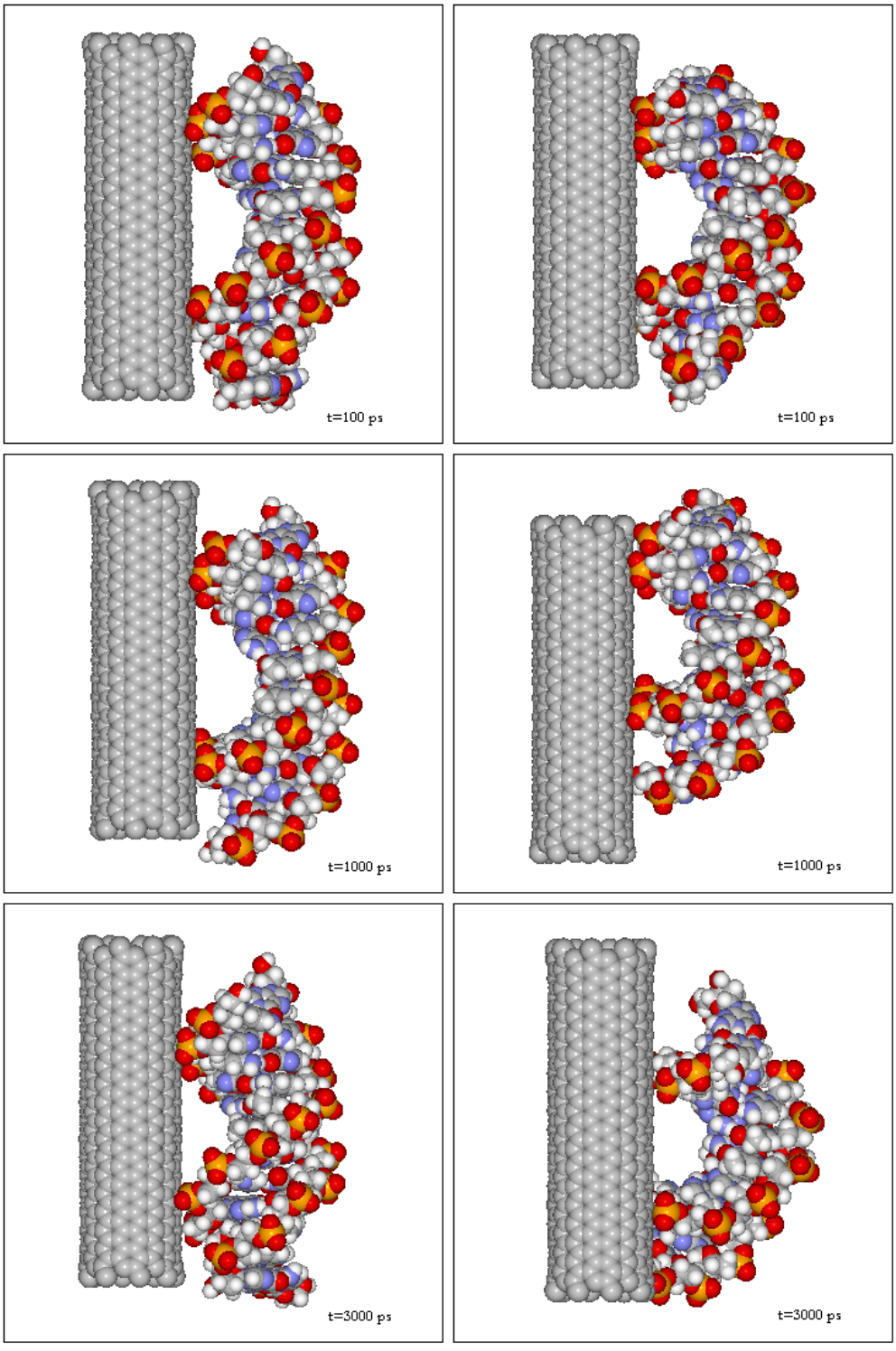

Figure 46: Snapshots taken during the simulations for DNA adsorption on charged SWNTs. The snapshots on the left hand side column are for a charge of $+0.05e$ per SWNT atom. The right hand column is for a charge of $+0.01e$ per SWNT atom.

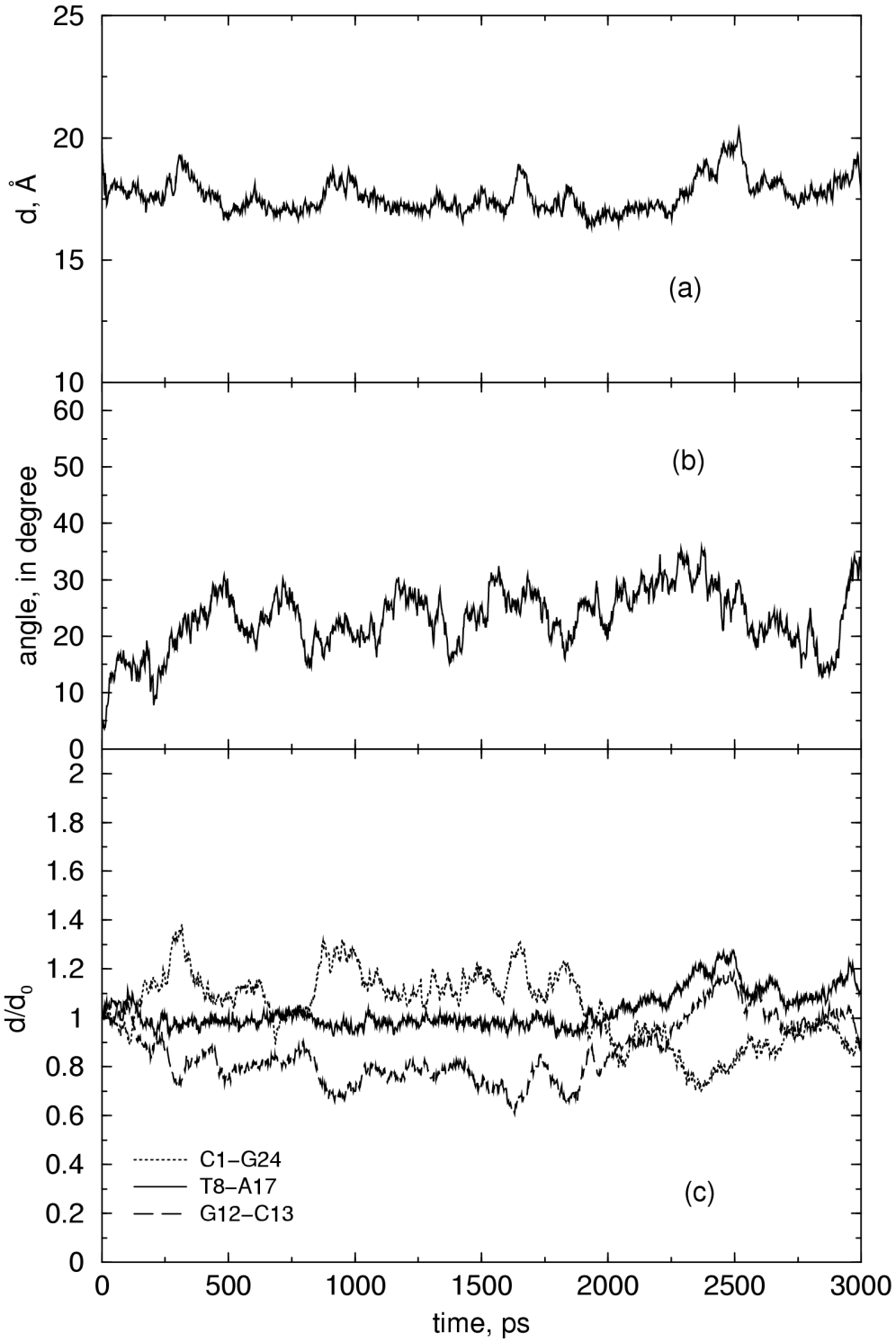

Figure 47: The adsorption of DNA on positively charged SWNT, A charge of q=+0.01e/C was placed on the center of each carbon atom in the SWNT: (a) The distance between the centers of mass of the DNA and the SWNT; (b) The angle between the axes of the DNA and the SWNT; (c) The normalized distance between the centers of mass of the SWNT and the head, tail, and the middle part of the DNA.

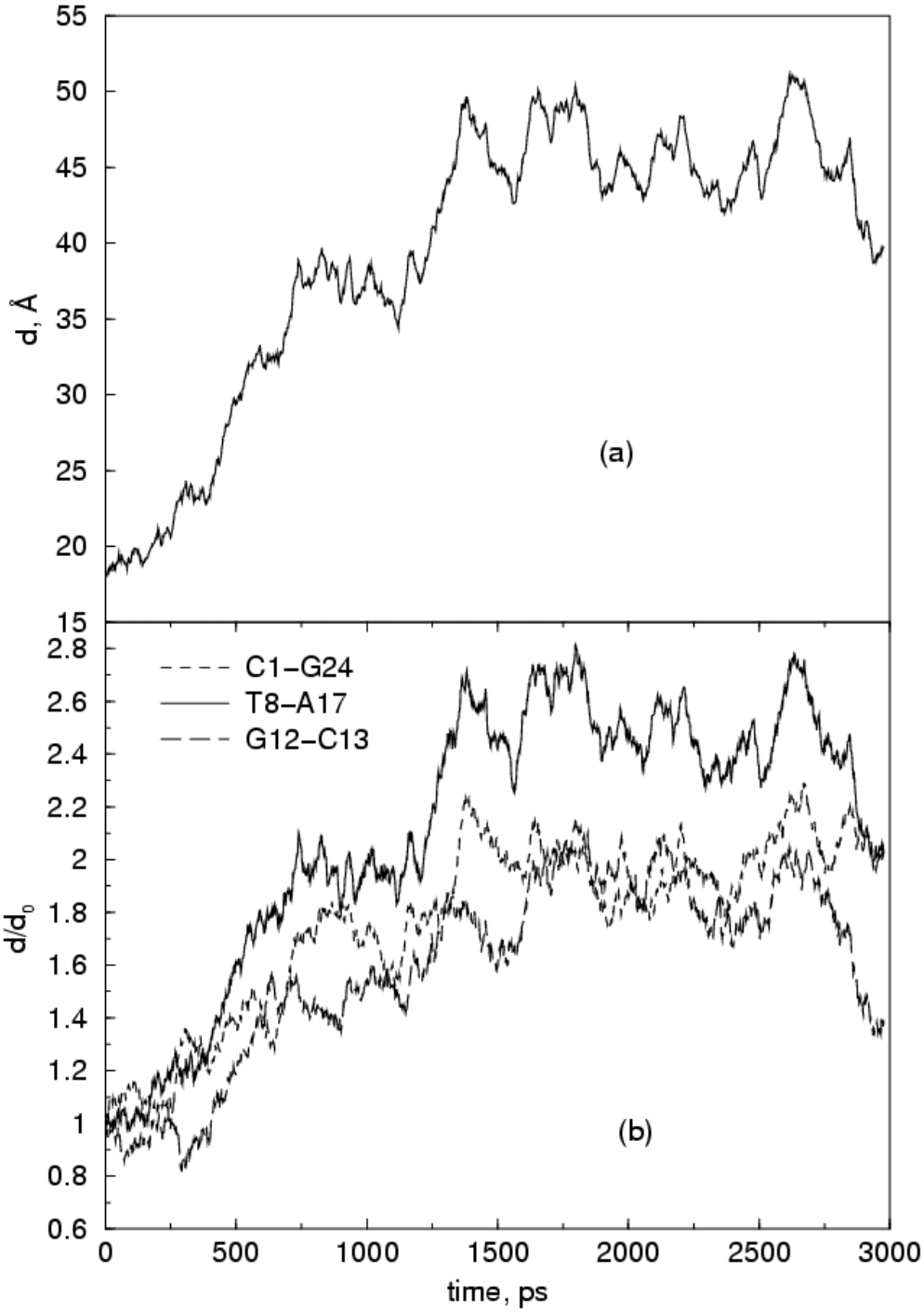

Figure 48: The simulation results of DNA on negatively charged SWNT. A charge of $q = -0.05e$/C was put on the center of each carbon atom in the SWNT: (a) The distance between the centers of mass of the DNA and the SWNT; (b) The normalized distance between the centers of mass of the SWNT and the head, tail, and the middle part of the DNA. No adsorption takes place because the DNA and SWNT repel on another.

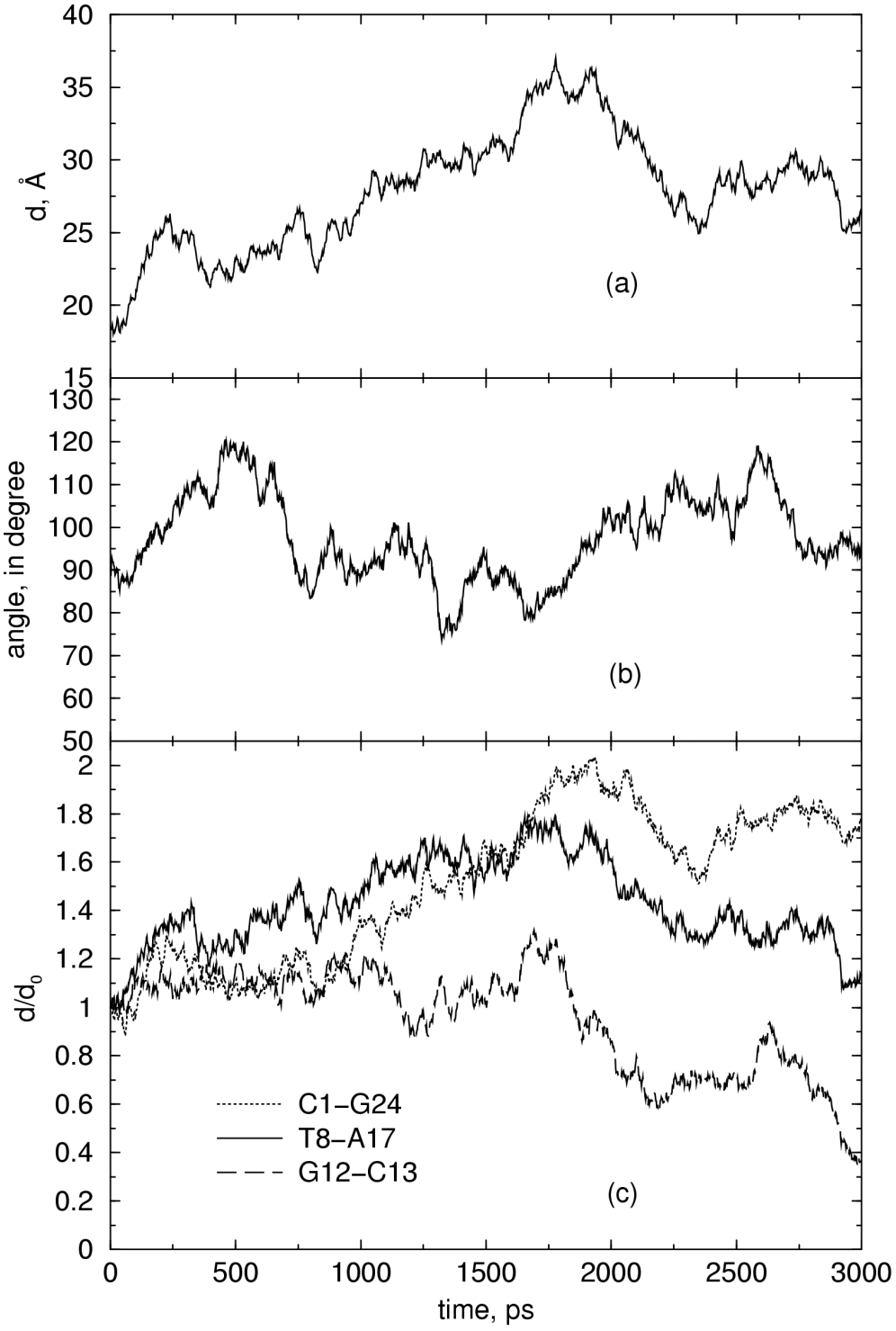

Figure 49: The adsorption of DNA on an uncharged SWNT. The DNA and SWNT axes were perpendicular to each other in the initial configuration. (a) The distance between the centers of mass of the DNA and the SWNT; (b) The angle between the axes of the DNA and the SWNT; (c) The normalized distance between the centers of mass of the SWNT and the head, tail, and the middle part of the DNA.

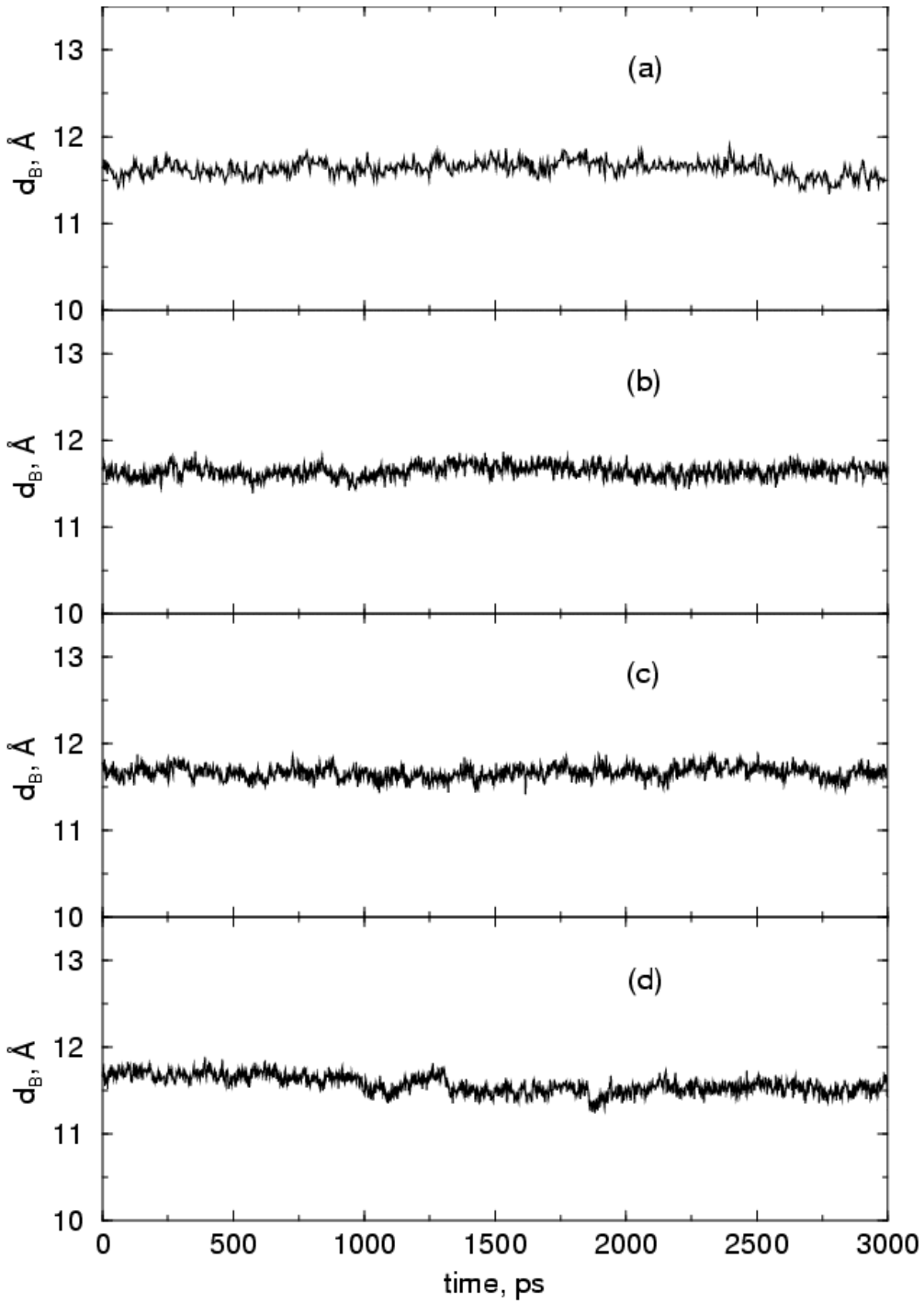

Figure 50: The average center of mass distance between base pairs of DNA segment in water. (a) DNA in water, without the presence of SWNT; (b) DNA with an uncharged SWNT in water; (c) DNA with positively charged SWNT in water, each carbon atom in SWNT was charged $+0.05e$/C; (d) DNA with positively charged SWNT in water, each carbon atom in the SWNT was charged $+0.01e$/C.

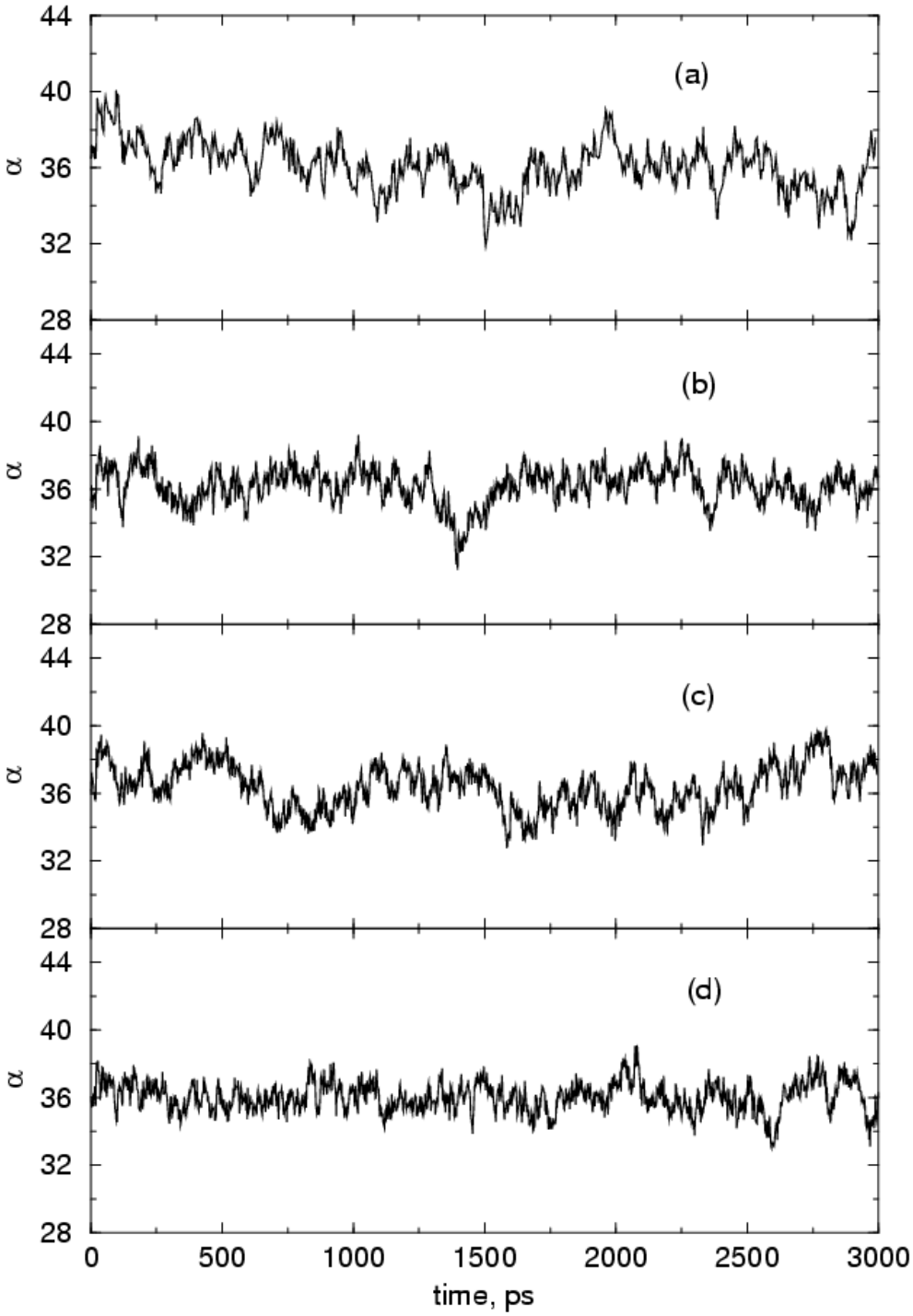

Figure 51: The average rotation angle per residue of the DNA strands. (a) DNA in water, without the presence of SWNT; (b) DNA with an uncharged SWNT in water; (c) DNA with positively charged SWNT in water, each carbon atom in the SWNT was charged $+0.05e$/C; (d) DNA with positively charged SWNT in water, each carbon atom in the SWNT was charged $+0.01e$/C.

7.5.4 The adsorption of the A-DNA on SWNTs

As we stated in a previous section, the A-DNA to B-DNA conversion was observed in a time scale of 300 ps if there is no SWNT present in water under the condition we studied. In this section we discuss how adsorption of DNA on to a SWNT affects the A-B transformation and conversely how the A-B transformation affects adsorption on to the SWNT.

The adsorption of DNA on to a SWNT appears to delay the A to B transformation of the DNA. In Fig. 52 we show the end-to-end distance of A-DNA as a function of time under three conditions: (a) A-DNA in water, without a SWNT; (b) A-DNA with an uncharged SWNT in water; (c) A-DNA with a $+0.05e$/C charged SWNT in water. Figure 52(a) was replotted from Fig. 40 for comparison.

Th end-to-end length did not completely relax from the A-DNA to the B-DNA value over 3 ns for A-DNA adsorbed on an uncharged SWNT (Fig. 52(b)). It appears that the complete A to B transition is either delayed or inhibited by the adsorption of A-DNA on to the uncharged SWNT.

Interestingly, A-DNA initially stretches to the B-DNA length at about 500 ps (Fig. 52(b)) but then quickly contracts and appears to stabilize around 3.1 nm. This length lies between that of A-DNA (2.8 nm) and B-DNA (3.8 nm). Although clear major and minor grooves had developed during the adsorption for the A-DNA (see the snapshots in Fig. 53), The incompletely stretched end-to-end length indicates that the A-B conversion was not completed within 3 ns. Longer simulations are needed to see if the A-DNA ultimately relaxes to the B-form beyond 3 ns.

The incomplete A-B form transformation observed in A-DNA/uncharged SWNT can be explained by the adsorption configuration difference between A-DNA/uncharged SWNT and B-DNA/uncharged SWNT. For the B-DNA adsorption on an uncharged SWNT, one end of the DNA binds with the SWNT and the other end unbound. No "rocking" was observed (see Fig. 43). On the other hand, when the A-DNA adsorbs on an uncharged SWNT, both ends of the A-DNA bind with the SWNT with very frequent "rocking" (see Fig. 54). The plane containing the end group base pairs is nearly parallel to the SWNT axis when the end group binds to the nanotube (see Fig. 53). Note that the end group planes for B-DNA are

parallel, while those for A-DNA are tilted toward one another (see Fig. 39). It is therefore easier for A-DNA to have both end groups bind to the SWNT since less bending is required compared with B-DNA. So the adsorption of A-DNA on an uncharged SWNT inhibits the A-B conversion.

We have simulated the adsorption of A-DNA on a $+0.05e$/C charged SWNT. The adsorption process of A-DNA on the charged nanotube is very different from A-DNA adsorption on the uncharged nanotube. The middle section of A-DNA binds more closely to the surface of the SWNT than either of the end groups. This can clearly be seen in Fig. 55(c) which shows that the T8-A17 (middle) section of A-DNA is closer to the SWNT than either of the two end groups. Comparison of Fig. 55(c) with Figs. 43(b), 45(b), 47(c), 49(c), and 54(b) shows that the only system for which T8-A17 binds more closely to the SWNT than either of the end groups is A-DNA on the $+0.05e$/C charged SWNT. The binding of the middle segments can also be observed from the molecular snapshot at a time of 500 ps in Fig. 53.

Another interesting feature of A-DNA on the $+0.05e$/C charged SWNT is that the end-to-end relaxation to the B-DNA form happens remarkably quickly; only about 250 ps is required for the relaxation to occur (see Fig. 52(c)). Note from Fig. 55(c) that time for T8-A17 to adsorb onto the SWNT surface is about the same as that required for the end-to-end distance to relax from the initial 2.8 nm to the B-DNA value of 3.8 nm. We presume that adsorption of the T8-A17 segment to the SWNT facilitates the A-B transformation by allowing the ends to move freely. This is in stark contrast to the case for A-DNA adsorbed on the uncharged SWNT, where binding of both end groups to the nanotube inhibits the A-B transition.

Once the A-B transition is complete for A-DNA on the $+0.05e$/C nanotube, the middle segment desorbs from the SWNT surface while the end groups migrate toward the nanotube surface. After 4 ns the ending geometry is very similar to that observed for B-DNA on the $+0.05e$/C nanotube (compare Figs. 46 at 3 ns and 53 at 4 ns). This is expected because after the A-B transition the two systems must relax to the same equilibrium state.

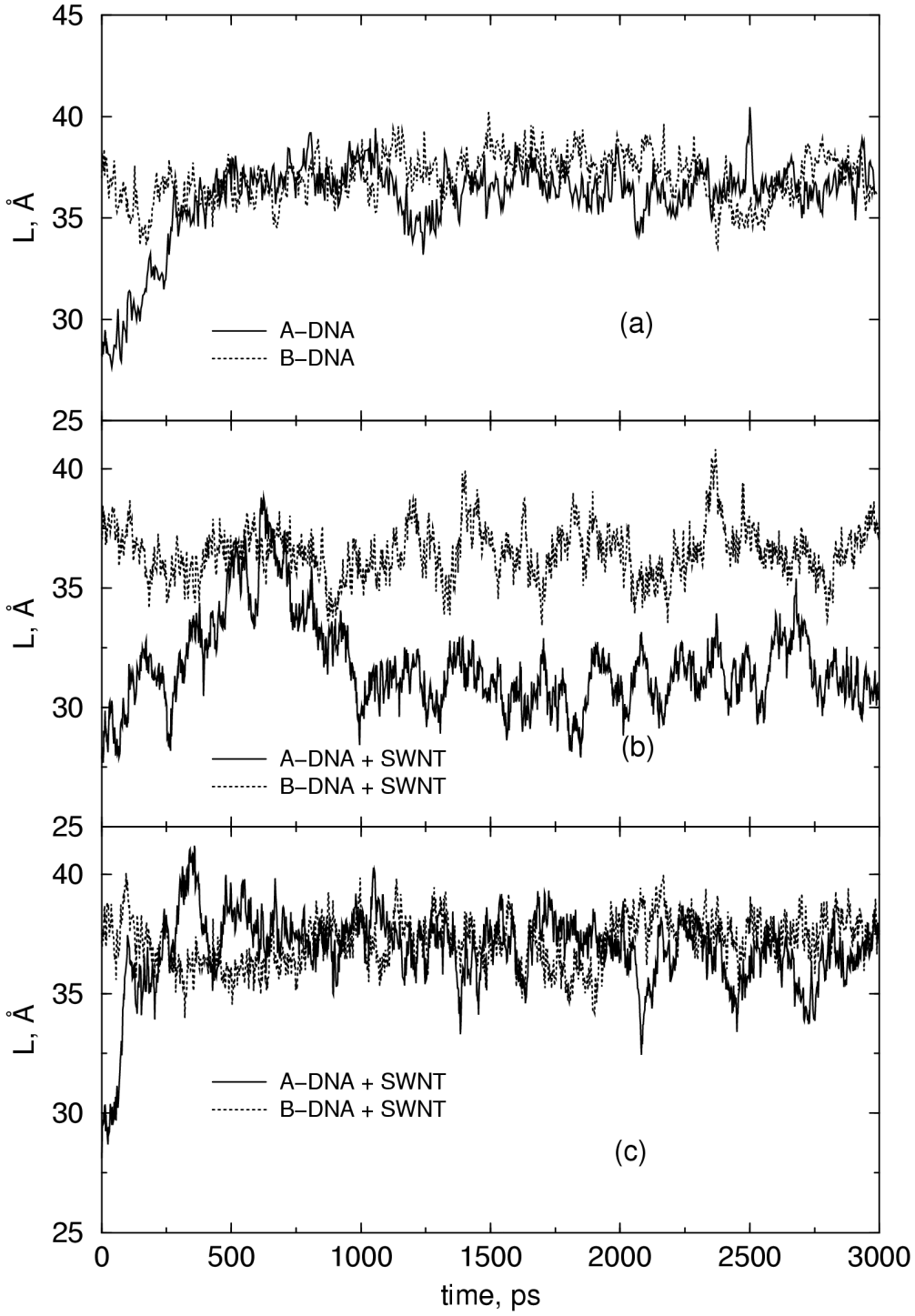

Figure 52: The end-to-end distance of A-DNA when it adsorbs on to a SWNT. The solid curves represent the end-to-end distance of A-DNA, the dotted curves gives the end-to-end distance of B-DNA under the same conditions. (a) The conversion of A-DNA to B-DNA, without the presence of a SWNT; (b) DNAs with an uncharged SWNT in water; (c) DNAs with $+0.05e$/C charged SWNT in water.

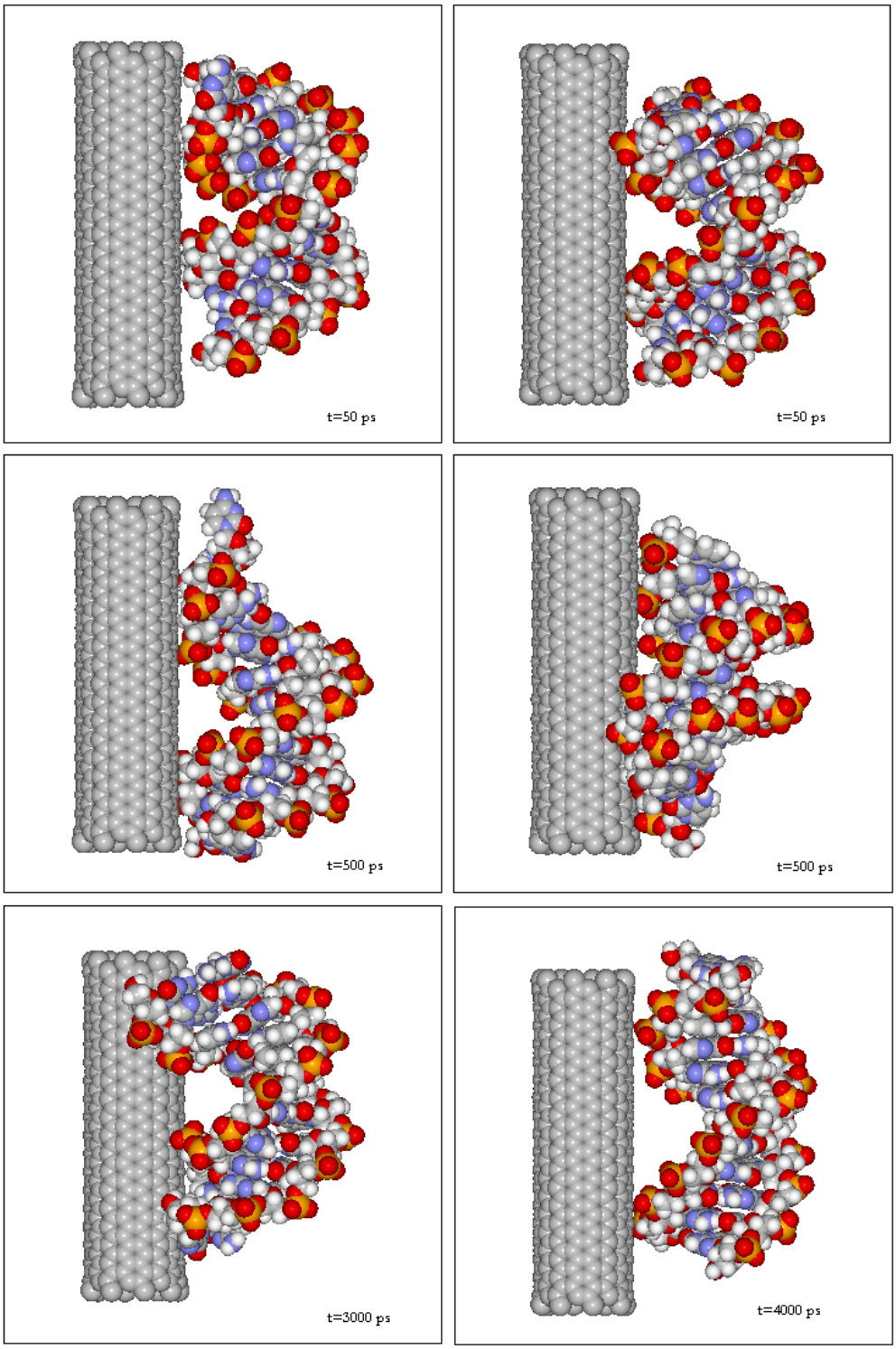

Figure 53: Snapshots taken during the simulations for A-DNA adsorption on uncharged and positively charged SWNTs. The snapshots on the left hand side column show the adsorption of the A-DNA on an uncharged SWNT. The right hand side column shows the adsorption of the A-DNA on positively charged SWNT, $q = +0.05e/\mathrm{C}$.

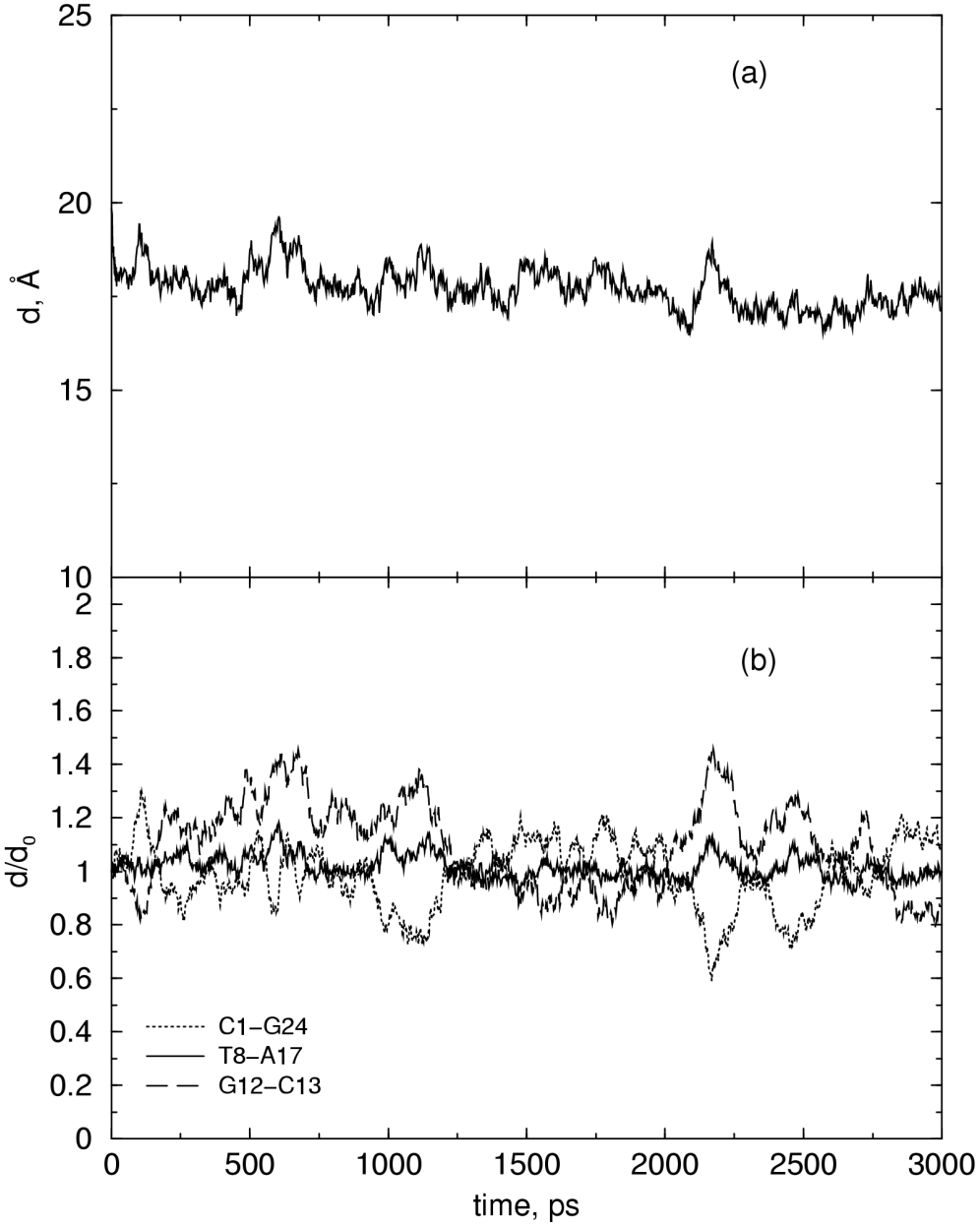

Figure 54: The adsorption of the A-DNA on an uncharged SWNT: (a) The distance between the centers of mass of the A-DNA and the SWNT; (b) The normalized distance between the centers of mass of the SWNT and the head, tail, and the middle part of the A-DNA.

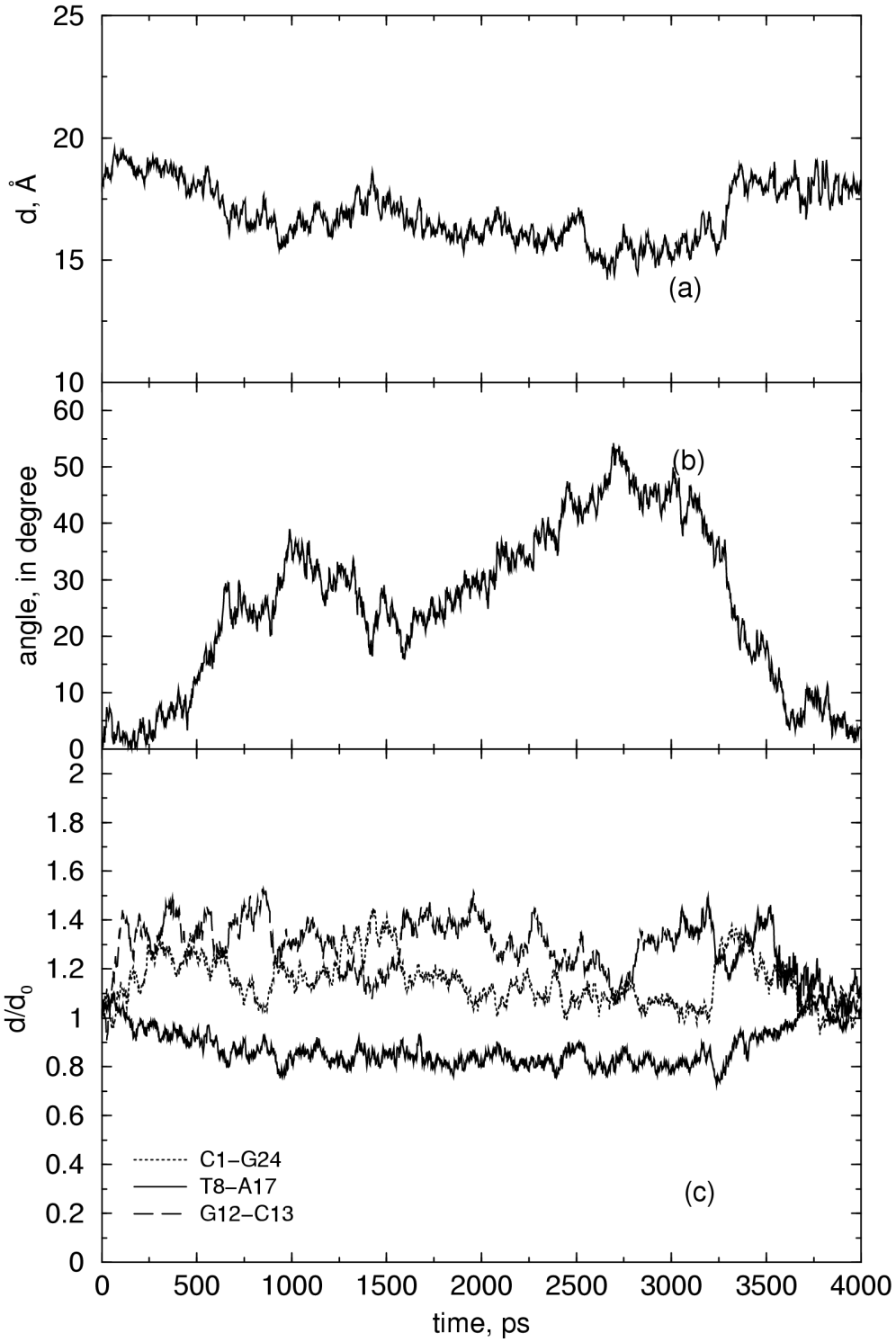

Figure 55: The adsorption of A-DNA on a positively charged SWNT, q=+0.05e/C: (a) The distance between the centers of mass of the A-DNA and the SWNT; (b) The angle between the axes of the A-DNA and the SWNT; (c) The normalized distance between the centers of mass of the SWNT and the head, tail, and the middle part of the A-DNA.

7.6 CONCLUSION

We have performed molecular dynamics simulations of a Dickerson Dodecamer DNA segment interacting with SWNTs in aqueous solution. The simulation results show that the end groups of a DNA segment adsorb onto the uncharged and positively charged SWNT on a time scale of a few hundred picoseconds. DNA molecules bind with one end onto an uncharged SWNT wall. When the SWNT is charged positively, both head and tail groups of the DNA bind with the SWNT wall. The adsorption process has a negligible effect on the structure of the DNA segment. The average base pair distance and the rotation angle per residue are not changed when the DNA adsorbs onto the uncharged or positively charged SWNT. However, the adsorption process affects the A to B conversion of A-DNA. The adsorption of the A-DNA onto an uncharged SWNT inhibits the complete relaxation of A-DNA to B-DNA over a time scale of 3 ns due to the binding of the A-DNA ends to the SWNT wall. In contrast, the adsorption of A-DNA on to a positively charged SWNT appears to promote the A to B conversion. This is accomplished by the middle section of DNA adsorbing to the SWNT, followed by slow relaxation to the B-DNA/charged SWNT binding geometry. The DNA segment does not adsorb onto a negatively charged SWNT and is repelled, as expected.

8.0 FUTURE WORK

8.1 LONGER SIMULATIONS AND LARGER SYSTEM SIZES

In our study of DNA segments adsorption on a SWNT, we chose to run all the simulations for a length of about three nanoseconds. Three nanosecond simulation is accepted as a routine time scale for studying DNA segments in an aqueous environment, although simulations up to ten nanoseconds had been performed. [170] For study of DNA/SWNT systems, a three nanosecond time scale simulation may not be long enough. This may be especially true for the DNA/SWNT systems involving DNA form transformations.

A longer simulation is needed to see if the adsorption of an A-DNA on to an uncharged SWNT can completely inhibit the A-B form conversion. From the current study we conclude that the A-B transformation does not occur within three nanoseconds due to the adsorption of both end groups. However, much longer molecular dynamics simulations will be needed in order to investigate if the state we observed at three nanoseconds is the final stable state. Longer simulations would also help to clarify the question if the adsorption mechanism is dependent on the starting geometry of the SWNT and the DNA segment. We see that the DNA segment does tend to bind with one end group to an uncharged SWNT. However, we did not observe quantitatively reproducible binding geometry the SWNT and the DNA would take when we start the simulation from different configurations (see Fig. 44). To study this issue, longer simulations are necessary. In this work, the distance between the SWNT/DNA centers of mass is about 2.0 nm initially. Will DNA readily adsorb if the initial separation is significantly larger? Another question is if the binding behavior of the DNA is affected by the finite size of the SWNT used in this study. Simulations with larger system sizes (further DNA/SWNT separation or longer SWNT) are needed to answer these questions.

8.2 STUDY WITH DIFFERENT DNA SEGMENT

In this study we used a 12-mer Dickerson DNA segment. As stated in the previous chapter, this DNA segment is symmetric in sequence. The ends of the Dickerson DNA are G-C groups, and middle is composed of A-T groups. We found that the DNA end groups bind more stably with the SWNT than the middle groups do. What is the reason behind this phenomena? Is it possible that different bases bind on to the SWNT with different stability? Or is it due to the structural difference of A-T and G-C base pairs? Why does A-T groups adsorb to $+0.05e$/C SWNT for the A-DNA form, but not for the B-DNA form? All these questions are still open. To answer these questions, we need to perform simulations of SWNT and DNA composed of various bases and base pairs.

Another interesting study is the simulation of SWNT and single stranded DNA. Recent experimental studies show that a single strand of DNA segment can wrap on to carbon nanotubes to create a 'coat'. [182] The phenomena was used to separate nanotubes of different diameters. It is found that the separation works well only for one specific type of single stranded DNA, $(GT)_n$. A possible mechanism was proposed by the experimentalists to explain this observation. The procedures developed in this work can be easily used to explore the theory behind the experimental results.

8.3 THE DYNAMICS OF THE SWNT

In this study the SWNT is held fixed in all the simulations by applying a force constant of 500 kcal/mol/Å^2 on each SWNT atom. By doing so we are assuming the adsorption of the DNA segment on to the SWNT does not affect the structure of the SWNT. We need to perform simulations including the vibrations of the SWNT atoms in order to test this assumption. The simulations considering the dynamics of the SWNT can be carried out by relaxing the force constant on each SWNT atom gradually during the equilibration.

APPENDIX

SAMPLE INPUT FILES FOR AMBER USED IN THIS WORK

A.1 GENERATE THE DICKERSON DODECAMER DNA

Input file for `nucgen` to generate a Dickerson Dodecamer DNA, `nuc.in`

```
  NUC   1
D
C5   G    C    G    A    A    T    T    C    G    C    G3

  NUC   2
D
C5   G    C    G    A    A    T    T    C    G    C    G3

END
$ABDNA
```

The command is

```
%nucgen -O -i nuc.in
           -o nuc.out
           -d $AMBERHOME/dat/leap/parm/nucgen.dat
           -p Dickerson.pdb
```

Please note the format in `nuc.in` file. There are 24 base residues needed to be specified in the file. The residues in upper line are numbered as 1 to 12, those in lower line are numbered as 13 to 24. Residue 1 pairs to residue 24, 2 to 23, 3 to 22, ..., 12 to 13 etc. The last line is the control for A-form or B-form DNA. Using either `ADNA` or `ABDNA` gives a B-form DNA, using `ADNA` gives an A-form DNA.

A.2 RELAX THE HYDROGEN ATOMS IN DNA

Input file for `sander` to relax the hydrogen atoms in the Dickerson Dodecamer DNA, `fixit.in`

```
dickerson dodecamer: minimization to fix up hydrogen positions
 &cntrl
  imin   = 1,
  maxcyc = 5000,
  ncyc   = 2500,
  ntr    = 1,
  ntb    = 0,
  igb    = 0,
 &end
Restrain the DNA heavy atoms I
5000.0
FIND
 *  CT  *  *
 *  C   *  *
 *  CA  *  *
 *  CB  *  *
 *  CK  *  *
 *  CQ  *  *
 *  CM  *  *
 *  OH  *  *
 *  OS  *  *
SEARCH
RES 1  24
END
Restrain the DNA heavy atoms II
5000.0
FIND
```

```
 *  O2  *  *
 *  O   *  *
 *  NA  *  *
 *  N*  *  *
 *  N2  *  *
 *  NC  *  *
 *  NB  *  *
 *  P   *  *
SEARCH
RES 1  24
END
END
```

Note: There are two groups of restraint declarations because one group can only support at most ten atoms to be restrained.

The command is

```
%sander -O -i fixit.in
           -o fixit.out
           -c Dickerson.inpcrd
           -p Dickerson.prmtop
           -r fixit.restart
           -ref Dickerson.inpcrd
```

A.3 INITIAL ENERGY MINIMIZATION HOLDING THE DNA AND SWNT FIXED

Input file for `sander` to minimize the energy initially holding all the solutes fixed, `min_ntr.in`

```
Initial minimization w/ position restraints on DNA_SWNT, 9.0 cut
 &cntrl
  ntx    = 1,       irest  = 0,       ntrx   = 1,      ntxo   = 1,
  ntpr   = 10,      ntwx   = 0,       ntwv   = 0,      ntwe   = 0,

  ntf    = 1,       ntb    = 1,
  cut    = 9.0,     nsnb   = 10,

  ibelly = 0,       ntr    = 1,

  imin   = 1,
  maxcyc = 2000,
  ncyc   = 5000,
  ntmin  = 1,       dx0    = 0.1,     dxm    = 0.5,     drms   = 0.0001,

  nscm   = 0,
  t      = 0.0,     dt     = 0.002,

  temp0  = 300.0,   tempi  = 300.0,
  ig     = 71277,   heat   = 0.0,
  ntt    = 0,
  tautp  = 0.2,
  vlimit = 20.0,

  ntc    = 1,       tol    = 0.0005,
```

```
 &end
Hold the DNA and SWNT fixed
500.0
RES  1  25
END
END
```

Note: Residues 1 to 25 represent DNA and SWNT, the rest of the residues are water molecules and free to move.

The command is

```
%sander -O -i min_ntr.in
           -o min_ntr.out
           -c DNA_SWNT_fixit.inpcrd
           -p DNA_SWNT_fixit.prmtop
           -r DNA_SWNT_min_ntr.restart
           -ref DNA_SWNT_fixit.inpcrd
```

A.4 INITIAL MOLECULAR DYNAMICS HOLDING THE DNA AND SWNT FIXED

Input file for `sander` to run initial molecular dynamics holding all the solutes fixed, `md_ntr.in`

```
Initial dynamics with DNA and SWNT fixed, 9.0 cut
 &cntrl

  nmropt = 1,
  ntx    = 1,       irest  = 0,       ntrx   = 1,      ntxo   = 1,
  ntpr   = 100,     ntwx   = 500,     ntwv   = 0,      ntwe   = 0,

  ntf    = 2,       ntb    = 2,
  cut    = 9.0,     nsnb   = 10,

  ibelly = 0,       ntr    = 1,

  imin   = 0,
  nstlim = 12500,
  nscm   = 0,
  t      = 0.0,     dt     = 0.002,

  temp0  = 300.0,   tempi  = 100.0,
  ig     = 71277,   heat   = 0.0,
  ntt    = 1,
  tautp  = 0.2,
  vlimit = 15.0,
  ntp    = 1,       pres0  = 1.0,     comp   = 44.6,
  taup   = 0.2,     npscal = 1,

  ntc    = 2,       tol    = 0.00001,
```

```
 &end
 &wt
   type='TEMP0', istep1=0,     istep2=500,
                 value1=100.0,  value2=300.0,
 &end
 &wt
   type='TEMP0', istep1=500,   istep2=12500,
                 value1=300.0, value2=300.0,
 &end
 &wt
   type='END',
 &end
 &rst
   iat=0,
 &end
Hold the DNA fixed
500.0
RES  1  25
END
END
```

Note: MD starts from T=100 K, in first 500 steps temperature is ramped from 100 K to the desired 300 K.

The command is

```
%sander -O -i md_ntr.in
           -o md_ntr.out
           -c DNA_SWNT_min_ntr.restart
           -p DNA_SWNT_fixit.prmtop
           -r DNA_SWNT_md_ntr.restart
```

```
-ref DNA_SWNT_min_ntr.restart
```

A.5 INITIAL MOLECULAR DYNAMICS WITH EWALD SUMMATION

Input file for `sander` to run initial molecular dynamics holding all the solutes fixed and turn on the Ewald summation, `md_ew_ntr.in`

```
initial dynamics fixing DNA/SWNT, 9.0 cut
 &cntrl

  ntx    = 1,       irest  = 0,       ntrx   = 1,      ntxo   = 1,
  ntpr   = 100,     ntwx   = 500,     ntwv   = 0,      ntwe   = 0,
  ntwprt = 0,

  ntf    = 2,       ntb    = 2,       dielc  = 1.0,
  cut    = 9.0,     nsnb   = 10,

  ibelly = 0,       ntr    = 1,

  imin   = 0,

  nstlim = 12500,
  nscm   = 0,
  t      = 0.0,     dt     = 0.002,

  temp0  = 300.0,   tempi  = 100.0,
  ig     = 71277,   heat   = 0.0,
  ntt    = 1,
  tautp  = 0.2,
  vlimit = 20.0,

  ntp    = 1,       pres0  = 1.0,     comp   = 44.6,
  taup   = 0.2,     npscal = 1,
```

```
  ntc    = 2,       tol    = 0.00001,

 &end
Allowing only the water to move
500.0
RES  1  25
END
END
```

Note: When the NMR optimization and temperature ramping is turned off, Particle Mesh Ewald summation is turn on.

The command is

```
%sander -O -i md_ew_ntr.in
           -o md_ew_ntr.out
           -c DNA_SWNT_md_ntr.restart
           -p DNA_SWNT_fixit.prmtop
           -r DNA_SWNT_md_ew_ntr.restart
           -ref DNA_SWNT_md_ntr.restart
```

A.6 MOVING DNA AND SWNT FIXED: ENERGY MINIMIZATION 1

Input file for `sander` energy minimization, relaxing DNA to a restrain of 25.0 kcal/mol/Å^2 while holding SWNT fixed, `equil_min1.in`

```
equil step 1, DNA relaxed to 25.0, SWNT fixed
 &cntrl

  ntx    = 1,       irest  = 0,       ntrx   = 1,      ntxo   = 1,
  ntpr   = 500,     ntwx   = 0,       ntwv   = 0,      ntwe   = 0,

  ntf    = 1,       ntb    = 1,
  cut    = 9.0,     nsnb   = 10,

  ibelly = 0,       ntr    = 1,

  imin   = 1,
  maxcyc = 2000,
  ncyc   = 5000,
  ntmin  = 1,       dx0    = 0.1,     dxm    = 0.5,     drms   = 0.0001,

  ntc    = 1,       tol    = 0.0005,

 &end
Constraints on DNA
25.0
RES 1  24
END
Constraints on SWNT
500.0
RES 25
```

```
END
END
```

The command is

```
%sander -O -i equil_min1.in
           -o equil_min1.out
           -c DNA_SWNT_md_ew_ntr.restart
           -p DNA_SWNT_fixit.prmtop
           -r DNA_SWNT_equil_min1.restart
           -ref DNA_SWNT_md_ew_ntr.restart
```

A.7 MOVING DNA AND SWNT FIXED: MD 1

Input file for `sander` MD, relaxing DNA to a restrain of 25.0 kcal/mol/Å^2 while holding SWNT fixed, `equil_md1.in`

```
equil step 1
 &cntrl

  ntx    = 1,       irest  = 0,       ntrx   = 1,      ntxo   = 1,
  ntpr   = 500,     ntwx   = 0,       ntwv   = 0,      ntwe   = 0,

  ntf    = 2,       ntb    = 2,
  cut    = 9.0,     nsnb   = 10,

  ibelly = 0,       ntr    = 1,

  nstlim = 1500,
  nscm   = 0,
  t      = 0.0,     dt     = 0.002,

  temp0  = 300.0,   tempi  = 300.0,
  ig     = 71277,   heat   = 0.0,
  ntt    = 1,
  tautp  = 0.2,
  vlimit = 20.0,

  ntp    = 1,       pres0  = 1.0,     comp   = 44.6,
  taup   = 0.2,     npscal = 1,

  ntc    = 2,       tol    = 0.00005,
```

```
 &end
Constraints on DNA
25.0
RES  1  24
END
Constraints on SWNT
500.0
RES 25
END
END
```

The command is

```
%sander -O -i equil_md1.in
           -o equil_md1.out
           -c DNA_SWNT_equil_min1.restart
           -p DNA_SWNT_fixit.prmtop
           -r DNA_SWNT_equil_md1.restart
           -ref DNA_SWNT_equil_min1.restart
```

A.8 FIVE ROUNDS OF STEP ENERGY MINIMIZATION

One of the input files for `sander` to run five rounds of step energy minimization, reducing the positional restraints to DNA by 5.0 kcal/mol/Å^2 each run, while holding the SWNT fixed, `equil_min2a.in`

```
equil step 2
 &cntrl

  ntx    = 1,       irest  = 0,       ntrx   = 1,      ntxo   = 1,
  ntpr   = 500,     ntwx   = 0,       ntwv   = 0,      ntwe   = 0,

  ntf    = 1,       ntb    = 1,
  cut    = 9.0,     nsnb   = 10,

  ibelly = 0,       ntr    = 1,

  imin   = 1,
  maxcyc = 600,
  ncyc   = 5000,
  ntmin  = 1,       dx0    = 0.1,     dxm    = 0.5,     drms   = 0.0001,

  ntc    = 1,       tol    = 0.0005,

 &end
Constraints
20.0
RES 1  24
END
Constraints
500.0
```

```
RES 25
END
END
```

Note: The restraints on DNA is relaxed by 5.0 kcal/mol/Å^2. The input files for other four rounds of step minimization are similar to this one, except the restraints are reduced to 15, 10, 5, 0, respectively.

The command is

```
%sander -O -i equil_min2a.in
           -o equil_min2a.out
           -c DNA_SWNT_equil_md1.restart
           -p DNA_SWNT_fixit.prmtop
           -r DNA_SWNT_equil_min2a.restart
           -ref DNA_SWNT_equil_md1.restart
```

A.9 FINAL EQUILIBRATION

Input file for `sander` final equilibration MD, no restraint on DNA, while holding SWNT fixed, `equil_md.in`

```
final equilibration, warm it up
 &cntrl

  nmropt = 1,
  ntx    = 1,       irest  = 0,       ntrx   = 1,      ntxo   = 1,
  ntpr   = 100,     ntwx   = 500,     ntwv   = 0,      ntwe   = 0,

  ntf    = 2,       ntb    = 2,
  cut    = 9.0,     nsnb   = 10,

  ibelly = 0,       ntr    = 1,

  imin   = 0,
  nstlim = 10000,
  t      = 0.0,     dt     = 0.002,

  temp0  = 300.0,   tempi  = 100.0,
  ig     = 71277,   heat   = 0.0,
  ntt    = 1,
  tautp  = 0.2,
  vlimit = 20.0,

  ntp    = 1,       pres0  = 1.0,     comp   = 44.6,
  ntc    = 2,       tol    = 0.00005,

 &end
```

```
 &wt
   type='TEMP0', istep1=0,     istep2=1000,
                 value1=100.0, value2=300.0,
 &end
 &wt
   type='TEMP0', istep1=1000,   istep2=10000,
                 value1=300.0, value2=300.0,
 &end
 &wt
   type='END',
 &end
 &rst
   iat=0,
 &end
Constraints
500.0
RES 25
END
END
```

Note: The starting temperature is 100 K. It is ramped to 300 K in the first 1000 steps. The command is

```
%sander -O -i equil_md.in
           -o equil_md.out
           -c DNA_SWNT_equil_min2e.restart
           -p DNA_SWNT_fixit.prmtop
           -r DNA_SWNT_equil_min2e.restart
           -ref DNA_SWNT_equil_md.restart
```

A.10 PRODUCTION RUN

Input file for `sander` production run, `md.in`

```
Production run, 50000 steps, that is 0.1 nanosecond
 &cntrl

  ntx    = 7,       irest  = 1,       ntrx   = 1,      ntxo   = 1,
  ntpr   = 100,     ntwx   = 500,     ntwv   = 0,      ntwe   = 0,

  ntf    = 2,       ntb    = 2,
  cut    = 9.0,     nsnb   = 10,

  ibelly = 0,       ntr    = 1,

  imin   = 0,
  nstlim = 50000,   nscm   = 0,
  t      = 0.0,     dt     = 0.002,

  temp0  = 300.0,   tempi  = 100.0,
  ig     = 71277,   heat   = 0.0,
  ntt    = 1,
  tautp  = 0.2,
  vlimit = 20.0,

  ntp    = 1,       pres0  = 1.0,     comp   = 44.6,
  taup   = 0.2,     npscal = 1,

  ntc    = 2,       tol    = 0.00005,

 &end
```

```
Constraints
500.0
RES 25
END
END
```

The command is

```
%sander -O -i md.in
           -o md.out
           -c DNA_SWNT_equil_md.restart
           -p DNA_SWNT_fixit.prmtop
           -r DNA_SWNT_equil_md.restart
           -ref DNA_SWNT_md.restart
           -x DNA_SWNT_md.traj
```

A.11 ANALYSIS-CARNAL INPUT FILE SAMPLE 1

Input file for `Carnal` analysis program, `carnal_dist.in`, used to calculate the distances between any two points in the simulation box, the angles between axis, atoms, or planes.

```
# FILES_IN lines designate the topology and trajectory files to be used
FILES_IN
# this is the topology file
  PARM p1 ntw.prmtop;
# this is the trajectory files, .gz files supported
  STREAM s1 ntw_1.traj ntw_2.traj ntw_3.traj ntw_4.traj ntw_5.traj;
# FILES_OUT set the printout files
FILES_OUT
# for scalar distance measurement, using regular table format
  TABLE tab1 tube_dist1.tab;
# DECLARE lines are actual command lines
DECLARE
# here I define atoms number 759 and 775 as a group
  GROUP gt1 (ATOM 759, 775);
# another group
  GROUP gt2 (ATOM 1318, 1334);
# define an axis between the center of mass of group gt1 and gt2 call it tube
  AXIS tube gt1%cmass gt2%cmass;
# define three other groups
  GROUP gc1 (ATOM 9,735);
  GROUP gc2 (ATOM 356,388);
  GROUP gc3 (ATOM 167,578,199,546);
# define another axis called dna between the geometry center of gc1 and gc2
  AXIS dna gc1%center gc2%center;
# measure the angle between the axes tube and dna just defined
  ANGLE ang1 tube, dna;
```

```
# measure the angle between the center of 3 groups of atoms defined
  ANGLE ang2 gc1%center gc3%center gc2%center;
# define the residue number 25 as another group, name it gwall
  GROUP gwall (RES 25);
# define residue 1 plus 24 as another group, name it g1
  GROUP g1 (RES 1, 24);
# measure the distance between center of mass of group g1 and the geometry
# center of group gwall, call it dist11_wall
  DIST dist11_wall g1%cmass gwall%center;
# OUTPUT line print out all the values measured to one big table, the name
# of the file for the table is what we set in FILES_OUT, the sequence of
# the measured data are printed one column by one column according to the
# order we DECLARE
OUTPUT
  TABLE tab1 MEAS;
END
```

The command is

```
%carnal -O < carnal_dist.in
```

A.12 ANALYSIS-CARNAL INPUT FILE SAMPLE 2

Input file for `Carnal` analysis program, `carnal_rms.in`, used to calculate the RMSD vs time.

```
FILES_IN
  PARM p1 ntw.prmtop;
  STREAM s1 ntw_1.traj ntw_2.traj ntw_3.traj ntw_4.traj ntw_5.traj;
# STATIC line set the reference coordinate file
  STATIC ref_set ntw.inpcrd;
FILES_OUT
  TABLE tab1 rms1;
DECLARE
  GROUP g1 (RES 1 - 24);
# calculate RMS values for group g1 compared to ref_set
  RMS fit1 FIT g1 s1 ref_set;
OUTPUT
  TABLE tab1 fit1;
END
```

A.13 ANALYSIS-CARNAL INPUT FILE SAMPLE 3

Input file for `Carnal` analysis program, `carnal_pdb.in`, used to extract PDB files from trajectory files.

```
FILES_IN
  PARM p1 ntw.prmtop;
# set three trajectory files to be used
  STREAM s1 ntw_1.traj;
  STREAM s3 ntw_3.traj;
  STREAM s5 ntw_5.traj;
FILES_OUT
# the PDB files extracted from each different trajectory file
# will be named differently, the PDB files extracted from s1
# will start with the name test1.pdb
  COORD c1 test1.pdb PDB;
  COORD c3 test3.pdb PDB;
  COORD c5 test5.pdb PDB;
DECLARE
# I want the PDB files only for residue 1 to 25
  GROUP g1 (RES 1 - 25);
OUTPUT
# from s1, I extract 2 PDB files, the first one is replica
# number 40, the second is the replica number 90, they will
# be named as test1.pdb.40 and test1.pdb.90
# from s2 and s3, I only extract 1 PDB file from each
  COORD c1 s1 SELECT(40 90) GROUP g1;
  COORD c3 s3 SELECT(90) GROUP g1;
  COORD c5 s5 SELECT(90) GROUP g1;
END
```

A.14 ANALYSIS-CARNAL INPUT FILE SAMPLE 4

Input file for `Carnal` analysis program, `carnal_strip.in`, used to strip the water and ion coordinates from trajectory files. The stripping process can be applied before producing MD movies.

```
FILES_IN
  PARM p1 ntw.prmtop;
  STREAM s1 ntw_0.traj ntw_1.traj ntw_2.traj ntw_3.traj ntw_4.traj ntw_5.traj
            ntw_6.traj ntw_7.traj ntw_8.traj ntw_9.traj;
FILES_OUT
# The default format for COORD file is trajectory format
  COORD c1 ntw_strip.traj;
DECLARE
# I want the trajectory for DNA and SWNT only
  GROUP g1 (RES 1 - 25);
OUTPUT
# I need all the replica, starting from No. 1
  COORD c1 s1 SELECT(1-) GROUP g1;
END
```

BIBLIOGRAPHY

[1] D. P. Valenzuela and A. L. Myers. *Adsorption Equilibrium Data Handbook*. Prentice Hall, New Jersey, 1989.

[2] D. M. Ruthven. *Principles of Adsorption and Adsorption Processes*. John Wiley & Sons, New York, 1984.

[3] J. M. Prausnitz, R. N. Lichtenthaler, and E. G. de Azevedo. *Molecular Thermodynamics of Fluid Phase Equilibria*. Prentice-Hall, New York, 3 edition, 1999.

[4] A. R. Leach. *Molecular Modeling: Principles and Applications*. Prentice Hall, 2001.

[5] S. Y. Jiang, K. E. Gubbins, and J. A. Zollweg. *Mol. Phys.*, 83:103, 1993.

[6] A. V. Klochko, E. N. Brodskaya, and E. M. Piotrovskaya. *Langmuir*, 15:545, 1999.

[7] R. F. Cracknell and D. Nicholson. *Mol. Phys.*, 80:885, 1993.

[8] R. F. Cracknell and D. Nicholson. *Mol. Sim.*, 13:161, 1994.

[9] R. F. Cracknell and D. Nicholson. *J. Chem. Soc., Faraday Trans.*, 90:1487, 1994.

[10] R. F. Cracknell and D. Nicholson. *Adsorption*, 1:7, 1995.

[11] L. D. Gelb and K. E. Gubbins. *Stud. Surf. Sci. Catal.*, 128:61, 2000.

[12] M. Sliwinska-Bartkowiak, J. Gras, R. Sikorski, G. Dudziak, R. Radhakrishnan, and K. E. Gubbins. *Stud. Surf. Sci. Catal.*, 128:141, 2000.

[13] K. T. Thomson and K. E. Gubbins. *Langmuir*, 16:5761, 2000.

[14] M. J. Bojan and R. van Sloonten. *Sep. Sci. Tech.*, 27:1837, 1992.

[15] J. L. Soto and A. L. Myers. *Mol. Phys.*, 42:971, 1981.

[16] G. B. Woods, A. Z. Panagiotopoulos, and J. S. Rowlinson. *Mol. Phys.*, 63:49, 1988.

[17] S. Yashonath, J. M. Thomas, A. K. Nowak, and A. K. Cheetham. *Nature*, 331:601, 1988.

[18] S. Yashonath, P. Demontis, and M. L. Klein. *Chem. Phys. Letters*, 153:551, 1988.

[19] G. B. Woods and J. S. Rowlinson. *J. Chem. Soc., Faraday Trans. 2*, 85:765, 1989.

[20] R. L. June, A. T. Bell, and D. N. Theodorou. *J. Phys. Chem.*, 94:1508, 1990.

[21] F. Karavias and A. L. Myers. *Mol. Sim.*, 8:23, 1991.

[22] F. Karavias and A. L. Myers. *Mol. Sim.*, 8:51, 1991.

[23] R. Q. Snurr, A. T. Bell, and D. N. Theororou. *J. Phys. Chem.*, 97:13742, 1993.

[24] M. D. LeVan, editor. *Fundamentals of Adsorption: Proceedings of the Fifth International Conference on Fundamentals of Adsorption*, Boston, 1996. Kluwer Academic Publishers.

[25] R. J. M. Pellenq, B. Tavitian, D. Espinat, and A. H. Fuchs. *Langmuir*, 12:4768, 1996.

[26] M. Heuchel, R. Q. Snurr, and E. Buss. *Langmuir*, 13:6795, 1997.

[27] L. F. Gladden, M. Hargreaves, and P. Alexander. *Chem. Eng. J.*, 74:57, 1999.

[28] M. D. Macedonia and E. J. Maginn. *Fluid Phase Equilibria*, 160:19, 1999.

[29] F. Marinelli, Y. Grillet, and R. J. M. Pellenq. *Mol. Phys.*, 97:1207, 1999.

[30] T. J. Hou, L. L. Zhu, and X. J. Xu. *J. Phys. Chem. B*, 104:9356, 2000.

[31] R. J. M. Pellenq, S. Rodts, V. Pasquier, A. Delville, and P. Levitz. *Adsorption*, 6:241, 2000.

[32] W. A. Steele. *Chem. Rev*, 93:2355, 1993.

[33] E. M. Aydt and R. Hentschke. *Ber. Bunsen. Phys. Chem.*, 101:79, 1997.

[34] G. W. Wu and K. Y. Chan. *Fluid Phase Equilibria*, 132:21, 1997.

[35] M. Pierce and E. Manousakis. *Phys. Rev. B*, 63:144524, 2001.

[36] M. Pierce and E. Manousakis. *Phys. Rev. B*, 59:3802, 1999.

[37] M. Pierce and E. Manousakis. *Phys. Rev. Lett*, 81:156, 1998.

[38] Q. Y. Wang and J. K. Johnson. *Mol. Phys*, 95:299, 1998.

[39] Q. Y. Wang and J. K. Johnson. *Int. J. Thermophys*, 19:835, 1998.

[40] J. J. Potoff and J. I. Siepmann. *Phys. Rev. Lett*, 85:3460, 2000.

[41] F. Y. Hansen and H. Taub. *Inorg. Mater*, 35:586, 1999.

[42] S. Balasubramanian, M. L. Klein, and J. I. Siepmann. *J. Chem. Phys*, 103:3184, 1995.

[43] R. Hentschke and R. G. Winkler. *J. Chem. Phys*, 99:5528, 1993.

[44] R. Hentschke, B. L. Schurmann, and J. P. Rabe. *J. Chem. Phys*, 96:6213, 1992.

[45] R. Loring and G. H. Findenegg. *J. Coll. Inter. Sci.*, 84:355, 1981.

[46] G. H. Findenegg and R. Loring. *J. Chem. Phys.*, 81:3270, 1984.

[47] P. Glanz, B. Korne, and G. H. Findenegg. *Adsorp. Sci. Tech.*, 1:183, 1984.

[48] A. L. Myers and J. M. Prausnitz. *AIChE J.*, 11:121, 1965.

[49] B. A. Younglove and J. F. Ely. *J. Phys. Chem. Ref. Data*, 16:577, 1987.

[50] R. Lustig and W. A. Steele. *Mol. Phys.*, 65:475, 1988.

[51] W. L. Jorgensen, J. D. Madura, and C. J. Swenson. *J. Am. Chem. Soc.*, 106:813, 1984.

[52] M. G. Martin and J. I. Siepmann. *J. Phys. Chem. B*, 102:2569, 1998.

[53] S. K. Nath, F. A. Escobedo, and J. J. de Pablo. *J. Chem. Phys.*, 108:9905, 1998.

[54] J. I. Siepmann, S. Karaborni, and B. Smit. *Nature*, 365:330, 1993.

[55] M. P. Allen and D. J. Tildesley. *Computer Simulation of Liquids*. Clarendon, Oxford, 1987.

[56] N. B. Vargaftik et al. *Handbook of Physical Properties of Liquids and Gases: Pure Substances and Mixtures*. Begell House, New York, 1996.

[57] W. A. Steele. *Surf. Sci.*, 36:317, 1973.

[58] D. Nicholson and N. G. Parsonage. *Computer Simulation and the Statistical Mechanics of Adsorption*. Academic Press, London, 1982.

[59] D. M. Shen, F. Siperstein M. Bülow, M. Engelhard, and A. L. Myers. *Adsorption*, 6:275, 2000.

[60] M. Lal and D. Spencer. *J. Chem. Soc., Faraday Trans. 2*, 70:910, 1973.

[61] J. G. Daunt, S. G. Hedge, S. P. Tsui, and E. Lerner. *J. Low Temp. Phys.*, 44:207, 1981.

[62] E. L. Pace and A. R. Siebert. *J. Phys. Chem.*, 63:1398, 1959.

[63] E. J. Bottani and V. A. Bakaev. *Langmuir*, 10:1550, 1994.

[64] V. Bakaev E. J. Bottani and W. Steele. *Chem. Eng. Sci*, 49:2931, 1994.

[65] J. S. Raut, D. S. Sholl, and K. A. Fichthorn. *Surf. Sci.*, 389:88, 1997.

[66] N. N. Avgul and A. V. Kiselev. Physical adsorption of gases and vapors of graphitized carbon blacks. In P. L. Walker, Jr, editor, *Chemistry and Physics of Carbon*, volume 6, page 1. Marcer Dekker, Inc., New York, 1970.

[67] L. W. Bruch. *Surf. Sci.*, 195:194, 1983.

[68] F. Y. Hansen, L. W. Bruch, and S. E. Roosevelt. *Phys. Rev. B*, 45:11238, 1992.

[69] A. Vernov and W. A. Steele. *Langmuir*, 8:155, 1992.

[70] D. B. Whitehouse and A. D. Buckingham. *J. Chem. Soc. and Faraday Trans.*, 89:1909, 1993.

[71] W. A. Steele. *The Interaction of Gases with Solid Surfaces*. Pergamon, Oxford, 1974.

[72] D. Nicholson and K. E. Gubbins. *J. Chem. Phys.*, 104:8126, 1996.

[73] J. L. Hirschfelder, C. F. Curtiss, and R. B. Bird. *Molecular Theory of Gases and Liquids*. John Wiley & Sons, Inc., New York, 1954.

[74] L. W. Bruch, M. W. Cole, and E. Zaremba. *Physical Adsorption: Forces and Phenomena*. Clarendon Press, Oxford, 1997.

[75] P. Jedlovszky and G. Pálinkás. *Mol. Phys.*, 84:217, 1995.

[76] D. Möller and J. Fischer. *Fluid Phase Equilibria*, 100:35, 1994.

[77] *CRC Handbook of Chemistry and Physics*. Boca Raton : CRC Press, 80 edition, 1999.

[78] M. Ferrario, M. Haughney, I. R. McDonald, and M. L. Klein. *J. Chem. Phys.*, 93:5156, 1990.

[79] R. L. Rowley. *Statistical Mechanics for Thermophysical Property Calculations*. Prentice Hall, Englewood Cliffs, NJ, 1994.

[80] A. D. Buckingham, R. L. Disch, and D. A. Dunmur. *J. Am. Chem. Soc.*, 90:3104, 1968.

[81] A. D. Buckingham, C. Gramham, and J. H. Williams. *Mol. Phys.*, 49:703, 1983.

[82] T. Kristof and J. Liszi. *J. Phys. Chem. B*, 101:5480, 1997.

[83] M. R. Battaglia, A. D. Buckingham, D. Neumark, R. K. Pierens, and J. H. Williams. *Mol. Phys.*, 43:1015, 1981.

[84] R. L. Gale and R. A. Beebe. *J. Phys. Chem.*, 68:555, 1964.

[85] D. Feller and K. D. Jordan. *J. Phys. Chem. A*, 104:9971, 2000.

[86] M. W. Cole, J. K. Johnson, A. Other, B. Other, C. Other, and D. Other. to be published.

[87] Z. M. Wang and K. Kaneko. *J. Phys. Chem.*, 99:16714, 1995.

[88] A. D. Crowell. *J. Chem. Phys.*, 49:892, 1968.

[89] X. C. Zhao, S. J. Kwon, R. Vidic, E. Borguet, and J. K. Johnson. *J. Chem. Phys.*, 117:7719, 2002.

[90] M. P. Allen and D. J. Tildesley. *Computer Simulation of Liquids*. Clarendon Press: Oxford, 1987.

[91] B. Smit. *Mole. Phys.*, 85:153–172, 1995.

[92] S. J. Kwon, J. Russell, X. C. Zhao, R. D. Vidic, J. K. Johnson, and E. Borguet. *Langmuir*, 18:2595, 2002.

[93] A. Zangwill. *Physics at Surfaces*. New York: Cambridge University Press, 1988.

[94] M. A. Van Hove, W. H. Weinberg, and C. M. Chan. *Low Energy Electron Diffraction and Structural Determination*, volume 6 of *Springer Series in Surface Sciences*. Berlin:Springer-Verlag, 1986.

[95] R. D. Ramsier and J. T. Yates Jr. *Surface. Sci. Rep.*, 12:243, 1991.

[96] J. G. Lee, S. H. Hong, J. Ahner, X. C. Zhao, J. K. Johnson, and J. T. Yates, Jr. submitted.

[97] J. Mocuta D. Ahner and J. T. Yates Jr. *Vac. Sci. Tech. A*, 17:2333–2338, 1999.

[98] J. Piper, J. A. Morrison, and C. Peters. *Mole. Phys.*, 53:1463–1480, 1984.

[99] W. B. J. M. Jassen, J. Michiels, and A. van der Avoird. *J. Chem. Phys.*, 94:8402–8407, 1991.

[100] C. Ramseyer, C. Girardet, F. Bartolucci, G. Schmitz, R. Franchy, D. Teillet-Billy, and J. P. Gauyacq. *Phys. Rev. B*, 58:4111–4119, 1998.

[101] R. Smoluchowski. *Phys. Rev.*, 60:661, 1941.

[102] C. Herring and M. H. Nichols. *Rev. Modern Phys.*, 21:185, 1949.

[103] R. Gomer. *Field Emission and Field Ionization*. America Vacuum Society Classic, AIP NewYork, 1993.

[104] D. B. Macleod. *Trans. Faraday Soc.*, 19:38, 1923.

[105] E. A. Guggenheim. *J. Chem. Phys.*, 13:253, 1945.

[106] O. R. Quayle. *Chem. Rev.*, 53:439, 1953.

[107] J. S. Rowlinson and B. Widom. *Molecular Theory of Capillarity*. Clarendon Press, Oxford, UK, 1989.

[108] J. Escobedo and G. A. Mansoori. *AIChE J.*, 42:1425, 1996.

[109] Z. B. Li and C. Y. Lu. *Can. J. Chem. Eng.*, 79:402, 2001.

[110] J. F. Lu, D. Fu, J. C. Liu, and Y. G. Li. *Fluid Phase Equilibria*, 194-197:755, 2002.

[111] D. D. Do, E. Ustinov, and H. D. Do. *Fluid Phase Equilibria*, 204:309, 2003.

[112] M. Z. Faizullin. *Fluid Phase Equilibria*, 211:75–83, 2003.

[113] M. A. Hooper and S. Nordholm. *Mol. Phys.*, 47:329, 1982.

[114] D. N. Sinha, J. S. Semura, and L. C. Brodie. *J. Chem. Phys.*, 76:2028, 1982.

[115] H. L. Frisch and P. Nielaba. *J. Chem. Phys.*, 105(16):7238, 1996.

[116] K. S. Liu. *J. Chem. Phys.*, 60:4226, 1974.

[117] J. K. Lee, J. A. Baker, and G. M. Pound. *J. Chem. Phys.*, 64:1976, 1974.

[118] G. A. Chapela, G. Saville, and J. S. Rowlinson. *Faraday Discuss. Chem. Soc.*, 59:22, 1975.

[119] J. Miyazaki, J. A. Barker, and G. M. Pound. *J. Chem. Phys.*, 64:3364, 1976.

[120] M. Rao and D. Levesque. *J. Chem. Phys.*, 73:455, 1979.

[121] G. A. Chapela, G. Saville, S. M. Thompson, and J. S. Rowlinson. *J. Chem. Soc. Faraday Trans.*, 73:1133, 1977.

[122] M. Rao and B. J. Berne. *Mol. Phys.*, 37:455, 1979.

[123] J. P. R. B. Walton, D. J. Tildesley, and J. S. Rowlinson. *Mol. Phys.*, 48:1357, 1983.

[124] M. Matsumoto and Y. Kataoka. *J. Chem. Phys.*, 88:3233, 1988.

[125] M. J. P. Nijmeijer, A. F. Baker, and C. Bruin. *J. Chem. Phys.*, 89:3789, 1988.

[126] J. Alejandre, D. J. Tildesley, and G. A. Chapela. *Mol. Phys.*, 85(3):651, 1995.

[127] E. Salomons and M. Mareschal. *J. Phys.: Condens. Matter*, 3:3645, 1991.

[128] C. D. Holcomb, P. Clancy, S. M. Thompson, and J. A. Zollweg. *Fluid Phase Equilibria*, 75:185–196, 1992.

[129] C. D. Holcomb, P. Clancy, S. M. Thompson, and J. A. Zollweg. *Fluid Phase Equilibria*, 88:303, 1993.

[130] C. D. Holcomb, P. Clancy, and J. A. Zollweg. *Mol. Phys.*, 78:437–459, 1993.

[131] M. Mecke, J. Winkelmann, and J. Fischer. *J. Chem. Phys.*, 107:9264, 1997.

[132] M. Mecke, J. Winkelman, and J. Fischer. *J. Chem. Phys.*, 110:1188, 1999.

[133] V. G. Baidakov, G. G. Chernykh, and S. P. Protsenko. *Chem. Phys. Lett.*, 321:315, 2000.

[134] J. J. Potoff and A. Z. Panagiotopoulos. *J. Chem. Phys.*, 112(14):6411, 2000.

[135] R. P. Feynman and A. R. Hibbs. *Quantum Mechanics and Path Integrals*. New York: McGraw-Hill, 1965.

[136] M. E. Tuckerman, B. J. Berne, G. J. Martyna, and M. L. Klein. *J. Chem. Phys.*, 99:2796, 1993.

[137] Q. Y. Wang, J. K. Johnson, and J. Q. Broughton. *Mol. Phys.*, 69:1105, 1996.

[138] Q. Y. Wang and J. K. Johnson. *Fluid Phase Equilibrium*, 132:93–116, 1997.

[139] R. H. Fowler. *Proc. R. Soc. London, Ser. A*, 159:229, 1937.

[140] E. M. Blokhuis, D. Bedeaux, C. D. Holcomb, and J. A. Zollweg. *Mol. Phys.*, 85:665, 1995.

[141] S. Plimpton. *J. Comp. Phys.*, 117:1, 1995.

[142] S. Plimpton and B. Hendrickson. Parallel molecular dynamics algorithms for simulation of molecular systems. In T. G. Mattson, editor, *Parallel Computing in Computational Chemistry*, ACS Symoposium Series, page 114, Washington, DC, 1995. Ameican Chemical Society.

[143] I.F. Silvera, , and V. V. Goldman. *J. Chem. Phys.*, 69:4209, 1978.

[144] V. Buch. *J. Chem. Phys.*, 100:7610, 1994.

[145] U. Buck, F. Huisken, A. Kohlhase, and D. Ottten. *J. Chem. Phys.*, 78:4439, 1983.

[146] M. G. Dondi and U. Valbusa. *Chem. Phys.*, 17:137, 1972.

[147] P. Diep and J. K. Johnson. *J. Chem. Phys.*, 113:3480–3481, 2000.

[148] P. Diep and J. K. Johnson. *J. Chem. Phys.*, 112:4465–4473, 2000.

[149] P. Wind and I. Røeggen. *Chem. Phys.*, 174:345–350, 1993.

[150] M. E. Tuckerman, B. J. Berne, and G. J. Martyna. *J. Chem. Phys.*, 97:1990, 1992.

[151] R. D. McCarty, J. Hord, and H. M. Roder. Selected properties of hydrogen. Monograph 168, National Bureau of Standards, Washington D. C., 1981.

[152] H. M. Roder, G. E. Childs, R. D. McCarty, and P. E. Angerhofer. Survey of properties of the hydrogen isotopes below their critical temperatures. Technical Note 641, Natinal Bureau of Standards, Washington D. C., 1973.

[153] P. C. Souers. *Hydrogen Properties for Fusion Energy*. Berkeley: University of California Press, 1986.

[154] R. B. Newman and L. C. Jackson. *Trans. Faraday Soc.*, 54:1481, 1958.

[155] V. N. Grigoriev and N. S. Rudenko. *Zhurnal Eksperimental'noi i Teoreticheskoi Fiziki*, 47:92–96, 1964.

[156] I. Prigogine. *Molecular Theory of Solution*. North-Holland Pub. Co., Amsterdam, 1957.

[157] A. Englert-Chwoles and I. Prigogine. *Nuovo Cimento*, Suppl. 9:347, 1958.

[158] S. R. Challa and J. K. Johnson. *J. Chem. Phys.*, 111:724–729, 1999.

[159] M. M. Telo da Gama and R. Evans. *Mol. Phys.*, 48:229, 1983.

[160] M. S. Pettersen and W. F. Saam. *J. Low Temp. Phys.*, 90:159–165, 1993.

[161] W. F. Saam and M. S. Pettersen. *J. Low Temp. Phys.*, 101:355–360, 1995.

[162] M. S. Pettersen. *J. Low Temp. Phys.*, 117:67–79, 1999.

[163] N. Metropolis, A. W. Rosebluth, M. N. Rosebluth, A. N. Teller, and E. Teller. *J. Chem. Phys.*, 21:1087, 1953.

[164] D. L. Beveridge and G. Ravishanker. *Curr. Opin. Struct. Biol.*, 4:246–255, 1994.

[165] P. Ewald. *Ann. Phys. Leipzig*, 64:253–264, 1921.

[166] D. D. J. MacKerell and N. Banavali. *J. Comput. Chem.*, 21:105–120, 2000.

[167] W. D. Cornell, P. Cieplak, C. I. Bayly, I. R. Gould, and K. M. Merz. *J. Am. Chem. Soc.*, 117:5170–5197, 1995.

[168] T. A. Darden, D. M. York, and L. G. Pedersen. *J. Chem. Phys.*, 98:10089–10092, 1993.

[169] T. E. Cheatham, III and P. A. Kollman. *Annu. Rev. Phys. Chem.*, 51:435–471, 2000.

[170] T. E. Cheatham, III and M. A. Young. *Biopolymer*, 56:232–256, 2001.

[171] R. H. Baughman, A. A. Zakhidov, and W. A. de Heer. *Science*, 297:787, 2002.

[172] M. S. Dresselhaus and P. C. Eklund. *Advances in Physics*, 49:705–814, 2000.

[173] Q. Y. Wang and J. K. Johnson. *J. Phys. Chem. B*, 103:4809–4813, 1999.

[174] F. L. Darkrim, P. Malbrunot, and G. P. Tartaglia. *Int. J. Hydrogen Energ.*, 27:193, 2002.

[175] W. A. de Heer, A. Chatelain, and D. Ugarte. *Science*, 270:1179, 1995.

[176] S. Tans. *Nature*, 393:49, 1998.

[177] A. Thess. *Science*, 273:483, 1996.

[178] G. H. Gao, T. Çagĭn, and W. A Goddard, III. *Nanotechnology*, 9:184, 1998.

[179] S. S. Wong, A. T. Woolley, T. W. Odom, P. Huang, J. L.and Kim, D. V. Vezenov, and C. M. Lieber. *Appl. Phys. Lett.*, 73:299, 1998.

[180] A. T. Woolley, C. Guillemette, C. L. Cheung, D. E. Housmani, and C. M. Lieber. *Nature Biotechnology*, 18:760–763, 2000.

[181] J. Michalowski, D. Kerrigan, and J. Kelly. Understanding nanodevices. Published online. National Cancer Institute.

[182] M. Zheng, A. Jagota, E. D. Semke, B. A. Diner, R. S. McLean, S. R. Lustig, R. E. Richardson, and N. G. Tassi. *Nature Materials*, 2:338, 2003.

[183] S. Q. Wang, E. S. Humphreys, S. Y. Chung, D. F. Delduco, S. R. Lustig, H. Wang, K. N. Parker, N. W. Rizzo, S. Subramoney, Y. M. Chiang, and A. Jagota. *Nature Materials*, 2:196, 2003.

[184] Report. Carbon nanotubes and nanofibers:the self-assembly challenge. ORNL Review online, Vol. 34, No. 2.

[185] G. Hummer, J. C. Rasaiah, and J. P. Noworyta. *Nature*, 414:188, 2001.

[186] A. Kalra, S. Garde, and G. Hummer. *Proc. Natl Acad. Sci. USA*, 100:10175, 2003.

[187] W. L. Jorgensen, D. S. Maxwell, and J. Tirado-Rives. *J. Am. Chem. Soc.*, 118:11225, 1996.

[188] W. F. van Gunsteren and H. J. C. Berendsen. *GROMOS 87 Manual*. The Netherlands, 1987.

[189] V. V. Simonyan, P. Diep, and J. K. Johnson. *J. Chem. Phys.*, 111:9778–9783, 1999.

[190] H. J. C. Berendsen, J. P. M. Postma, W. F. von Gunsteren, and J. Hermans. *Intermolecular Forces*. Reidel, Dordrecht, Holland, 1981.

[191] H. J. C. Berendsen, J. R. Griega, and T. P. Straatsma. *J. Phys. Chem.*, 91:6269, 1987.

[192] W. L. Jorgensen. *J. Am. Chem. Soc.*, 103:335, 1981.

[193] J. Brodholt, M. Sampoli, and R. Vallauri. *Mole. Phys.*, 86:149, 1995.

[194] A. A. Chialvo and P. T. Cummings. *J. Chem. Phys.*, 105:8274, 1996.

[195] L. X. Dang and T. M. Chang. *J. Chem. Phys.*, 106:8149, 1997.

[196] W. L. Jorgensen, J. Chandrasekhar, and J. Madura. *J. Chem. Phys.*, 79:926, 1983.

[197] P. Jedlovszky and J. Richardi. *J. Chem. Phys.*, 110:8019, 1999.

[198] H. J. C. Berendsen, J. P. M. Postma, W. F. van Gunsteren, A. D. Nola, and J. R. Haak. *J. Chem. Phys.*, 81:3684–3690, 1984.

[199] M. A. Young, B. Jayaram, and D. L. Beveridge. *J. Am. Chem. Soc.*, 119:59–69, 1997.

[200] K. Miaskiewicz, R. Osman, and H. Weinstein. *J. Am. Chem. Soc.*, 115:1526–1537, 1993.

[201] S. J. Tans, M. H. Devoret, H. J. Dai, A. Thess, R. E. Smalley, L. J. Geerligs, and C. Dekker. *Nature*, 386:474, 1997.

[202] L. Grigoryan, G. I. Sumanasekera, A. L. Loper, S. Fang, J. L. Allen, and P. C. Eklund. *Phys. Rev. B*, 58:4195, 1998.

[203] M. Zheng, A. Jagota, M. S. Strano, A. P. Santos, P. Barone, S. G. Chou, B. A. Diner, M. S. Dresselhaus, R. S. Mclean, G. Bibiana, G. G. Samsonidze, E. D. Semke, M. Usrey, and D. J. Walls. *Science*, 302:1545, 2003.